High Resolution Studies of Deep Earth Structure

Thesis by

Xiaoming Ding

In Partial Fulfillment of the Requirements

for the Degree of

Doctor of Philosophy

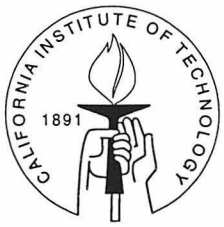

California Institute of Technology

Pasadena, California

1998

(Submitted June 24, 1997)

Acknowledgements

Thanks to the Seismological Laboratory, Caltech for giving me the privilege to work here. One of the best experiences I had during my 5 years stay here is that I actually experienced a big earthquake (Northridge earthquake) and survived it. I suppose that is necessary for people to become a seismologist.

My advisor, mentor, Prof. Don V. Helmberger is the most wonderful person I have ever met in my life. Not only did he show me the interesting things about seismology (e.g., a small wiggle in some seismograms is an important phase), he also showed his encouragement, extreme patience and understanding of me as a poor, hard-working, no-life Caltech graduate student.

The CSEDI group meeting is a great place to get inspirations. It includes three professors, Don Anderson, Mike Gurnis, and Don Helmberger and three students Igor Sidorin, Lianxing Wen and me. Thanks to them for helping me to view my study from another fundamental aspect — Earth mantle convection. Thanks to Steve Grand for introducing me into the field and allowing me slicing through his 3D tomographic model.

I also thank my former office-mate Emily Brodsky for interesting discussions we had and helping to proof-read my thesis. Thanks to Xi Song and Weishi Huang for picking me up at the airport and oriented me into Caltech campus. Ed Garnero, Xiaodong Song have been a great help in my study all the time. Craig Scrivner taught me all kinds of Perl tricks. Thanks to George Chen, Kathleen Holland and Wenbo Yang for explaining their high pressure and high temperature shock wave experiment to me and expanding my understanding of deep mantle minerology. Thanks to Timothy Melbourne for reviewing my paper.

Thanks to Jinbo Chen's family and Yi-chun Wang's family for being such good friends of my family, we have had a lot of wonderful time together. Last but not least, thanks to my wife for being a constant support. Her understanding, considerate and

hard-work at home made this thesis possible.

Abstract

Recent advances in seismic tomography has imaged major deep structure in the lower mantle. The ring of fast velocities originally derived from global long-period inversions has been resolved into interspersed sheet-like structure which appears to be old slabs. Beneath some of the structure, there are high velocity zones (HVZ) with variable thickness approaching the core mantle boundary (CMB). Detailed broadband modeling of waveforms produced by seismic paths sampling one of these zones yields a picture of D″ zone, with one thermal negative above the layer and one positive approaching the CMB, which would seem to be quite compatible with pancaked slab debris. In contrast, modeling waveforms produced by sampling the slowest velocity regions along the CMB reveals a thin ultra low velocity zone (ULVZ). The dimensions of these zones range from a few hundred km beneath Iceland to a few thousand km beneath Africa.

Seismic data recorded on TERRAscope and Berkeley Digital Seismic Network are used to study the HVZ beneath Central America. Modeling these waveforms (P, SV and SH) constitutes a major portion of this thesis. Two modeling strategies were employed in the thesis: (1) Assume a "Lay type" D″ with a sharp velocity discontinuity; (2) Assume an upper transition zone approaching D″, and a lower transition zone approaching the CMB (old slabs). Our preferred model following strategy (1) (Chapter 2) has an S discontinuity 200 km above the CMB with 3% jump and a negative gradient in the D″ layer. It fits S, SKS, Scd on radial component and S and Scd phase on tangential component in the distance range of 78° to 92°. A 2D model with decreasing thickness of D″ layer toward North is also investigated. It fits the data better at the distances beyond 90° and produces reasonable good fit of the S and Scd phases. This suggests that the typical negative gradient in the "Lay type" D″ may not be necessary as in SDH. P waveform modeling, on the other hand, shows no indication of a corresponding Pcd phase. The PREM model fits the P travel time

and waveform well. Our preferred model following strategy (2) (Chapter 3) has a positive gradient initiated 350 km above the CMB with a sharper increase near 200 km and a strong negative gradient begins at about 100 km. This model can explain both P and S waveforms.

In Chapter 4 the ULVZ beneath Iceland and Africa are addressed. The major phases used to study the ULVZ are SKS and $S_{P_{diff}}KS$ which travels along the CMB as P at both the core entry ($S_{P_{diff}}KS$) and exit ($SK_{P_{diff}}S$) locations. A major structure beneath Iceland ($SK_{P_{diff}}S$) as identified from data recorded on stations in Northern Europe appears to be shaped like a dome, 80 km high, 200 km wide with a 10% drop in P and S velocities. The data for Africa is less complete but highly anomalous. Shear wave record sections across Africa and Europe containing the cross-over from S to SKS and extended core-phases (75° to 120°) are presented from deep South American events. These are compared against corresponding synthetics for various tomography models computed with a new 2D synthesizing technique (Appendix A). Some of the most recent models, *Grand* [1994], explain the observation for African data better than 1D models. However, considerable fine tuning is required in D″ to explain abrupt changes in S and ScS waveforms and the extreme cases in SKS-S travel times. Essentially, Grand's anomaly needs to be increased to -4% with evidence for a strong plume (1500 km of vertical structure with -4% velocity drop) to explain the SKS travel times and waveform data. The plume is located along the eastern edges of the basal low velocity region.

By studying the various branches of the core phases PKP, it has become quite clear that North-South paths in the inner-core appear faster than East-West paths. Moreover, the broadband seismograms associated with these paths are distinct. The reason for this difference is not known but suggests a lower (anisotropic) inner-core with an upper (isotropic) inner-core which may have variable thickness. Modeling of long period and broadband data for such structures is, also, addressed in Chapter 5 of this thesis.

Contents

List of Figures

List of Tables

Chapter 1 General Introduction

1.1 D″ region

The lower-most 200 km of the mantle, region D″, is known to be a region of generally low seismic gradient [*Dziewonski and Anderson*, 1981] and increased scatter in travel times and amplitudes. It is now recognized that this region is highly heterogeneous in material properties on large and small scales, presumably due to thermal and chemical variations.

The large scale tomographic models [e.g., *Masters et al.*, 1996; *Su et al.*, 1994; *Li and Romanowicz*, 1996] have discovered the faster than average structure at the base of the mantle associated with the circum-Pacific ring. *Richards and Engebretson* [1992] found that the faster than average seismic velocities in the lower mantle occur in regions with long subduction history, therefore, concluded that most slabs penetrate down to the core mantle boundary (CMB). In contrast, *Wen and Anderson* [1995] concluded that slabs generally remain in the upper mantle based on the high degree correlation between seismic structure at the top of the lower mantle and the subduction history. The fact that different conclusions have been reached based on similar long wavelength images suggests higher resolution image are necessary in order to understand the process. Recently, *Grand* [1994] and *van der Hilst et al.* [1997] obtain S and P tomographic models independently using different seismic data sets and different inversion techniques. These two models are compatible even at small scales down to 500km. They confirm the fast structure of circum-Pacific rings and show that these structures are linearized, and well correlated with the subduction history. Beneath Central America is one such fast anomaly. In recognition of the high heterogeneity of the D″ structure, we utilize the newly developed TERRAscope (Caltech) and Berkeley Digital Seismic Network (U. C. Berkeley) arrays to resolve both P and S structures at a constrained azimuth with all three components of broad-

band data in Chapter 2. We found an obvious discontinuity of S velocity but not in P. Furthermore, the anisotropy is constrained in the bottom of the D″.

We propose a different type of model from the typical "Lay type" discontinuity for the above region. We add two thermal boundarylayers on top and bottom of the D″ layer assuming the fast anomaly is caused by a subducted slab, as interpreted by *Grand* [1994] and *Grand et al.* [1997]. This type of model is compatible to the velocity model generated from geodynamic modeling.

The recent discovery of the ultra low velocity zone (ULVZ) by *Garnero and Helmberger* [1996] reveals another dramatic structure at the base of the mantle. This layer has a thickness of 10–50 km and is characterized by a 10% decrease of the P velocity as established with studies of SKS and the associated $S_{P_{diff}}KS$ and/or $SK_{P_{diff}}S$ phases. The original discovery was reported for beneath south Fiji, and it was soon found that this layer generally underlies larger scale slow anomalies in the lower mantle. ULVZs beneath two distinct regions are investigated in Chapter 4. One is very localized beneath Iceland as the S, SKS, SKKS differential travel times do not show any anomaly while $SK_{P_{diff}}S$ is very anomalous. The other is the most prominent slow anomalies in the world at the base of the mantle as shown by *Grand* [1994] — the African anomaly. The complexity of the upper mantle structure of the Africa anomaly impose some interesting observations on seismic records. For example, the Southern Africa is a shield which will speed up the S arrivals while central and northern Africa is a rift zone which will slow down the S arrivals. The large slow anomaly extends up to the depth of 1000 km and shows a plume like structure. We propose a 2D model that can explain the travel time and waveform data of S and SKS well. The model is obtained by enhance the slow anomalies beneath Africa in *Grand* [1994] to -4%.

1.2 Inner-core structure

The inner core was first discovered by *Lehman* [1936] using seismic data from the "core shadow." It has a radius of 1222 km and a density about 13 g/cm^3, and represents 1.7% of the mass of the Earth. Recent studies have shown that the inner

core is anisotropic with respect to an axis approximately the same as the rotation axis. Moreover, *Song and Richards* [1996] and *Su et al.* [1996] have proposed that the inner-core is rotating relative to the outer core based on seismic differential times of PKP phase families(Figure 5.1). However, to resolve the differential spin rate requires detailed knowledge of the inner core anisotropy. It looks complicated due to the hemisphere variations and scatter of the PKP time picks as noted by *Tanaka and Hamaguchi* [1997],*McSweeney et al.* [1997], and *Creager* [1996]. In Chapter 5, we propose an interpretation of PKP (DF and BC) data in terms of a transitional mostly isotropic structure (upper inner core) surrounding the anisotropic (lower inner core) inner core with possible variations in the thickness and velocity change. Evidence shows that a 300 km thick upper inner core overlying an anisotropic (5%) inner core will produce synthetics compatible with data at the range of 146° to 152° recorded on northwestern North America stations from south Sandwich events.

Chapter 2 Modeling D″ Structure Beneath Central America with Broadband Seismic Data

2.1 Abstract

Deep South American events recorded at distances between 70° and 96° are used to constrain the lower mantle structure beneath Central America. Employing data from the TERRAscope, BDSN, IRIS and CNSN (Canadian National Seismic Network) broadband arrays, we obtain a 1-D shear model with a 200 km thick D″ layer with a 3% velocity jump at the top and a negative gradient within the layer from broadband waveform modeling of SH-polarized S, ScS, and Scd. The shear structure above D″ is similar to the Preliminary Reference Earth Model (PREM) [*Dziewonski and Anderson*, 1981] in terms of dT/dΔ and S-SKS differential times. SV synthetics for this model, assuming a PREM core, produce a satisfactory fit to the data, except at the larger ranges to the north where the waveforms display rapid variation. This feature is indicative of lateral variation of the type suggested by *Grand* [1994], where the discontinuity becomes less well defined. Synthetics computed for a simplified 2D cross-section through this structure produce the Scd phase and simple S at larger distances. While Scd is easily observed in the shear wave data, there is little evidence of its counterpart in the P data. By testing several models with different P-velocity jumps at the same depth as the D″ jump in shear structure, we conclude that the velocity jump must be less than 1%. In fact, PREM provides an excellent fit both in timing and waveform shapes and therefore we conclude that lower-mantle structure beneath Central America shows clear evidence for a discontinuity in S velocity but not in P.

2.2 Introduction

D″ is an anomalous zone at the base of the mantle as defined by *Bullen* [1949] and marks the transition between the hot liquid iron core and the relatively cold solid silicate mantle. It has long been recognized as a dynamically important region of the Earth's interior and likely has physical properties at least as heterogeneous as the surface of the Earth. Long-period tomography studies have mapped apparent large scale variations [*Masters and Shearer*, 1992; *Su et al.*, 1994; *Li and Romanowicz*, 1996] in which the lowermost layer displays a high velocity ring around the Pacific which are usually interpreted as old subducted slab [*Loper and Lay*, 1995]. Alternative interpretations of these velocity anomalies suggest that the continents tend to align themselves on top of fast velocity regions causing the original normal regions to appear slow [*Anderson*, 1994; *Wen and Anderson*, 1995].

A related tomographic study by *Grand* [1994] at shorter wavelengths (~100 km) suggests a more complex picture where subducted slabs appear to be involved. This model and the ones discussed above also display large low velocity zones (LVZ), and one particularly large LVZ anomaly is located beneath the South Western Pacific. This large scale structure is underplated by a thin zone of ultra low P-wave velocity (10%) [*Garnero and Helmberger*, 1995, 1996; *Mori and Helmberger*, 1995] which appears to have D″ structure distinctly different than under the Americas, *Garnero et al.* [1993]. In short, the lowermost mantle is likely to be the resting place of subducted slab material and the origin of hotspot plumes. It will be difficult to understand the mineral physics and the dynamical properties of this zone, but we can start by attempting to derive the detailed properties of the P-SV and SH velocity structures with a particular geographical region at D″ depth.

While tomography models provide a large-scale description, waveform modeling can produce higher resolution helpful in understanding the dynamics of D″ structure. Due to the limited distribution of deep earthquakes and station locations, such modeling can only resolve CMB. Since *Lay and Helmberger* [1983a] first proposed D″ as a layer with 2-3% shear velocity jump about 300 km above the core mantle boundary

(CMB), based on the waveform modeling of World Wide Standard Seismograph Network (WWSSN) long-period records, numerous studies in both P and S have been conducted in a search for such a discontinuity. Long-period investigations have addressed the magnitude of velocity jump across the discontinuity while short-period studies have provided information on the sharpness of such features. Some long-period studies that find the discontinuity in S include *Young and Lay* [1987, 1990], *Gaherty and Lay* [1992], *Garnero et al.* [1993], *Kendall and Shearer* [1994] and others, while short-period studies suggest that this discontinuity is very sharp, as in *Lay and Helmberger* [1983a]. The P discontinuity is more easily studied with short period records, such as in *Wright et al.* [1985], *Baumgardt* [1989], *Young and Lay* [1989]; *Vidale and Benz* [1993]; *Houard and Nataf* [1992, 1993]. *Davis and Weber* [1990]; *Weber* [1993]; *Kendall and Nangini* [1996] also found evidence for the discontinuity using broadband records. There is little indication of the D″ discontinuity for some other geographical regions [*Wysession et al.*, 1992; *Weber*, 1993; *Vidale and Benz*, 1993; *Mori and Helmberger*, 1995]. *Weber* [1993] has shown with broadband records from the Gräfenberg array that beneath Russia the P and S velocity structure do not correlate, while *Wysession et al.* [1992] analyzed long-period diffracted P and S waves and with similar conclusions. However, these studies involve many events, in which the P and S data generally involve different geographical regions. Thus, considering the highly heterogeneous D″ structure, samples from the same region are particularly appropriate.

A broadband study by *Zhang and Lay* [1984] used SH recordings from Southern California for Argentine events, and found the D″ discontinuity to be a 2.75% velocity jump 250 km above CMB with zero velocity gradient in the layer. We extend this region to the north and use the modern broadband stations recently deployed. Three component seismograms recorded on the TERRAscope and BDSN arrays for each event are used to ensure that P and S sample the same region. Dealing with array data from a single event eliminates the need to address various source time functions, mechanisms, and assorted baseline shifts. This was not possible until the recent development of modern broadband stations because old WWSSN instruments had a

limited dynamic range which made it difficult to obtain satisfactory recording for the same event on both short-period and long-period instruments.

The D″ region addressed in this study lies beneath the western edge of Central America (Figure 2.1). In addition to the BDSN and TERRAscope network (BB network), we also include four CNSN stations (PMB, PGC, EDM, and WALA) and four IRIS stations (COR, TUC, ANMO, and CCM). We chose these stations because their azimuth is very close to that of BDSN and TERRAscope stations (except CCM, which we chose because it is closer to the event and therefore less sensitive to D″ structure). The azimuth of the stations in the BB network are between 316° and 320° relative to our primary event (5/10/94, h=605km), and about 326° to 330° to the CNSN stations. Two other auxiliary Argentine events (4/29/94, h=570km and 8/21/94, h=580km) are displayed in this figure as triangles which were used to help resolve the reflection from the D″ layer in SV and P waveforms. Figure 2.1 is a Mercator projection and does not reflect the azimuth for those CNSN stations very well due to the distortion at higher latitude. Also included in Figure 2.1 are the tomographic velocity anomalies in gray-scale background according to *Grand* [1994] for the lowermost mantle. Note the faster-than-average velocity beneath the Caribbean, which is sampled by the raypaths from this study. The raypaths of P and S from the same event to the same station may sample different depths (by 150km) when bottoming above the D″ layer. But in the D″ layer zone, they are very close together if the D″ layer is a typical "Lay-type" structure.

2.3 Observations

The broadband responses produced from the above instruments are generally proportional to velocity in the frequency range we are interested in and have a high signal to noise ratio. As an example, we display the three components of such motions for the 5/10/94 Argentine event recorded at Pasadena band-passed between 0.005 Hz to 4 Hz to suppress aliasing affects, *Kanamori et al.* [1991]. (Figure 2.2a). We deconvolve the instrument response to obtain displacement, and rotate horizontal EW

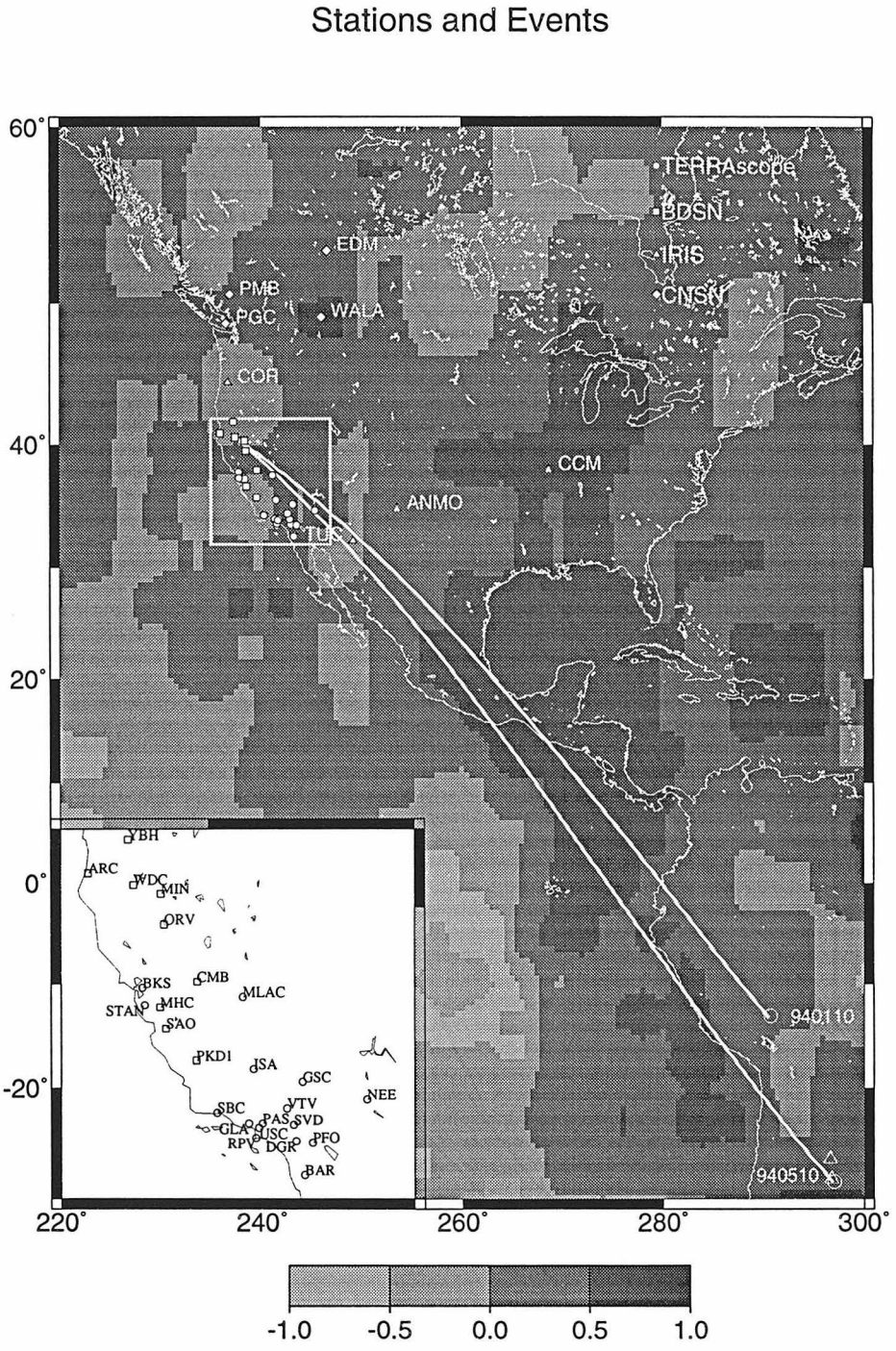

Figure 2.1: Map displaying the locations of the two major south American events, North American stations (circle) and two auxiliary events (triangle) used in this study. Inset contains the TERRAscope and BDSN stations. The background gray-scale is the velocity anomaly(δv/v, in percentage) based on the *Grand* [1994] 3-D tomographic model. The D″ region sampled is roughly the midpoint of the corridor as indicated.

and NS components into radial and transversal components(Figure 2.2b). The P phases such as P, pP, sP, PP are particularly strong on the vertical component but also recognizable on the radial, as expected for this range. In contrast, SKS and S_V are stronger on the radial component. Unfortunately, a relatively strong coda generally follows S_V which appears to be the complex signal containing SP and PL waves trapped in the local crust [*Langston*, 1996]. This complexity is generally the reason for the concentration on P and SH waveforms (rather than SV) in both structure and source studies. Ideally, SP will not be observed on the transverse component for an isotropic Earth which appears to be roughly the situation. The complex nature of SP can be seen in Figure 2.3 where we have included the Bolivia event (01/10/94, h=589km) to increase the range of samples, and observe move-out on the different components. Records with ranges less than 75° are from the 1/10/94 Bolivia event, and the others are from the 5/10/94 Argentine event. These two events have different source mechanisms so that the polarity of the P waves are opposite, while the S waves have the same polarity. All three panels are plotted with a reduced velocity of 13.4 km/s so that the S arrival move-out is nearly zero. The window includes the S waves, Scd, ScS, SKS, SP(a phase follows the S wave as indicated in the figure), and their coda. Several dashed lines are added to indicate different arrivals. The travel time of SP is most obvious in the vertical component, the SKS on the radial component and S and ScS on tangential component. The SP phase appears quite variable in both arrival time and shape. Fortunately, we are primarily interested in S, SKS, Scd and ScS which occur before SP at ranges beyond about 71°. However, it is important to be aware of the possible contaminations of ScS at the smaller distances. The bottom portion of this figure, also shows some of the problems with rotation where some small arrivals along the dashed lines (transverse) indicates some SKS motion. Such effects can be caused by anisotropy in the upper mantle as suggested by *Vinnik et al.* [1984] and *Silver and Chan* [1991]. Since SKS on the transverse component is quite small for most of the stations and the anisotropy in TERRAscope stations is generally similar [*Liu et al.*, 1995], we will assume isotropic upper structure in this investigation.

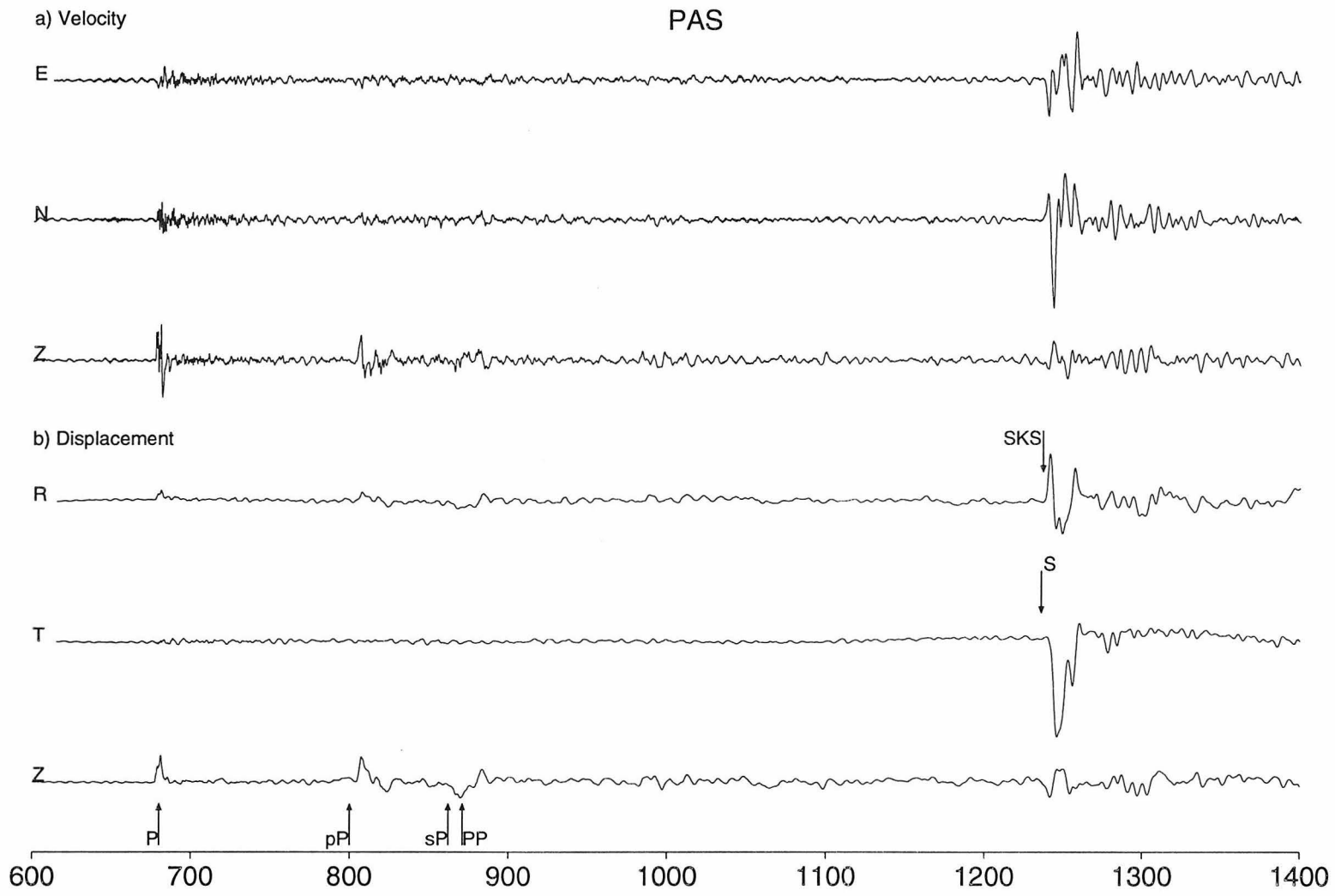

Figure 2.2: Broadband record from the Argentine event recorded at Pasadena (Δ=81.2°); a) original record of three components and b) deconvolved to displacement and rotated. The principle phases are indicated.

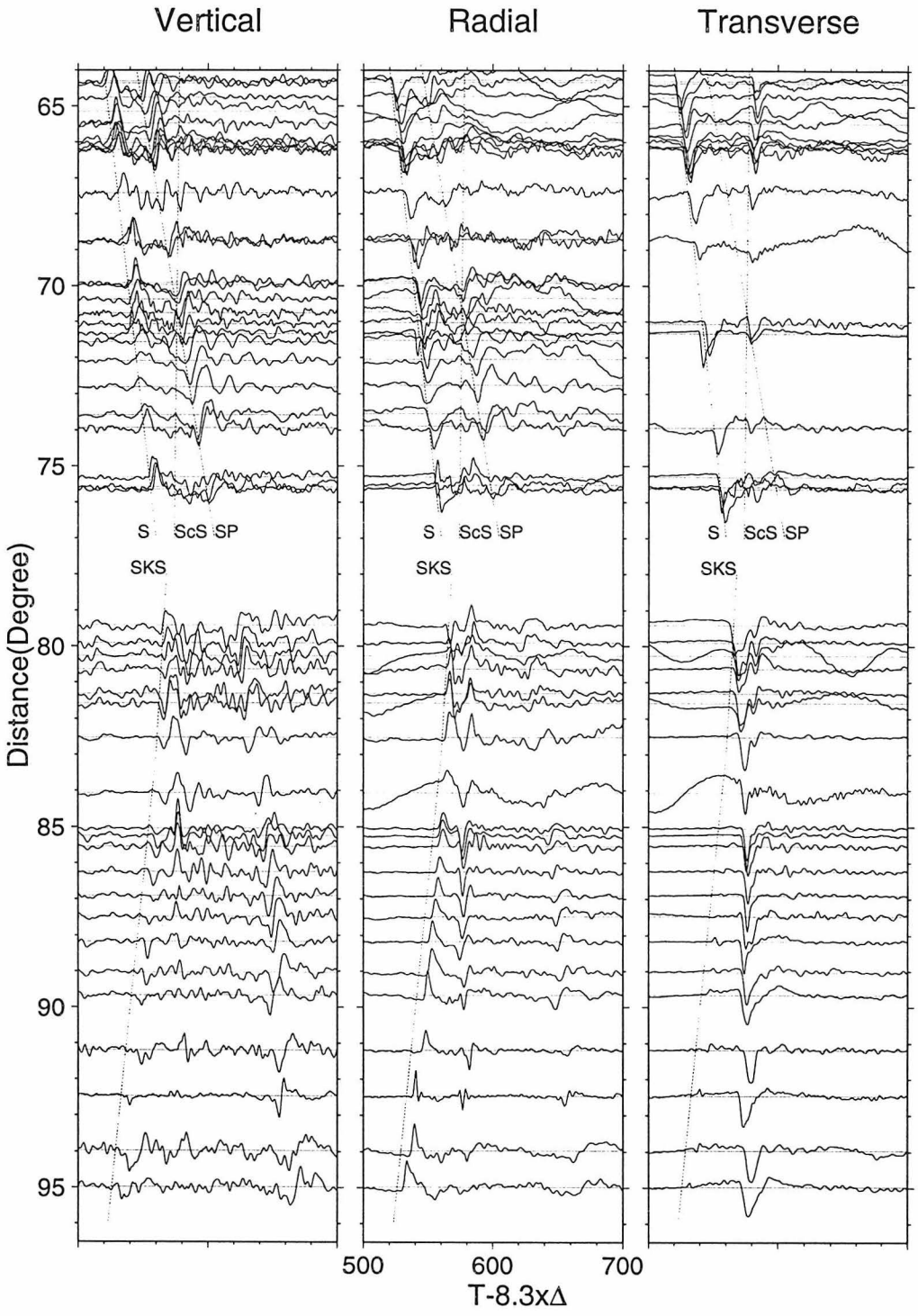

Figure 2.3: Three component record sections from the Bolivia event and Argentine events. The time window is chosen to display the cross-over of the SP and ScS phases at 70°. Reference lines have been added to emphasize the major phases.

2.4 Travel time analysis

The Bolivian event was used as a reference event, since it is closer to the stations and the raypaths sample lower-mantle structures from 800 km to 1300 km above the CMB, and hopefully, sample a less complex region. We study the travel time residuals relative to IASP91 [*Kennett and Engdahl*, 1991], though the result should not depend on the model. We pick P travel times on vertical component, S on transverse component and SKS on radial component after the SKS-S crossover. These picks were determined from the arrival onsets as measured from the velocity records. We define the travel time residual to be the difference between the travel time we pick and the travel time predicted by the IASP91; Positive values indicate the phase is late. Both P and S residuals for the two events and SKS residuals for the Argentina event are displayed in Figure 2.4 along with the P station corrections obtained from *Dziewonski and Anderson* [1983] hereafter, referred to as DA83. In DA83, they define the station time corrections in terms of a static part and azimuthal dependent part, the sums of which are given in the plot. The static term dominates the corrections at all stations, except at station WDC. The static part is generally considered to be caused by crustal anomalies, however, the azimuth dependent part may be caused by deeper structure. The P residuals for the two events track each other well and agree with DA83 predictions. The offset of these observations with DA83 can be easily explained by a shift in origin time (or change of source depth) and translated as a baseline shift. Thus, the Bolivian residuals which should not be affected by the D″ layer can be used to correct the Argentina record section.

In contrast to the P-wave travel times, the S arrivals scatter significantly over the ranges 70° to 80°. For example, ANMO shows the residual difference of more than 5 seconds, TUC has about 4.5 seconds, while PAS has less than 1 second residual. Such scatter should not be caused by travel time picking errors, which are estimated to be less than 0.5 sec. We can attribute the scatter in these residuals to three possible sources, earthquake source region, receiver and the mantle path. The receiver portion of the path is obviously common between the two events and this should be apparent

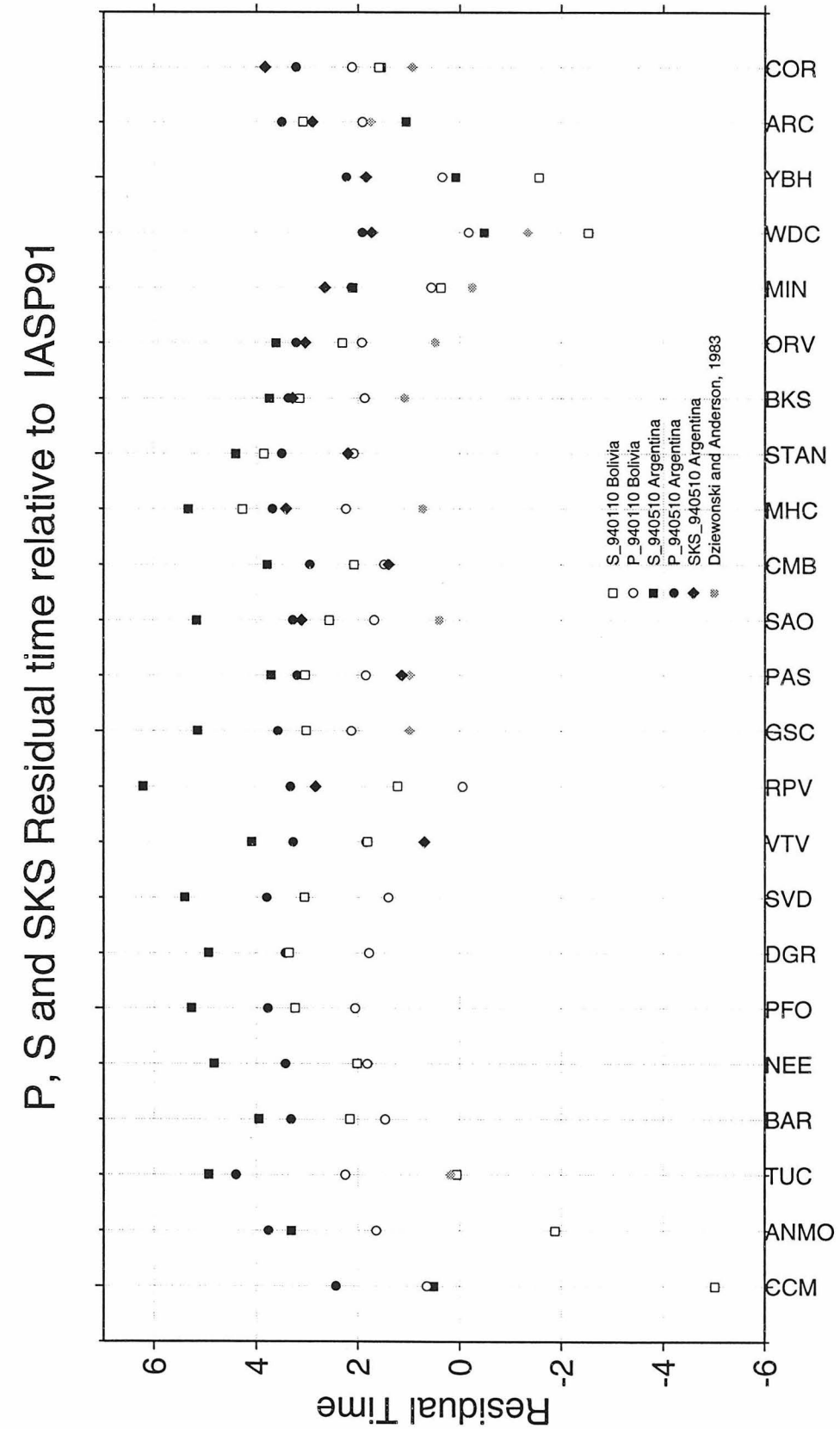

Figure 2.4: Plot of P, S and SKS residual times as picked from the velocity traces. P is from the vertical component. SH is from the tangential component and SKS is from the radial component. The predicted P travel-time delays from *Dziewonski and Anderson* [1983] are included for comparison.

as a static offset between stations. The source portion could be assumed to be similar since the azimuth difference to the stations is not great. Therefore, the rather large scatter of S residual differences between the two events indicates that structure in the lower mantle may contribute as well, which makes the station correction for S difficult. Inspection of SKS travel times shows that SKS residuals behave similarly to S at closer distances, but are not as large as at stations MIN, WDC and YBH, where the S residuals are rather large for both events. This again confirms that we are dealing with a complex S structure, perhaps near these stations. Since it is difficult to resolve this problem due to the limitations of the data, we choose not to make any station corrections for S, but to simply flag the timing problems associated with these three stations. S-SKS differential times at these stations are used to constrain the structure. We have included three other U.S. stations in the travel times plots for reference, namely ANMO, CCM and TUC. Both ANMO and CCM show very strong differences between the events presumably caused by the well-known Caribbean anomaly, *Jordan and Lynn* [1974] and others. No corrections were applied to the Canadian stations at this stage of our study since only their waveforms were used.

2.5 Waveform modeling

We employ the same forward modeling strategy as *Lay and Helmberger* [1983a]. However, here we have dense broadband record sections so that the velocity structure in the lower mantle and D″ are better constrained. We find that the travel times of the various record sections before the sampling of the fast D″ structure satisfy the predictions from PREM. The actual SH triplication data look very much like that from *Zhang and Lay* [1984] and therefore, our preferred model looks like PREM but with a modification of the D″ structure, see Figure 2.5.

Following *Young and Lay* [1987], the velocity decrease below the D″ velocity jump is added to comply with the simplicity of long range diffracted waveform shape. The model SZL by *Zhang and Lay* [1984] along with PREM and our preferred model SDH

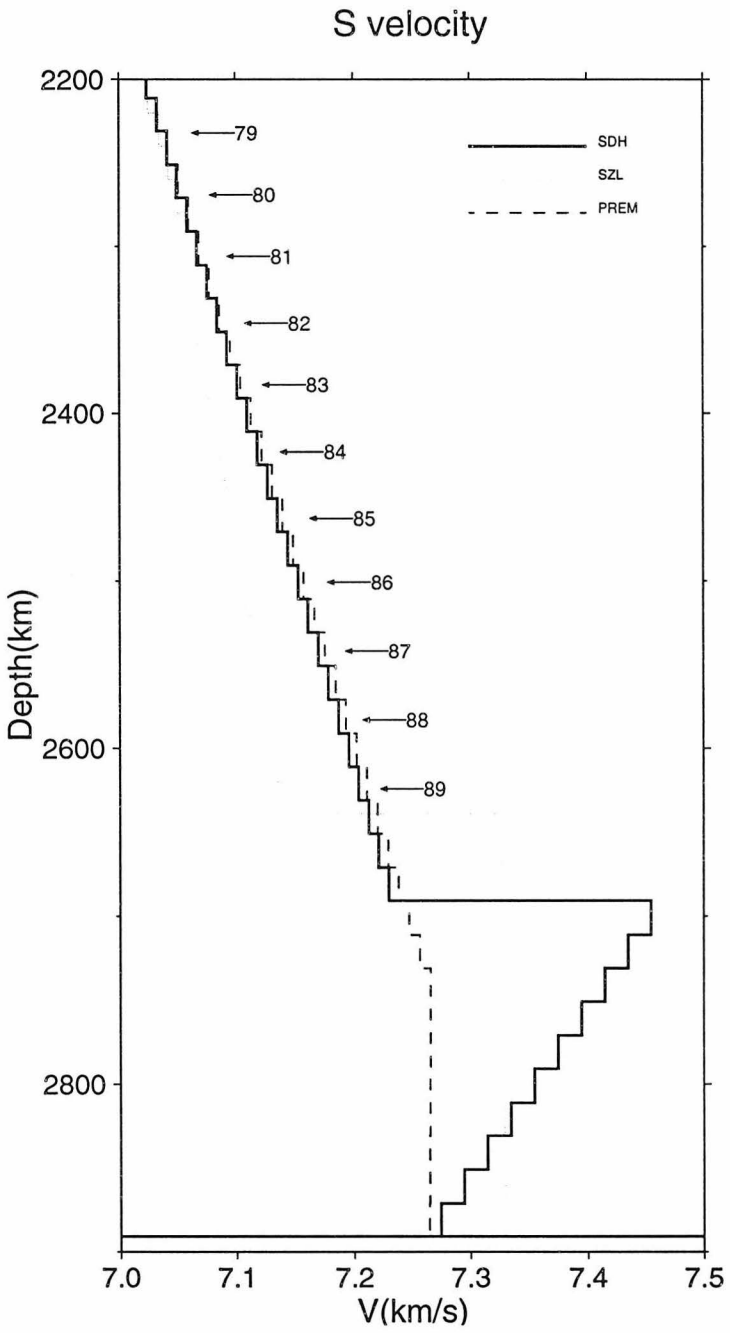

Figure 2.5: S velocity models of PREM [*Dziewonski and Anderson*, 1981], SZL [*Zhang and Lay*, 1984] and our preferred model, SDH. SZL has a gradient reduction relative to PREM from a depth of 2200 km and a 250 km thick D″ layer with 2.75% velocity jump, in which the gradient is zero. SDH follows PREM till the depth 200 km above the CMB, where the S velocity increases by 3% and the velocity gradient in the layer is negative. Arrows indicate the depth where the S bottoms for different epicentral distances. After 84°, Scd crosses over S and becomes the first arrival.

are displayed in the figure. Our model has a thinner D″ layer (200 km thick), a 3% velocity jump, and a negative velocity gradient in the D″ layer. The S travel time curves for these three models displayed in Figure 2.5 are plotted in Figure 2.6. As labeled in the figure, the solid line is derived from SDH, the dotted line for SZL, and the dashed line for PREM. Lowercase letters indicate the triplication points produced by the D″ discontinuity which only apply to SZL and SDH. There are two major differences between SDH and SZL. One is that the point where SKS crosses S is about a half degree further for SZL, and the other is that the S-wave arrives later for the SZL model beyond 86°. These modifications prove to be more compatible with the travel time data as displayed in Figure 2.6 and with the waveform data as demonstrated in the following presentation of record sections. Note that the two open circles are associated with the anomalous stations WDC and YBH. The depth where direct S (ab) bottoms is indicated in Figure 2.5. This model is quite similar to that proposed recently by *Kendall and Nangini* [1996] for a neighboring region to the east and will be discussed later.

2.5.1 S waveforms

A review of the polarization of our data indicates that the fault mechanism is probably not affecting our modeling. This is expected since the stations are nearly along a fixed azimuth and involve a limited range of ray parameters. Thus, it is likely that only the source time function and the velocity structure are controlling these seismograms. Since the direct S-wave at 70° is impulsive and not contaminated by D″ structure, we will simply use the first 15 seconds of the tangential S_H waveform at CCM as the effective source time history. Though the CCM station could be sampling the mid-mantle structure discussed by *Grand* [1994] and others, the frequency content of its S arrival does not show much difference from that of the other stations, and therefore should serve as a useful source description.

We used the Cagniard de Hoop generalized ray theory (GRT) [*Helmberger*, 1983] to generate the synthetics. The SH synthetics derived from SDH and SZL are displayed

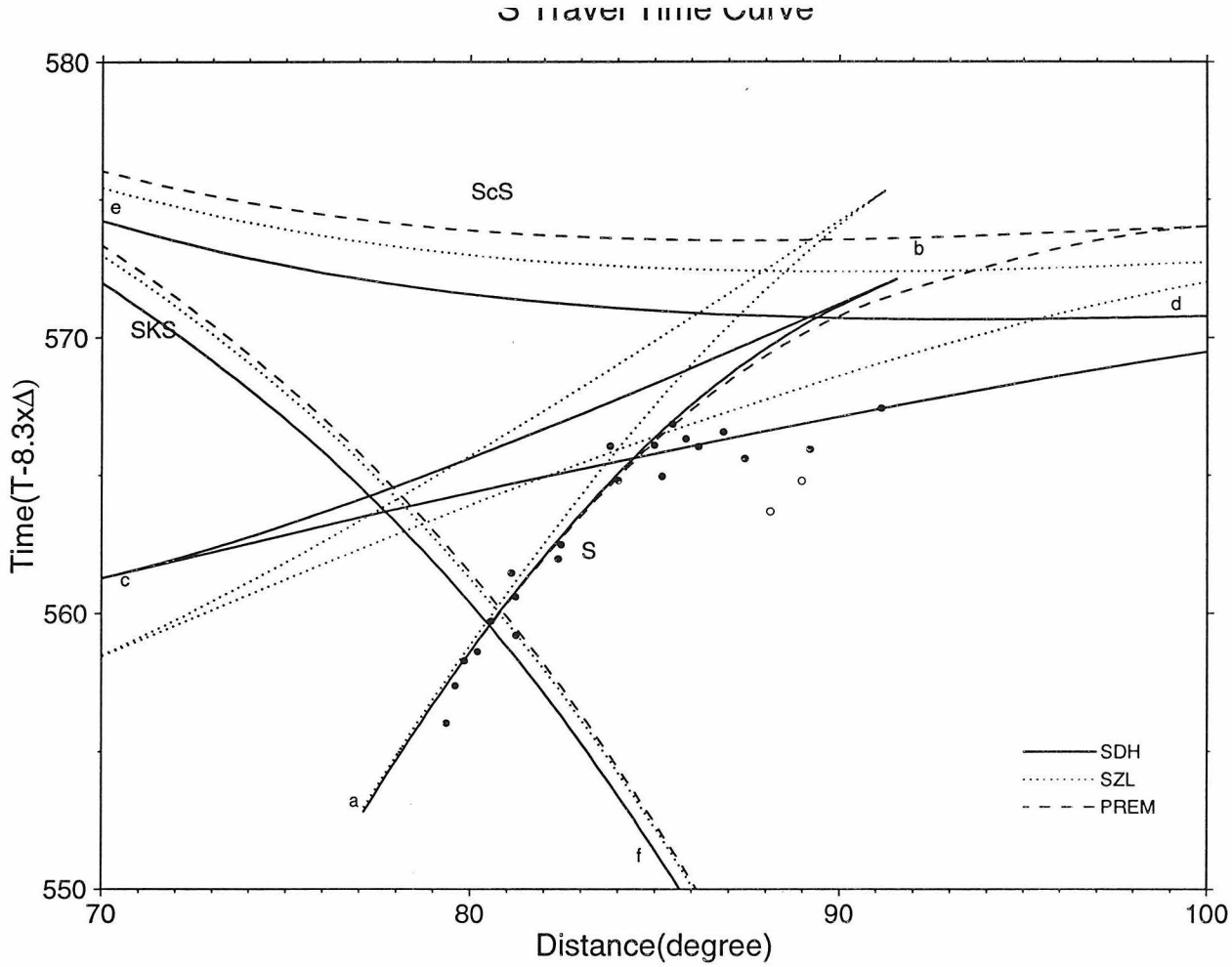

Figure 2.6: S travel time curves for the three models displayed in Figure 2.5. Solid line is for the model SDH, dotted line for model SZL and dashed line for model PREM. Lower case letters represent triplication caustics. For SZL and SDH, ab branch is the S wave going above the D″ layer, bc is the reflection off the top of D″ layer, cd is S wave sampling the D″ layer, de is ScS and ef is SKS. Three branchs are associated with the CMB discontinuity: ab for S in the mantle, be for ScS and ef for SKS. Also included are the travel time points for the 5/10/94 event. Open circles correspond to those stations having anomalous travel time.

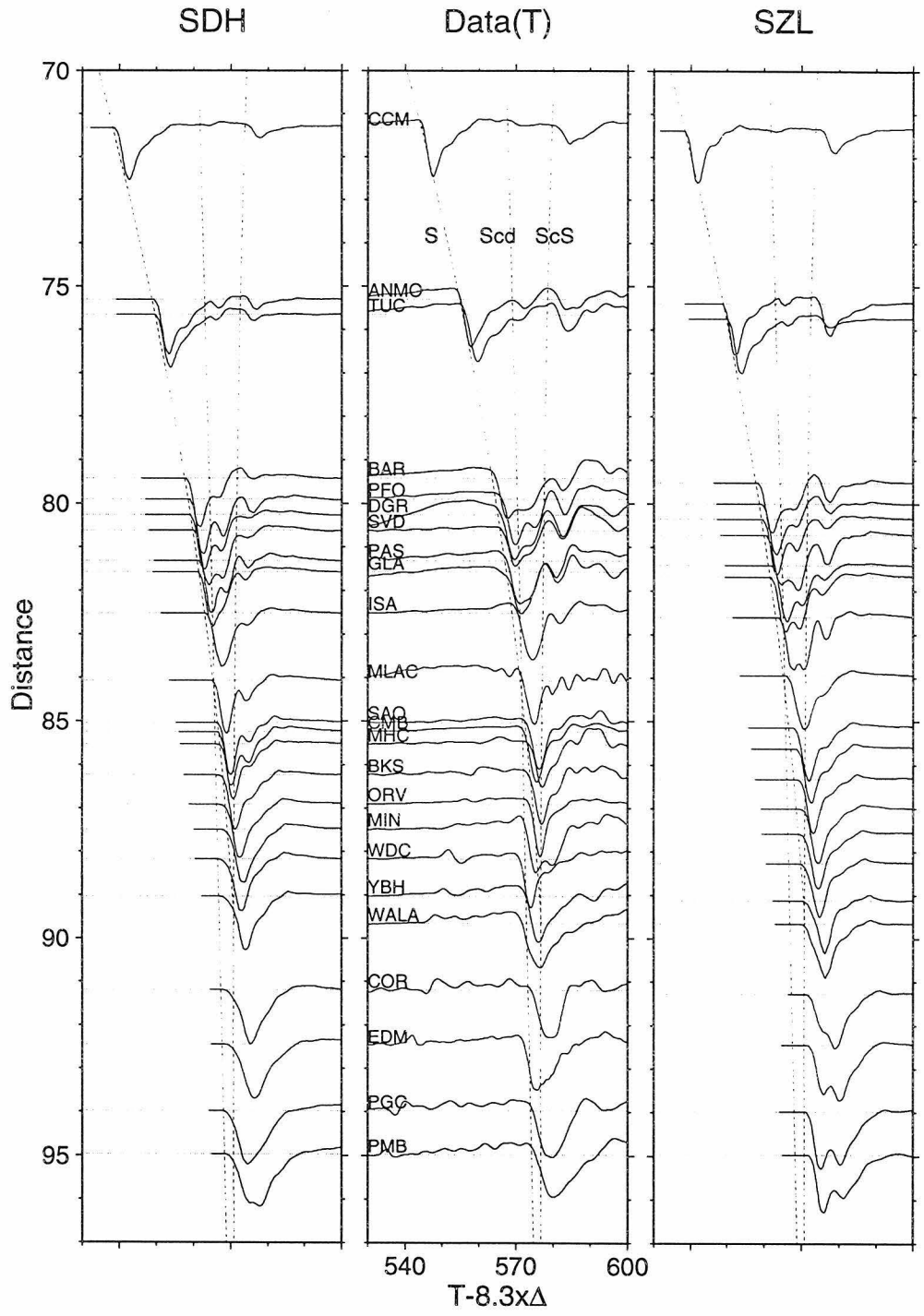

Figure 2.7: Comparison of synthetics from two models, SDH and SZL with the data for the transverse component. The dashed lines are S, Scd and ScS travel times as predicted by SDH. Both model show clear development of Scd from 70° to 80°. SZL predicts a stronger Scd at distance of 80° to 84°, while SDH fits the data well. After 84°, the first arrival of S from SZL is later than the data, whereas SDH fits better. After 90°, SZL begins to develop a double arrival not shown in the data.

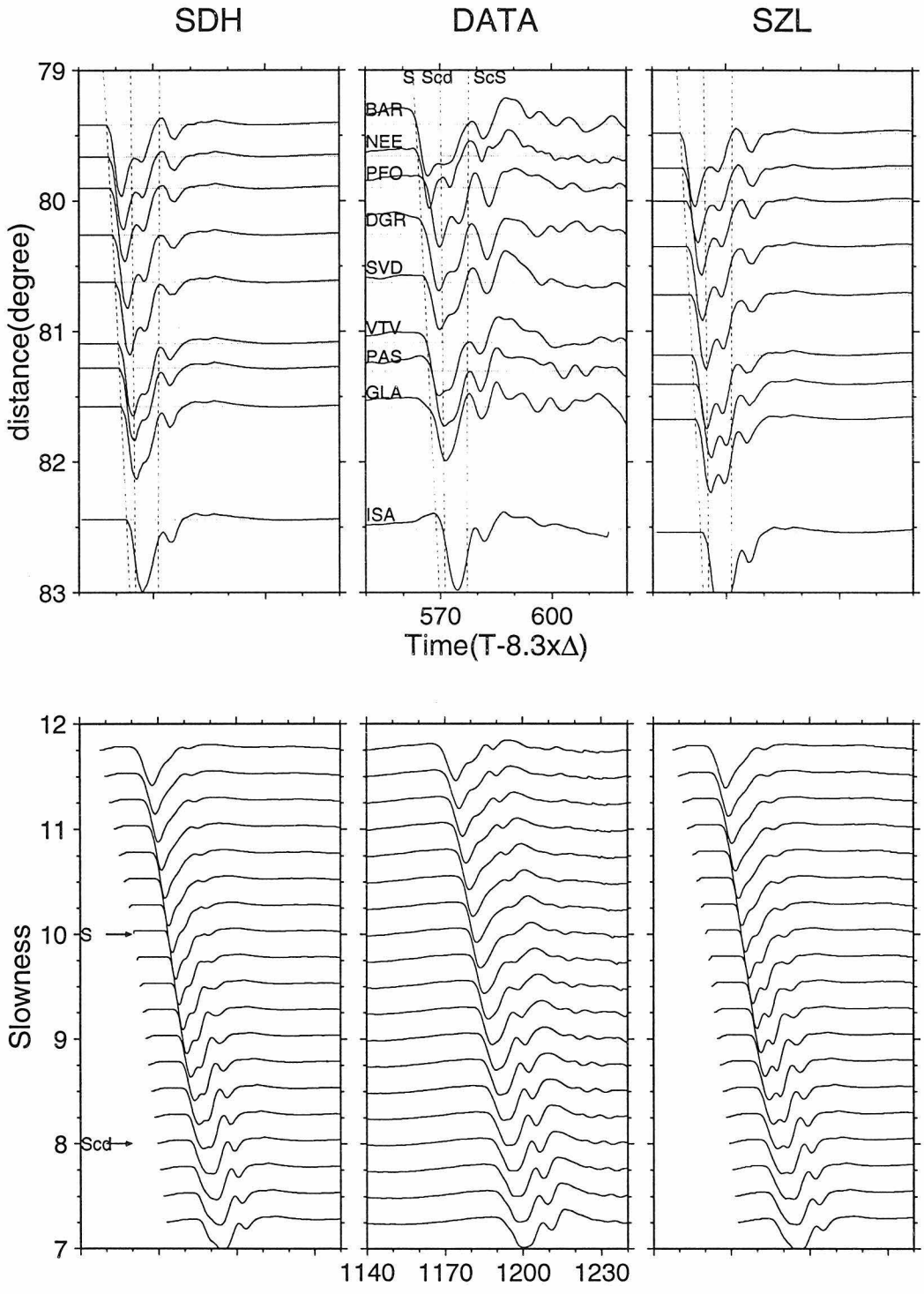

Figure 2.8: a) A more detailed record section of TERRAscope data from 79° to 83°, displaying the convergence of S and Scd. b) A slant-stack of the seismograms in (a). Arrows indicate the slowness at which S and Scd are theoretically most enhanced.

in Figure 2.7 along with the data in the middle panel. The dotted lines indicate the main arrivals, namely S, Scd, and ScS determined by the model SDH. These lines are displayed with the data in the middle panel with a baseline shift of 6 seconds applied. Such a baseline shift comes from the error in event location and origin time determination and the fact that the arrays we used are in a known tectonic region. Note that a base-line shift of 6 seconds alone is expected between the pure path models TNA (tectonics) and SNA (shield) as proposed by *Grand and Helmberger* [1984]. We also included these SDH reference lines on the SZL synthetics for ease in comparison. Both profiles of synthetics display a recognizable Scd phase beginning at about 75°. The Scd evolution is clearly demonstrated in the data. That is, at CCM (71.3°), there is hardly any Scd discernible but it becomes apparent at ANMO (75.3°) and TUC (75.7°), where S and Scd are well separated. The more distant stations (COR, EDM, PGC, PMB) show a single pulse waveform while SZL begins to develop a double pulse waveform which doesn't agree with our data particularly well. The SDH synthetics on the left better match the single pulse feature in the data observed at the larger distances. Note that, the difference between these two sets of synthetics at the larger distance is caused by the relative strength of the Scd branch. It is relatively weak for SDH because of the negative gradient in D″.

The concentration of records between 79° and 83° are shown in Figure 2.8. At these distances the Scd and S phases are close in time making differential time measurement difficult. However, the synthetics fit the complex observed waveform quite well as demonstrated by an overlay comparison. The Scd and S interference yields a single pulse at distances further than station GLA where SDH synthetics provide a good fit.

One of the biggest difficulties in detailed waveform modeling is properly accounting for the distortions caused by receiver structure. Earlier studies attempted to handle such problems by searching for stations with simple receiver function, see *Helmberger and Wiggins* [1971]. For example, we could pick those stations that have small P to S precursors produced by the crust-mantle transition. Such stations would help detect the precise distance where SKS cross over S but these stations may not be the most

transparent to the Scd phase. Thus, a more statistically justified method is to add more stations and stack the data at various phase velocities. As more stations are added we can expect to improve resolution. We stack 10 stations within 4°(79° to 83°) and compare predictions from our models to the data stack.

The S waveform stack is displayed in Figure 2.8(b). Theoretically, it will enhance S most when stacking with a slowness of 10 and Scd with a slowness of 8.0, which is slightly dependent on the model. Since S and Scd are not well separated, the Scd phase will not be seen as an isolated pulse at this distance range. However, SDH fits the data very well all through the slowness stacking as does the SZL model.

We used the SH waveforms to derive the model SDH and then generated SV synthetics from this model and SZL as displayed with the data in Figure 2.9. The source function is still the first 15 seconds of CCM SH record because it resembles most SKS arrivals at further distances. The dotted lines indicate S, Scd, and SKS as determined by model SDH. The SV component is much more complicated in the time window we are analyzing because there is another major phase, SKS, interfering with the already complicated S-Scd-ScS system. The travel time of SDH fits the data quite well after a base-line shift, while the SZL predicts larger S-SKS differential times than the data at large ranges. Both sets of waveforms fit very well at distances less than 89°, and the difference between SDH and SZL is not great. But at distances greater than 90°, the observed second arrival consisting of Scd, S and ScS shows more complicated behavior in timing and waveshape than predicted by either model. The Scd behavior is more difficult to trace due to the complicated interference of several major arrivals. But at 75°, Scd is still separated from S and SKS as pointed out earlier by Lay and Helmberger, 1983b. We illustrate this by showing the individual ray contribution and the data in Figure 2.10. One of the advantages of the GRT synthetics is that you can break down the rays that sample different depths to identify their contribution to the synthetics. The first trace labeled S is the synthetic generated by including only contributions of those rays sampling above the D″. The second trace labeled S+Scd includes those rays sampling the D″ layer, ScS and SKS are included in the third and fourth traces, respectively. The bottom trace is the observed TUC record. Reference

lines indicating the various arrivals are included. The beginning negative pulse before the SKS arrival is Scd, as shown by the synthetics. The initial upward pulse on the observed data is due to the S to P conversion at the Moho beneath the receiver. This feature is common in the observations but varies rapidly from station to station. Although this arrival is easily modeled, it doesn't add much to our understanding of D″. Its strongest impact occurs at the S-SKS crossover as displayed in Figure 2.11, where it interferes with SKS. In this figure we display the dense network coverage from 79° to 83° with the synthetics for both models. SKS overtakes S (crossover) as the first arrival at about 80.5° in the SDH synthetics. The crossover is slightly larger for SZL as discussed earlier and does not fit the data quite as well as SDH. The rather large arrival occurring about 20 seconds after the first arrival is not modeled well especially near the bottom of the figure. This phase is, also, quite strong on the vertical component, see Figure 2.3, suggesting that it is some type of PL-wave development.

The comparison of SDH and PREM is displayed in Figure 2.12, where the crossover for PREM is similar to that of SZL. Since it lacks the reflection from the D″ layer, the waveform for PREM poorly predicts observations in the 80° range. However, at distances greater than 90°, the second arrival, diffracted SV, is a simple pulse in PREM synthetics which fits stations COR and PGC better than the synthetics on the left. But the rapid change in waveform between COR and EDM is very difficult to explain with 1D models. Some of this waveform peculiarity is probably caused by the EDM receiver structure, as can be seen in Figure 2.3. EDM is the third trace from the bottom which appears to be singular in appearance compared to the others for all phases. However, such variations for paths connecting EDM to South American events has been noted earlier by *Lay and Helmberger* [1983a]. This type of feature suggests rapid variation in D″, as discussed below.

We take advantage of broadband data by convolving with the analog broadband instrument used by *Zhang and Lay* [1984], which removes both long period source

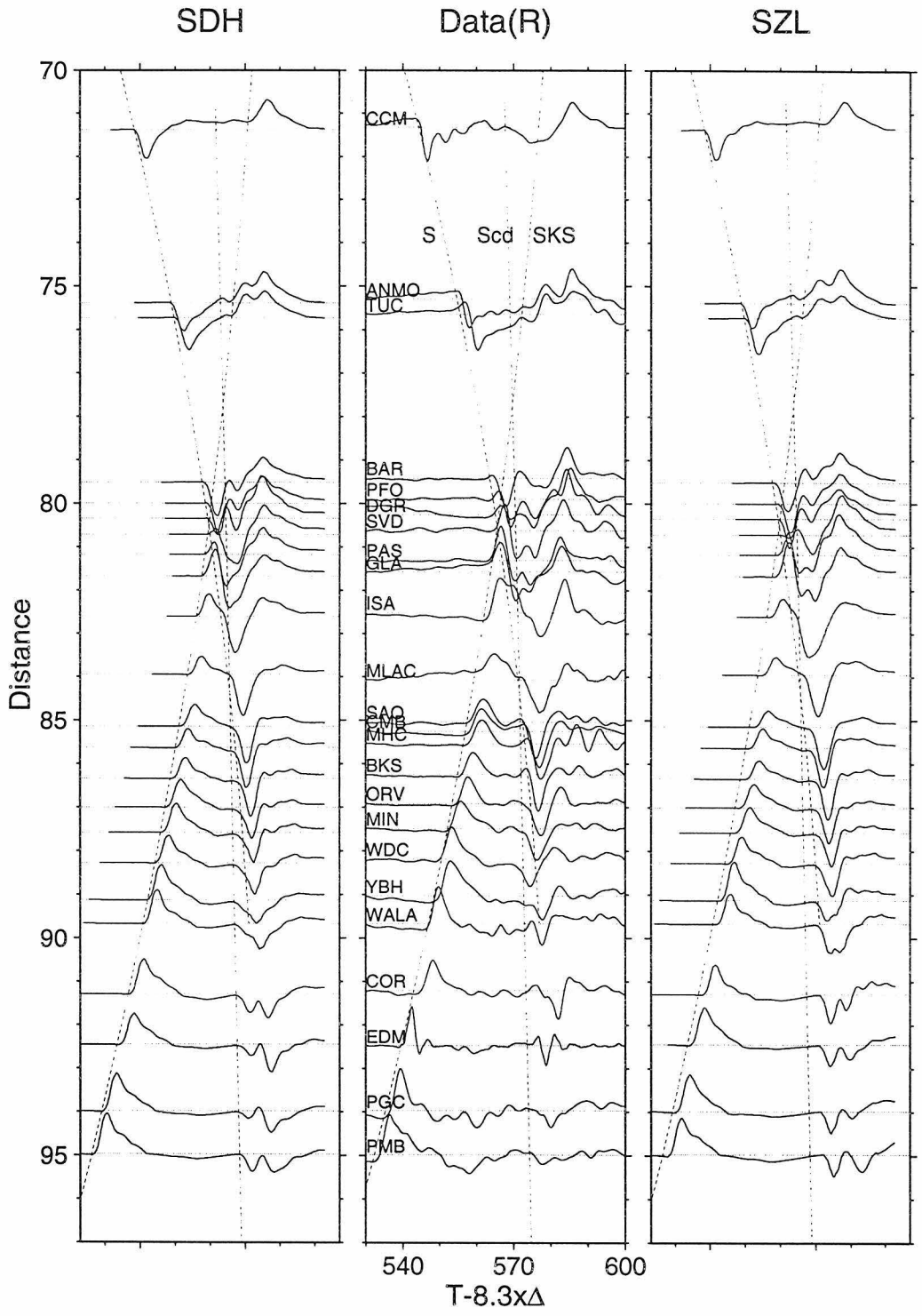

Figure 2.9: Comparison of synthetics from models SDH and SZL with the SV data, as observed on the radial component. Both models fit the data well at distances less than 84°, but at larger distances, SDH better predicts SKS-S differential time. Both models show complicated SV waveforms not observed in data.

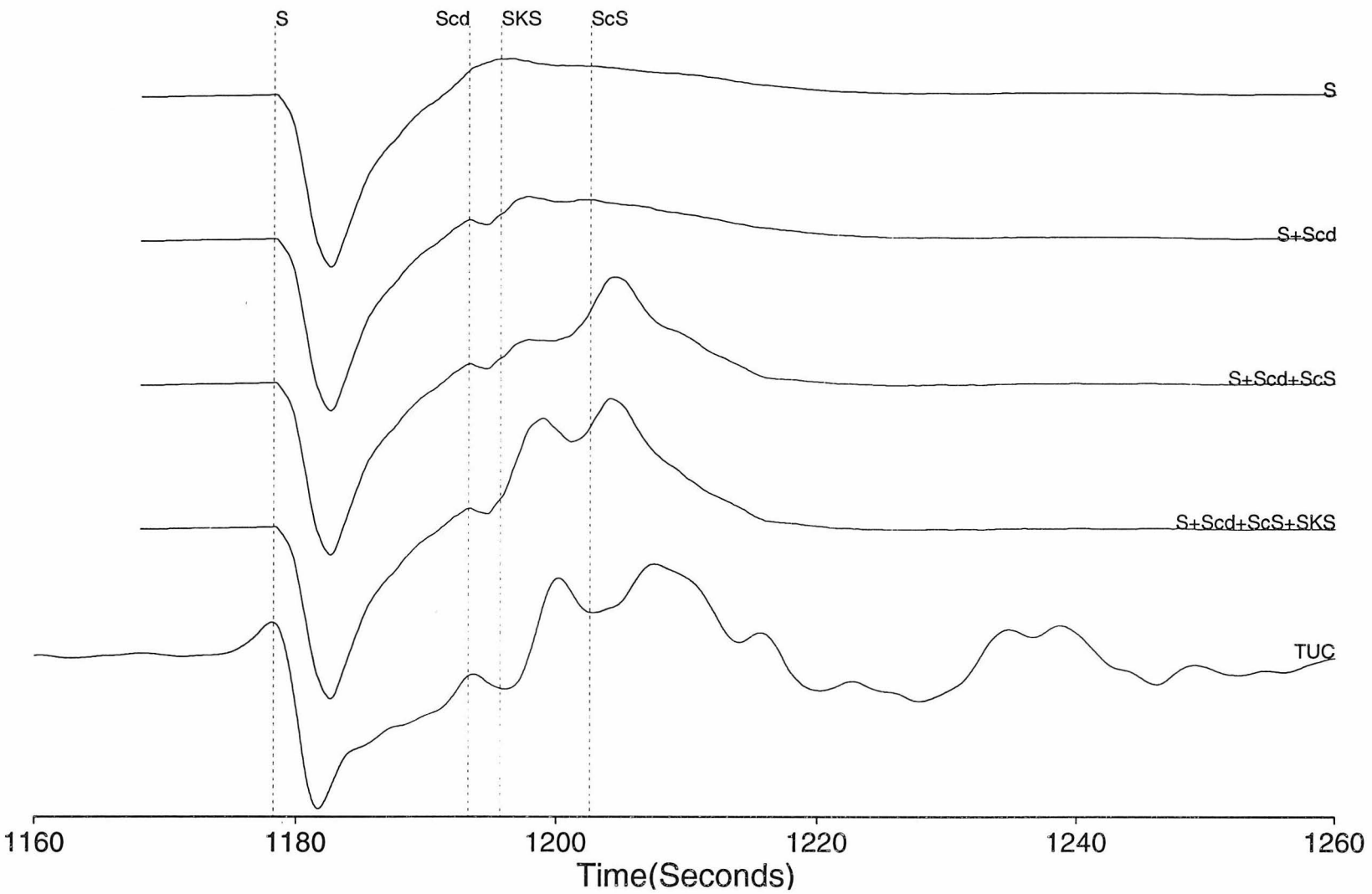

Figure 2.10: Detailed construction of the synthetic in terms of ray contributions compared to the record at station TUC. At this distance, Scd arrives earlier than SKS and is observable in data.

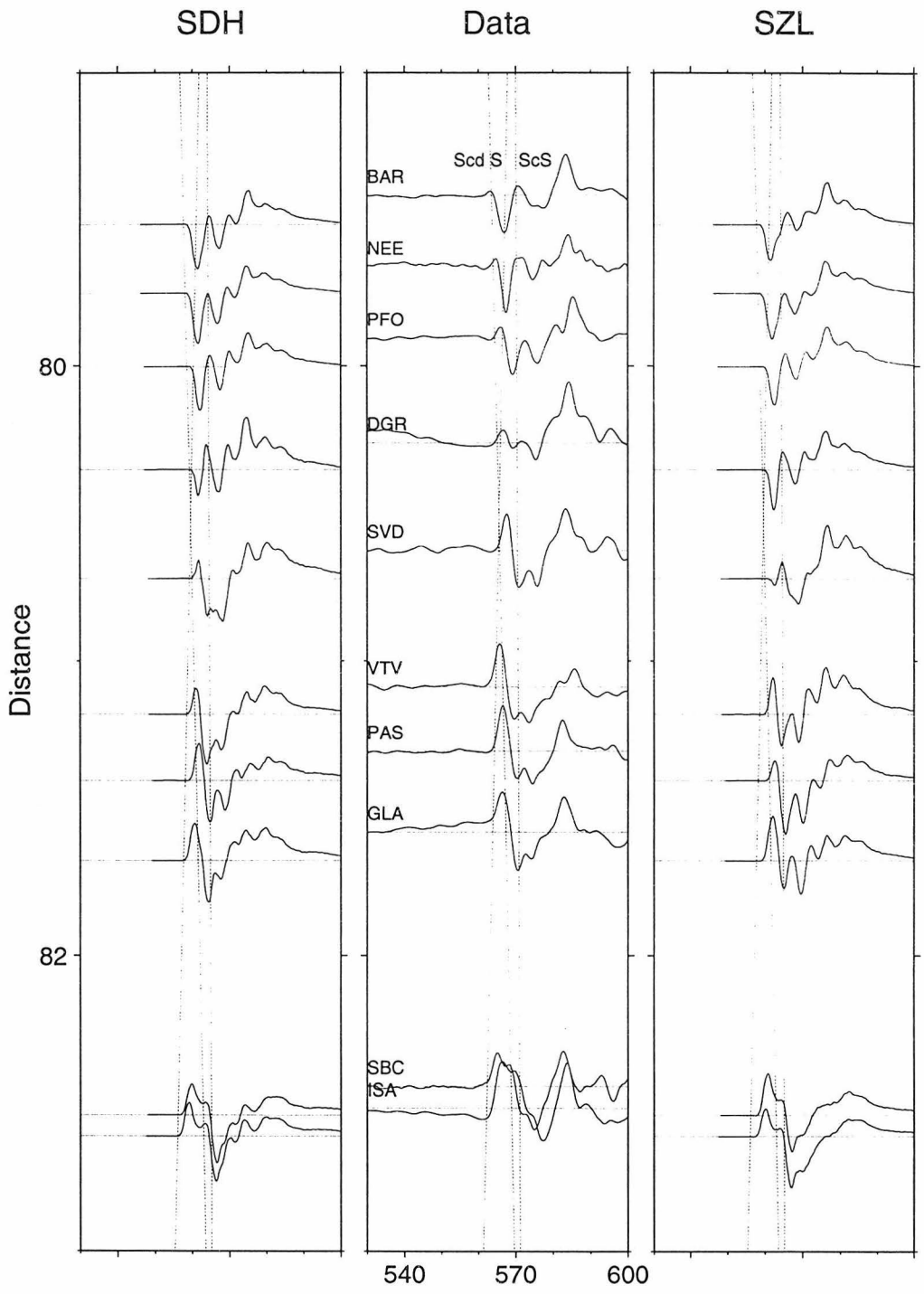

Figure 2.11: Detailed comparison of the TERRAscope array data at the cross-over distances (S to SKS) assuming the CCM SV source history. The change of polarity indicates where SKS becomes the first arrival. Dashed lines are predictions of S, Scd and SKS travel times from the SDH model.

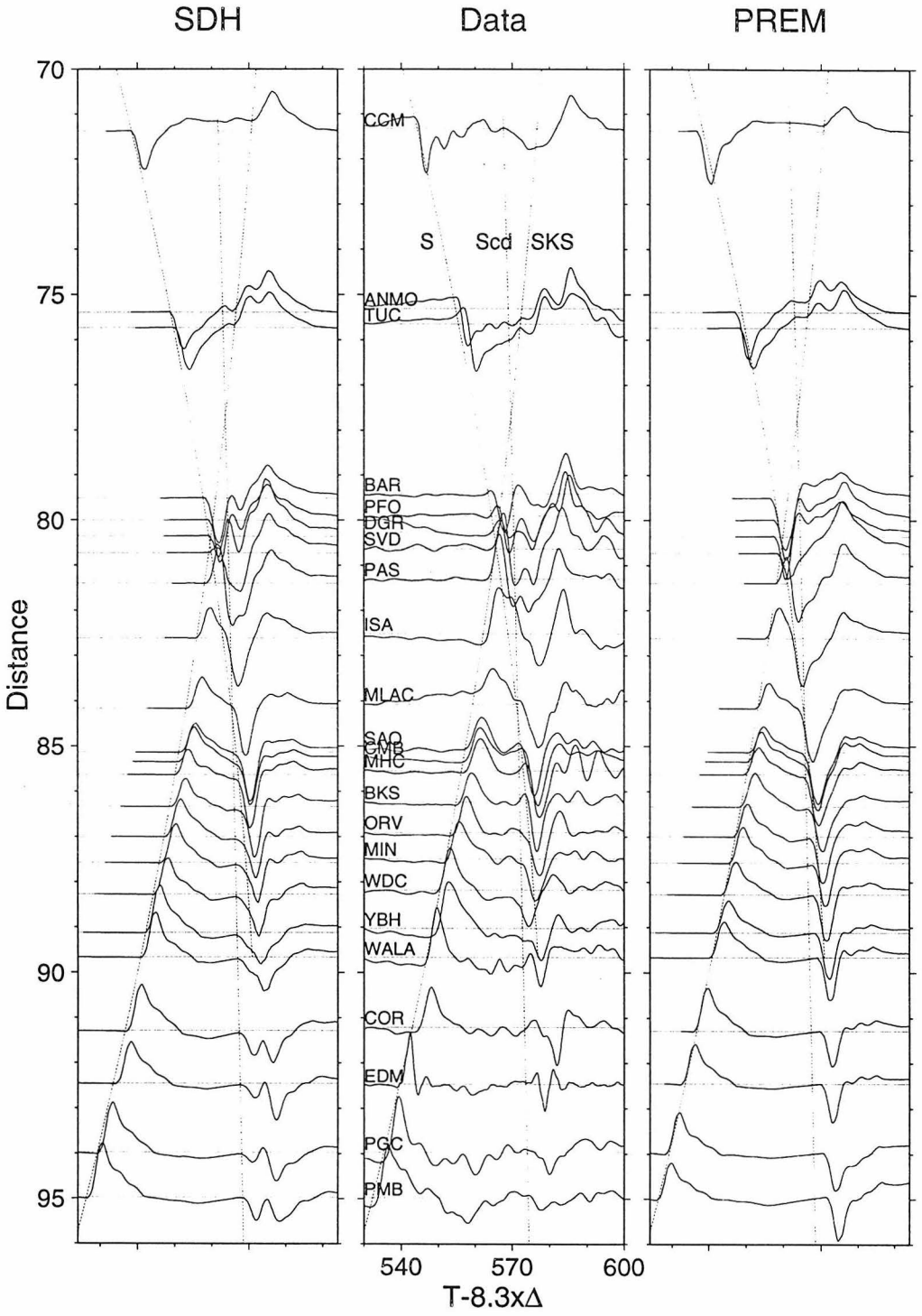

Figure 2.12: Comparison of synthetics from the two models SDH and PREM with the radial SV data. Note that at distances beyond 90° PREM shows a simple SV arrival that fits data better than SDH.

complexity and short period scattering so that Scd phase is easier to recognize near SKS-S crossover. Applying this short period filter allows better separation of Scd from the other phases and produces a reasonably coherent line of peaks. Both radial and tangential components are displayed in Figure 2.13, in which we include black dots to indicate the pick of Scd on tangential components and white dots for ScS. In the upper panels, which is the records from the 5/10/94 Argentina event, we also include dashed lines to indicate S, Scd, SKS arrivals predicted by the model SDH. The Scd arrivals are evident in all records and our model SDH predicts their timing quite well. The best time window to observe Scd on the radial component is where SKS crosses over S and cancels each other. At this distances, Scd is relatively separated from SKS and S, therefore, easy to observe as seen at DGR, SVD. Records from another event (04/29/94, depth=573km) about 0.1° from the 5/10/94 event is processed the same way and displayed in the lower panel. Again, records at station DGR and SVD show clear Scd arrivals on the radial component although again slightly delayed, perhaps indicative of some anisotropy. The ScS arrivals on the radial component appear later than that on tangential component, and are phase shifted relative to the tangential component. A fast layer with 5% increase in shear wave velocity with a thickness of 20 km above the CMB beneath the Caribbean has been proposed earlier to explain such an effect by *Mitchell and Helmberger* [1973], and fits our data as well. A similar structure beneath southern Alaska has been proposed by *Lay and Helmberger* [1983b]. The apparent shift in ScS_V relative to ScS_H predicted by this type of modeling can be explained by about 2.5% anisotropy in the bottom 100 km of mantle as suggested by *Doornbos et al.* [1986].

Overlays of the tangential (solid) with the radial (light) aligned on SKS for the two events are displayed in Figure 2.14. There is substantial SKS on the tangential component at some stations, e.g. BKS etc. Such features have been explained by mantle anisotropy [*Silver and Chan*, 1991]. The large second arrival consisting of Scd, S and ScS should have similar onsets assuming isotropic behavior, which is generally observed except for the two most distant stations, YBH and ARC. This suggests that the anisotropy structure is confined mostly to the bottom of the mantle. However,

since this waveform is formed by the interference of several arrivals it is easily affected by lateral variation and scattering.

2.5.2 P waveforms

As mentioned previously, we do not see much evidence for a Pcd phase. Thus, we have simply assumed constant Poisson's ratio (σ=0.3) and generated three models similar to SDH but containing velocity jumps of 1%, 2%, and 3%, denoted by PR1, PR2, and PR3. The comparison of PR3 and PREM with the recorded vertical component of displacement is displayed in Figure 2.15. As in the S-wave modeling, we choose the waveform at CCM and applied an attenuation factor with t*=0.4s to smooth it so that its frequency content is similar to most of the other waveforms as the representative of a source excitation or regional correction [*Lay and Helmberger*, 1981]. Unfortunately, the source is rather complex in its frequency content, but the width of the waveform is stable across the array. These complexities were not so noticeable in the S waves because of the extra attenuation encountered. The dotted line indicates the P-wave onset appropriate for PREM and was included in the other panels for reference. The residuals determined by the travel-time analysis of Figure 2.4 were applied to the various stations from TUC to COR along with a 4 seconds baseline delay. This baseline shift apparently accounts for the difference of upper mantle structure beneath the arrays relative to PREM and perhaps some offset due to the error of the source location and origin time determination. Although many models were considered, we choose PREM and PR3 to display because PREM proves effective and PR3 corresponds to SDH. However, while PREM fits the travel time very well, PR3 does not. The triplication which is obvious in PR3 synthetics does not appear in the observations. Furthermore, the phase PcP in the PR3 synthetics is too strong because of the strong negative gradient at the base of the mantle, a feature not evident in data. In short, while the observed waveforms are complicated, no Pcd phase could

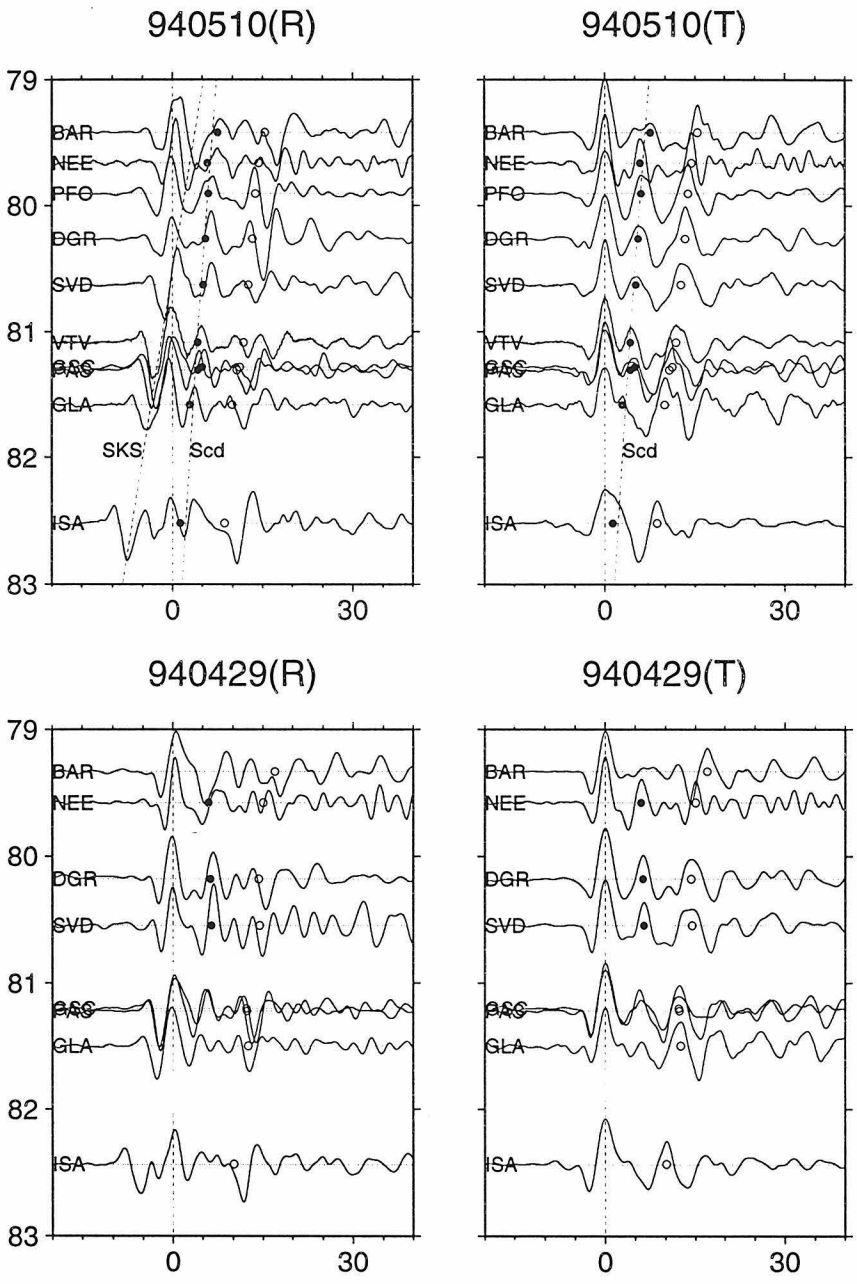

Figure 2.13: Radial and tangential velocity records from 79° to 83° convolved with a Wood-Anderson long period response. Records are lined up on the S peak in tangential component for the 5/10/94 event (upper panel) and the 4/29/94 event (lower panel). The black dots are the Scd pick from the tangential component, and white dots are ScS. The computed travel times of S and Scd from model SDH are included in upper panels. In the upper left panel, SKS is also included. Scd is clearly shown in the radial component.

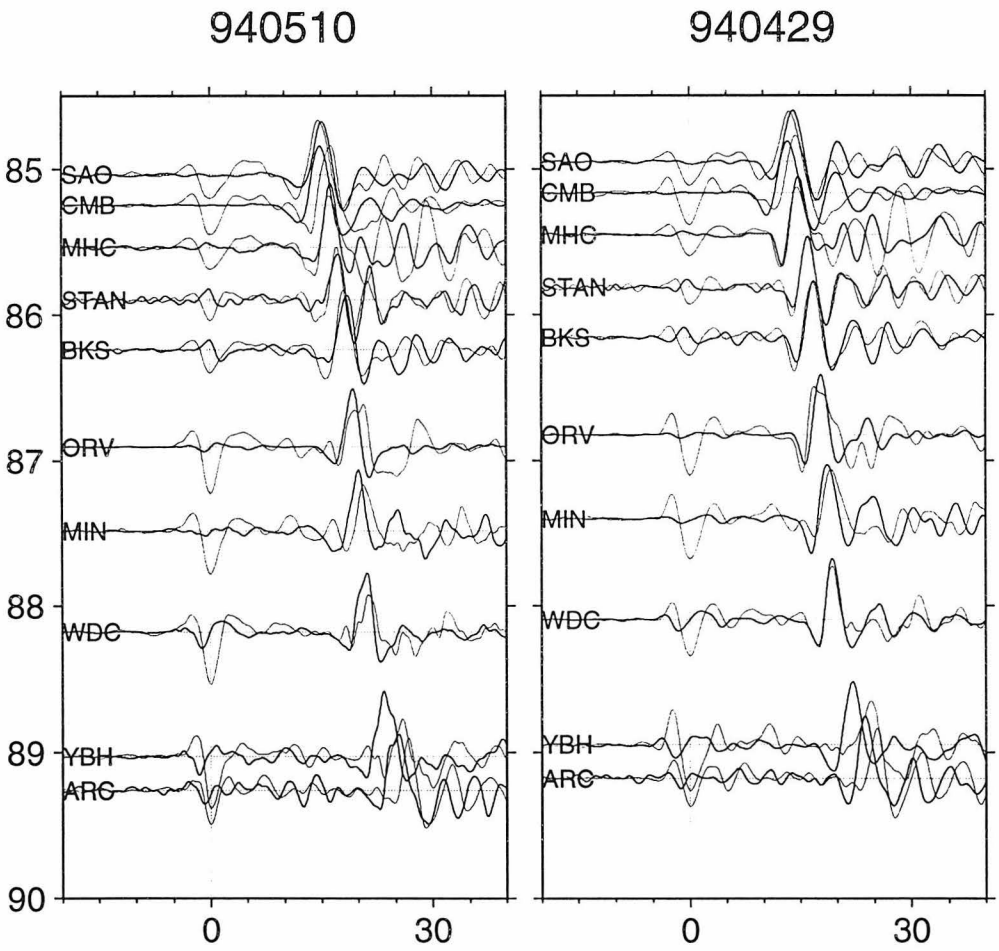

Figure 2.14: Overlay of radial and tangential components for the 5/10/94 event (left) and the 4/29/94 event (right). No significant SV/SH splitting is observed on most of the stations.

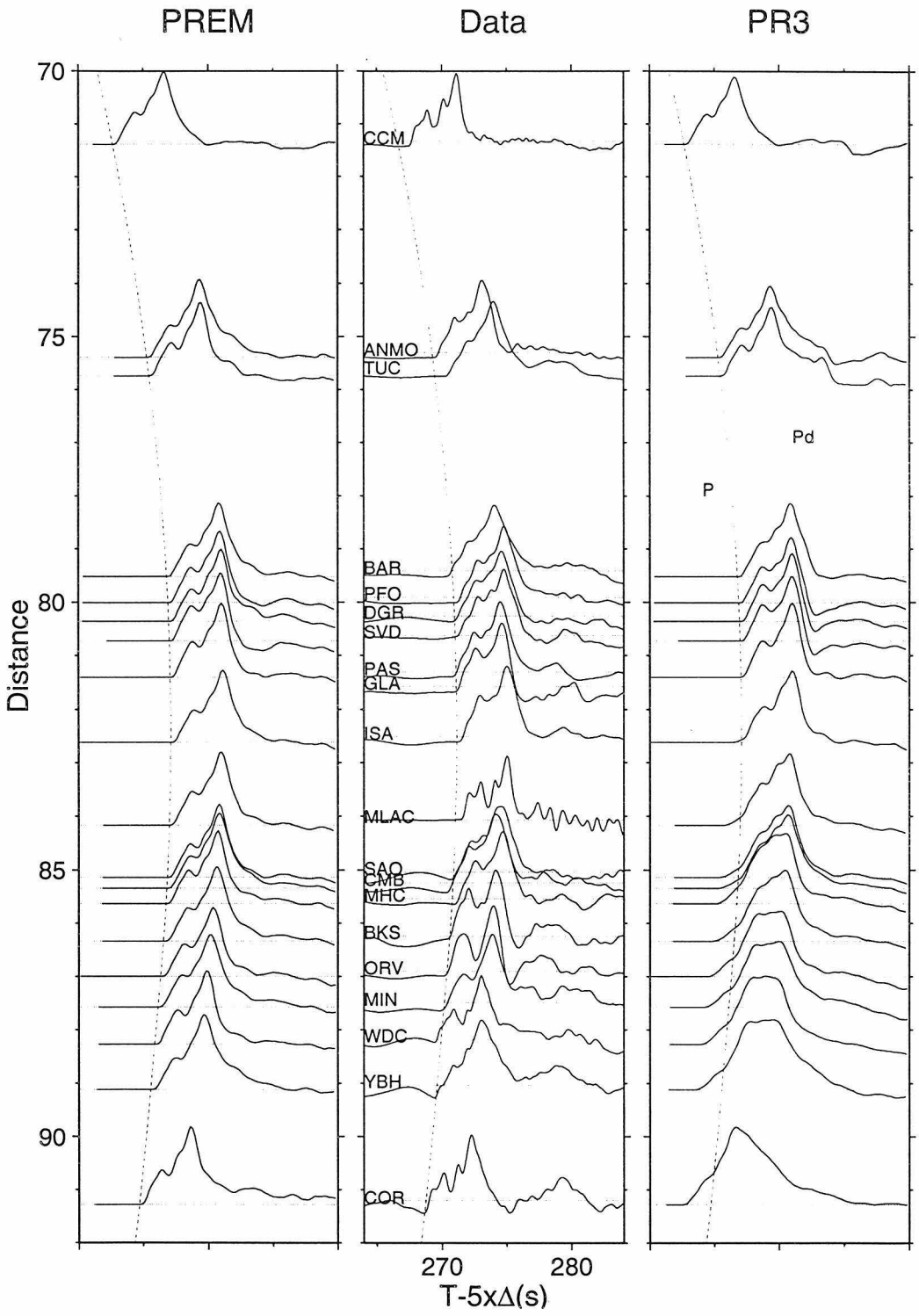

Figure 2.15: Comparison between P synthetics produced from the model PR3, PREM with P wave data as observed on the vertical component. Dashed lines indicate the P arrival predicted by PREM. At right panel, Pcd appears as a coda after P at 75° and starting at 82°, Pcd becomes the first arrival.

be identified. However, if the jump is less than 1%, we probably could not resolve it because of the complexity of the P waveform from this event.

A simpler event (8/19/94, depth=580km) was found near our primary Argentine event that has strong P-waves but weak S-waves (Figure 2.1). Displacement records from this event along with a simulated WWSSN short period profile are displayed in Figure 2.16 along with PR3 synthetics. The records are aligned along the first arrival peak predicted by the model PR3 to make the comparison to synthetics easier. The dotted lines are Pcd, P and PcP derived from model PR3. The first 3 seconds of the NEE record were used as an effective source in generating the synthetic section which displays a clear triplication. No sign of these features appears in the data in the frequency band of the WWSSN short period instrument or in the displacement record sections.

Mori and Helmberger [1995] stacked data from the dense short period California network for this source-receiver geometry and found little evidence for a Pcd phase. Thus, our broadband results substantiate their short-period conclusion, namely this region is well modeled by PREM. A lack of evidence for the Pcd phases for the neighboring region to the east was recently suggested by *Kendall and Nangini* [1996].

2.6 Discussion

We now review current ideas on the interpretation of the D″ triplication data. End members proposed ranges from a global phase-change to occurance of localized scatterers. *Nataf and Houard* [1993] advocate the first option. They interpret the apparent fluctuations in Scd and Pcd strengths as caused by lateral variations as is typically observed in upper mantle triplication data. Note that while long-period triplication data from the 400 km and 600 km transitions are nearly global [*Grand*, 1994], short-period manifestations are less convincing and show a great deal of variation. *Weber* [1993] supports the scatter interpretation and explains the types of variation in D″ that can model the P-wave data in terms of local dipping structures (up to 6°), and reflections of various dimensions. *Weber* [1994] suggests that perhaps some laminar-

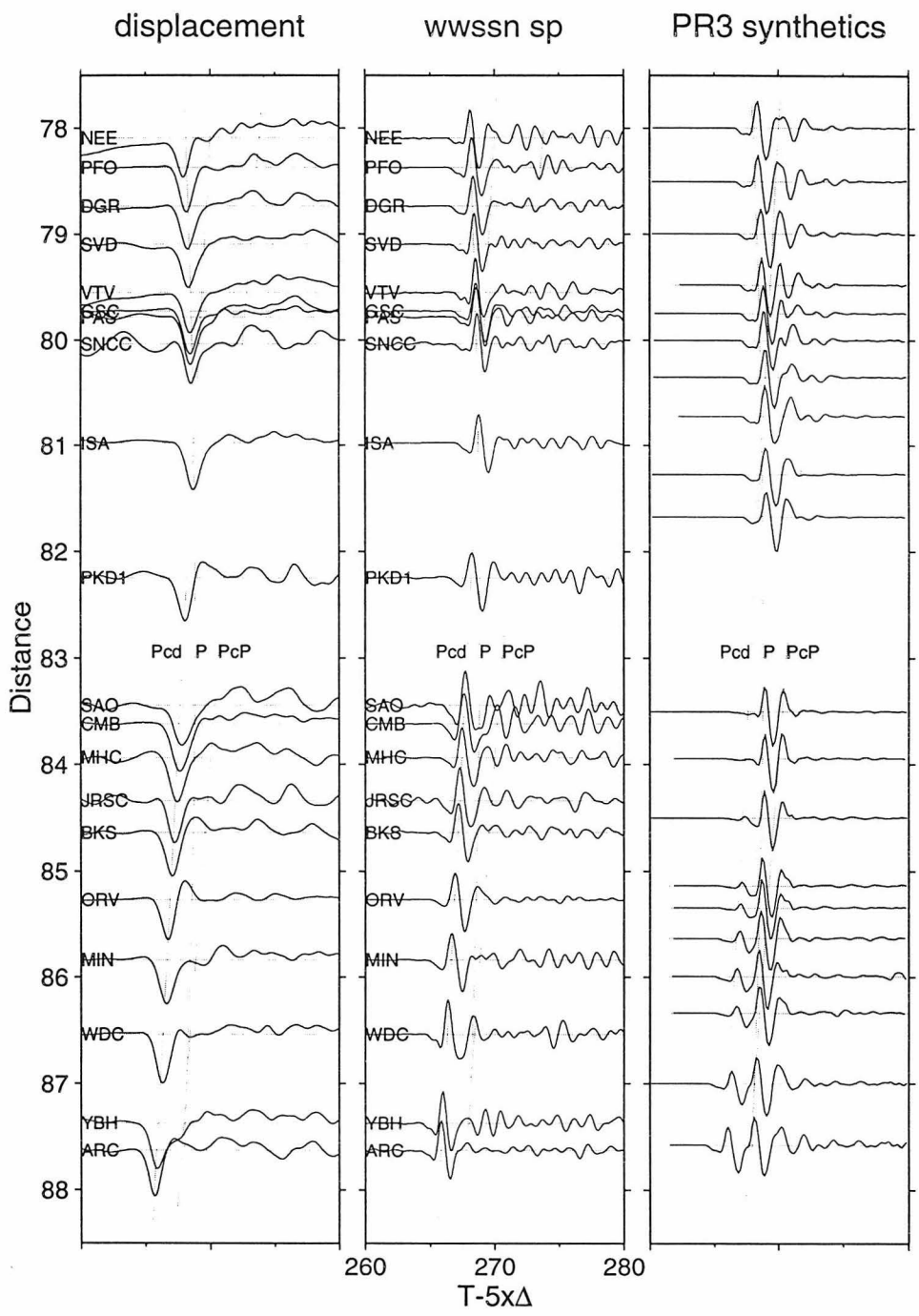

Figure 2.16: Record sections in displacement (left) and WWSSN short period response (middle) along with the synthetics in WWSSN short period (right) from the 8/19/94 event, which has a simpler source function than the 5/10/94 event. The dashed lines are travel times for P, PcP and Pcd from the model PR3. The data (left and middle panel) are lined up on the first arrival predicted by the PR3 model. The observed data show no indication of a Pcd arrival in displacement or WWSSN short period response.

type structures are responsible for these triplications and that they are influenced by lower mantle convection.

Recent global imaging studies such as *Kendall and Shearer* [1994] and *Li and Romanowicz* [1996] confirmed the circum-Pacific ring of high-velocities as mentioned earlier in Figure 2.1. Such high velocities are particularly well established beneath Asia from the detailed D″ modeling studies by *Gaherty and Lay* [1992]. The relatively fast D″ ring around the Pacific is often interpreted as being produced by subduction. The existence of the intermediate depth high velocity anomaly beneath the Caribbean has been recognized since *Jordan and Lynn* [1974]. Subsequent studies by *Lay* [1983], *Bokelmann and Silver* [1993], and and *Vidale and Garcia-Gonzalez* [1988] have established the feature in both P and S travel times and in waveform complexity. Probably the best direct evidence for a high-velocity slab-like feature in the mid and lower mantle is due to *Grand* [1994] (Figure 2.1). His results display a nearly continuous vertical zone of high velocities beneath the eastern edge of North America which he interprets as ancient slab material. *Richards and Engebretson* [1992] and *Engebretson et al.* [1992] suggest that this location is appropriate for (30–120Ma) subducted material. However, high velocity zones at the base of the mantle as far west as displayed in Figure 2.1 is more problematic as discussed by *Grand* [1994] but may be explained by bilateral slab spreading near the CMB as indicated in some recent dynamic models, *Zhong and Gurnis* [1997]. Thus, one possible explanation for the Lay-type D″ discontinuity is that this layer is subducted material spreading out at the base of the mantle, and consequently, can be viewed as something quite localized and probably rapidly varying. If this is the situation, the style of recent D″ structures such as our SDH model with a negative gradient may not be necessary in that the primary reason for adding this feature was to make the long range S diffraction synthetics look PREM-like, [*Young and Lay*, 1990]. But if the high velocity layer has variable thickness [*Kendall and Nangini*, 1996] and perhaps, disappears, there is no longer any need to add the negative gradient, which is not required in most Scd modeling *Kendall and Nangini* [1996]. We demonstrate the simplicity of diffracted S as the discontinuity disappears by introducing the 2D model displayed in Figure 2.17

with associated synthetics in Figure 2.18.

Figure 2.17 displays a lower mantle cross-section, roughly, running from Argentina to the BDSN station WDC. The lower slice contains this model along with a smoothed set of iso-velocity lines. Generalized rays can be tracked through such structures and synthetics constructed as in Figure 2.18, see *Helmberger et al.* [1997]. The synthetics before the crossover, about 82° in this run, look quite similar to those discussed earlier in Figure 2.7 and Figure 2.9. However, they become much simpler at the larger ranges. Note that the SH-synthetics in Figure 2.7 for the uniform layer model SZL show a double arrival near 95° which is eliminated in the 2D synthetics. Similarly, the SV-synthetics become simple at large ranges, looking much more PREM-like as can be seen by comparing those results with those in Figure 2.12. Thus, the task of producing single-pulse S waveforms beyond 90° and also a clear Scd at the close distances can be accomplished with such 2D structure. However, the modeling of the waveforms at the larger ranges such as COR and EDM in Figure 2.9 remains difficult. Much more broadband data in this range and beyond will be required which will be pursued in future efforts. But if the high velocity zones sampled by the sparse detections of Scd are subducted slabs as interpreted by *Grand* [1994], we would expect these high velocity regions at the base of the mantle to have abrupt lateral features which should be seen in waveform patterns as suggested in the recent study by *Kendall and Nangini* [1996].

2.7 Conclusion

This study differs from previous D″ discontinuity study efforts in that we utilize broadband data from a densely sampled extended array to study the P, SV and SH velocity characteristics. The D″ region sampled is beneath the Western Caribbean which was studied earlier by *Zhang and Lay* [1984] using the SH components of a sparse broadband analog array. Their model has a uniform high velocity layer, 260km thick with a 3% velocity jump, and predicts synthetics matching the data quite well. Our preferred 1-D model has adopted the faster PREM velocities above D″, has a

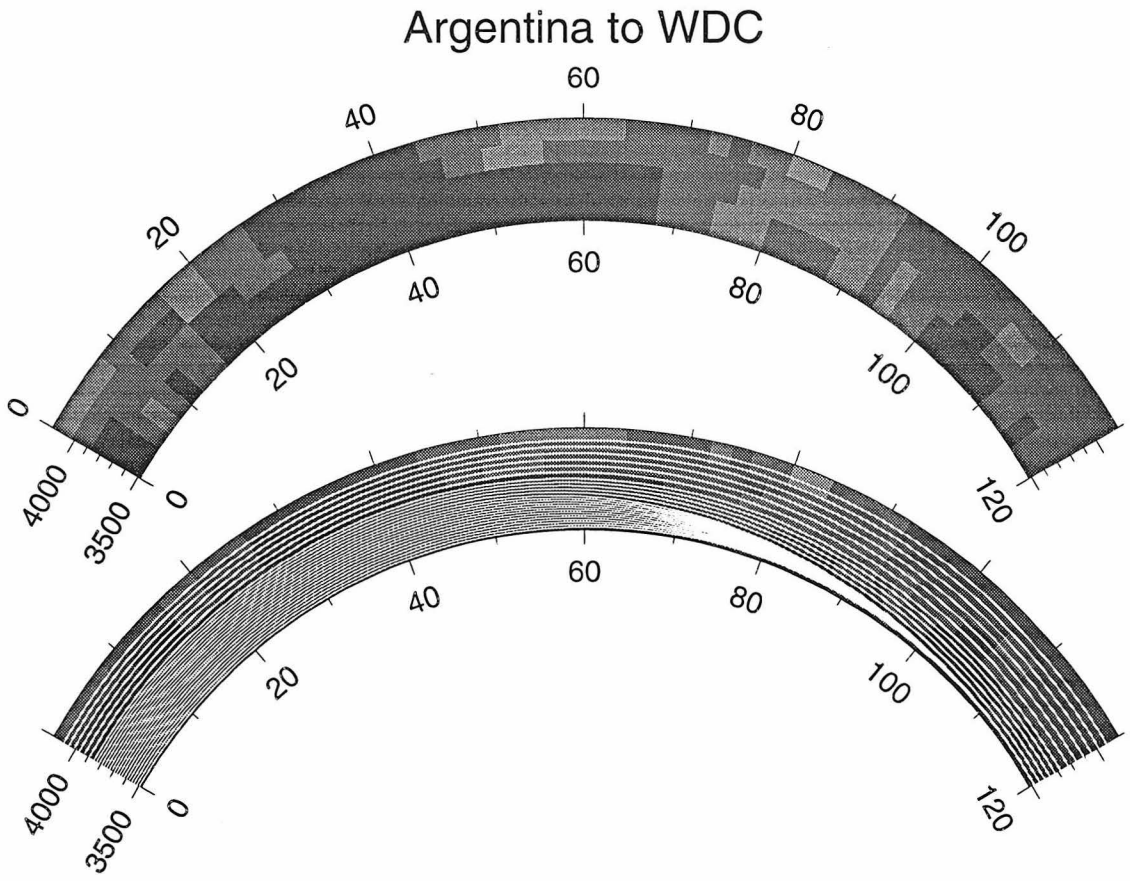

Figure 2.17: The upper panel shows a display of tomographic velocity structure by *Grand* [1994] along a slice from Argentina to California. The fast structure (Caribbean anomaly) becomes less well developed beyond 70°. The lower panel contains this structure along with iso-velocity lines used in the construction of 2D synthetics.

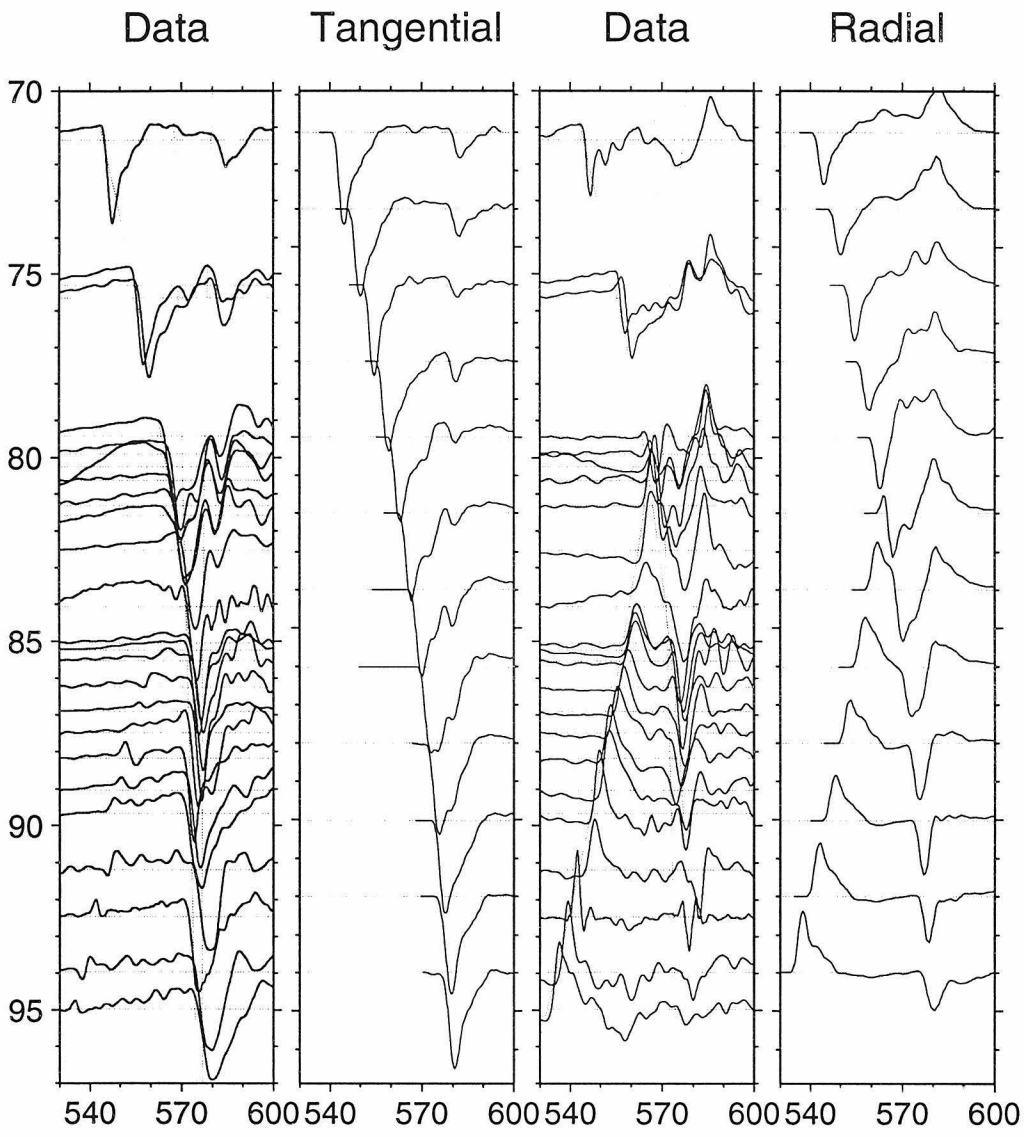

Figure 2.18: Record sections of data and 2D synthetics. Dashed lines are included from previous figures indicating the arrivals relative to SDH. Note that the 2D model can produce Scd at close distances as the model SDH and SZL and can produce simple SV arrival at distances beyond 90° as well.

3% velocity jump followed by a negative gradient similar to models developed for the Caribbean by *Kendall and Nangini* [1996]. It is more difficult to observe the D″ triplication in S_V than it is for S_H due to the interference of SKS and S-to-P converted phase caused by crustal structure. Nevertheless, we were able to identify the Scd (SV) on many records, particularly at the SKS-to-S crossover where these two phases cancel each other allowing a clear window. Some evidence for ScS splitting was observed similar to the earlier study by *Mitchell and Helmberger* [1973] which can be explained by a thin high velocity layer or 3% anisotropy confined in this study to the bottom most 100km. Detailed studies of the P-waves reveal no apparent triplication in P even though the raypaths are nearly identical to where the S-waves sample.

While the main feature of the data could be explained by 1-D models, considerable evidence for lateral variation is apparent. This is seen in the observed waveform shapes of SH and SV beyond 88° where a great deal of scatter exists reflecting the complex 3D structure suggested by *Grand* [1994]. His model has D″ fast velocities dissipating rather rapidly beneath the northern end of our data profile, and becoming more PREM-like. Synthetics generated from simplified 2D cross-sections of his structure display some features compatible to the data. However, our limited observations are too sparse to draw any definitive conclusions at this stage except to emphasize the need for more complexity in models.

Chapter 3 D″ Seismic Structure in Down-welling Regions

3.1 Abstract

Recent broadband (BB) lower mantle study has emphasized the variability of D″. In particular, the early evidence for a shear-wave triplication caused by a 3% jump in velocity a few hundred km above the CMB beneath the Caribbean has been well established although with considerable variation in depth. An equivalent P-wave triplication sampling the same region appears undetectable but occasionally observed elsewhere. If the structure producing this triplication is constructed from ancient subducted slab, we would expect an upper and a lower thermal boundary layer. Using estimates of temperature variations obtained from dynamic models, we construct plausible velocity-depth profiles. A gentle positive gradient initiated 350 km above the CMB with a sharper increase near 200 km reaching velocities of 13.8 km/sec in P and 7.4 km/sec in S. A strong negative gradient begins about 100 km above the CMB, similar to previous studies representing the lower boundary layer. This model explains the BB waveforms of P and S waves observed at TERRAscope for paths sampling beneath the Caribbean and is compatible with recent tomographic models.

3.2 Introduction

Large scale structures in the lower mantle have been well established in recent years, *Masters et al.* [1996], *Li and Romanowicz* [1996], and others. While the details may differ, most of the long period inversions yield the picture of a complex pattern of slow velocities beneath the Pacific with relatively fast regions around the circum-Pacific belt. Resolution estimates from these studies are about 500 km in vertical sampling

and a few thousand km horizontally.

Higher resolution can be obtained by using bodywave tomography using the multiples of S up to SSSSS including upper mantle triplication data and the families of core phases, ScS, SKS, etc. Beneath the Americas, there are enough stations and earthquakes to image structure with dimensions as small as a few hundred km. One of the most important results of this study are images of relatively narrow linear high velocity features seen in the lower mantle extending from mid-South America to Alaska, *Grand* [1994]. Results from a detailed P-wave tomography study by *van der Hilst et al.* [1997] are nearly identical to Grand's beneath the Americas. The agreement is remarkable considering the complete independence of data and methods employed. The American anomaly appears continuous from the upper mantle to the CMB as displayed in Figure 3.1a. *Grand* [1994] interprets the high velocity of D″ regions displayed in this figure as ancient ponded slab.

Linear high shear velocity structures which extend down to the CMB and spread out over the CMB are quite similar in form to down-welling slabs displayed in simple convection models with plates and whole mantle convection. An east-west cross-section through the seismic velocity and beneath the Americas is compared with a convection model with oceanic lithosphere subducting and descending through the entire lower mantle (Figure 3.1b). As with the observed tectonics, the convection model has oceanic lithosphere subducting beneath a continent which moves toward the ocean (east in Figure 3.1a and left in Figure 3.1b). Although the tomography model has higher frequency variations, the tomography and convection models are quite similar (Figure 3.1). The similarities of the seismically fast anomalies spreading out on top of the CMB which are connected to slabs (Figure 3.1a), suggest that these old cold slabs may be responsible for the jump in shear velocity 200 km above the CMB. For illustration, we show a radial profile through the slab (A-A′ in Figure 3.1b). The convection model, taken from *Zhong and Gurnis* [1997], was computed in a two dimensional cylindrical geometry with temperature-dependent viscosity. The calculation is transient and the slab descends through an incompressible and isothermal fluid (initially) with a hot thermal boundary layer at the base. The snap-shot in the

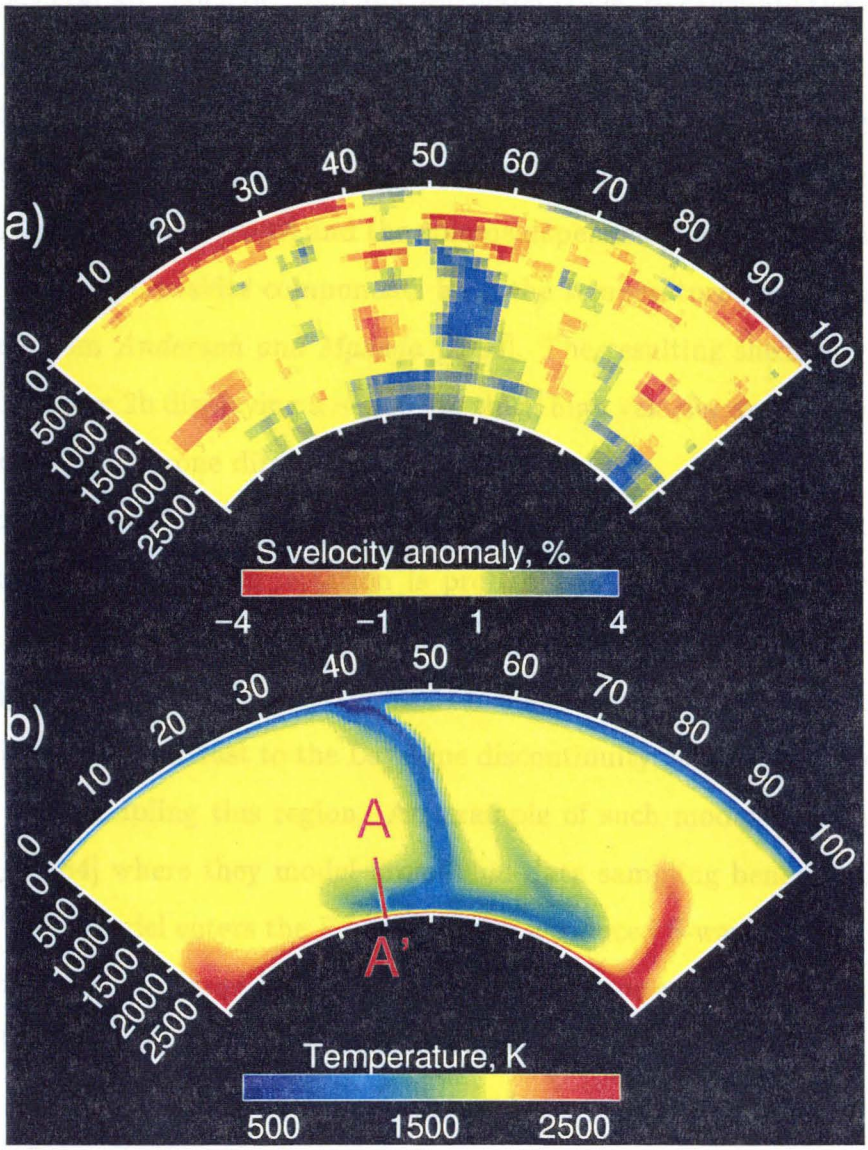

Figure 3.1: a) A cut through a great circle (20°– -140°) to (11.7°– -35.8°) for the tomography model by *Grand* [1994] (the scale varies with depth as in the original paper). b) Temperature field for a convection model computed by *Zhong and Gurnis* [1997].

convection model (Figure 3.1b) represents 230 Myr of subduction.

In order to transform the thermal structure into a shear wave velocity model, thermal perturbations are applied to the adiabatic profiles of elastic parameters. We use the general approach of *Zhao and Anderson* [1994] to calculate the bulk modulus, rigidity, and density along an adiabat. We use different parameters for the (Mg,Fe)O magnesiowustite and (Mg,Fe)SiO_3 perovskite components of the lower mantle. For magnesiowustite, the temperature dependence of the coefficient of thermal expansion comes from *Isaak et al.* [1989] and the volume dependence from *Chopelas and Boehler* [1992]. For the perovskite components both the temperature and volume dependencies come from *Anderson and Masuda* [1994]. The resulting shear velocity profile is shown in Figure 2b displaying a $\sim$ 300 km thick high velocity anomaly which overlays a thin low velocity zone directly above the CMB.

A comparison of the tomography results (Figure 3.1a) with this model is interesting but a detailed interpretation is probably premature. However, if the basic premise is correct, we would expect the temperature and velocity profiles to be similar to Figure 3.2, where the velocity tends to start increasing as we approach D″. This feature is in stark contrast to the Lay-type discontinuity usually assumed in modeling seismic data sampling this region. An example of such modeling is given in *Zhang and Lay* [1984] where they model broadband data sampling beneath the Caribbean region. Their model enters the D″ region with a reduced S-wave (1.5% below PREM, *Dziewonski and Anderson* [1981]) velocity and contains a 2.75% jump, 250 km above the CMB. This model produced excellent fits to the waveform data.

The dataset used by these authors has been greatly improved with the introduction of the Californian Broadband arrays, *Ding and Helmberger* [1997]. Their results suggest a model similar to those proposed by *Young and Lay* [1987] with a strong S-velocity jump (3%), 200 kms above the CMB with a strong negative gradient approaching the core unlike that displayed in Figure 3.2b. No evidence in the P-waveforms for an equivalent triplication was found. They also found substantial evidences for lateral variation across their seismic profile indicating the complexity in D″. Similar results for D″ samples further to the east have been reported by *Kendall*

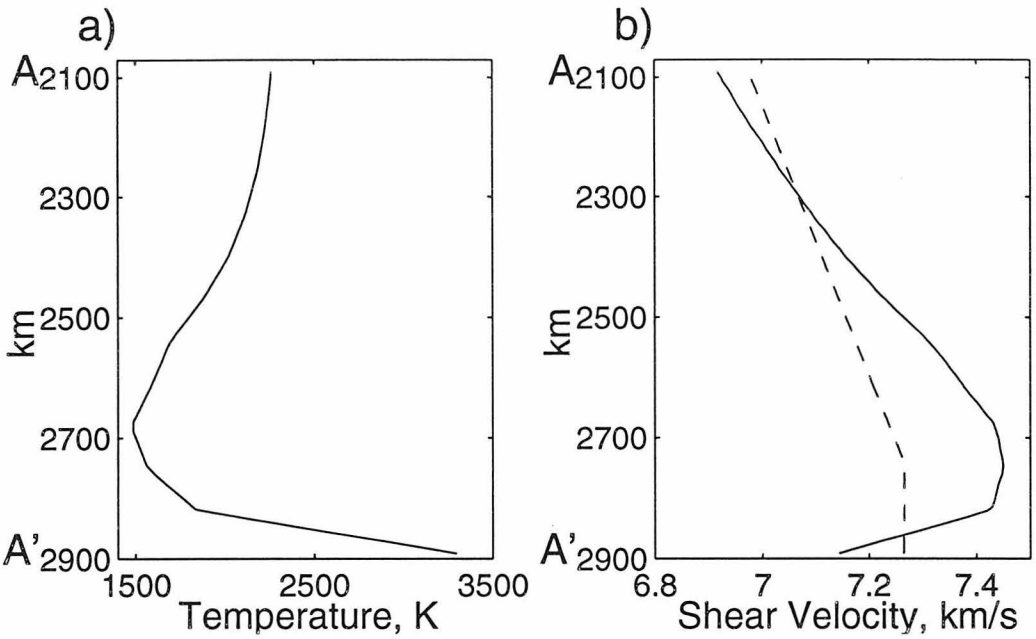

Figure 3.2: Temperature (a) and the corresponding shear velocity (b) for the cross-section A - A' marked in Figure 3.1b. PREM model values (dashed line) are included for reference.

and Nangini [1996].

The purpose of this paper is to introduce complex seismic models similar to those suggested in Figure 3.2 and explain the present seemingly incompatibility of P and S seismic profiles. The latter topic has a long history, as discussed in detail by *Weber* [1993].

3.3 Modeling results

The dataset used in this report is a subset of the one that is discussed in detail by *Ding and Helmberger* [1997]. It consists of a collection of South American events recorded by TERRAscope (Caltech) and BDSN (UCB). The geometric paths for S and SKS to TERRAscope plotted on a tomographic cross-section [*Grand*, 1994] is given in Figure 3.3. The section crosses the Caribbean anomaly along the western edge as displayed in Figure 3.1. The paths of interest, namely Scd and ScS, are bracketed by these two rays. Thus, all of these rays sample similar upper mantle paths which enhances resolution in the lowest most mantle. The S-wave path is nearly PREM

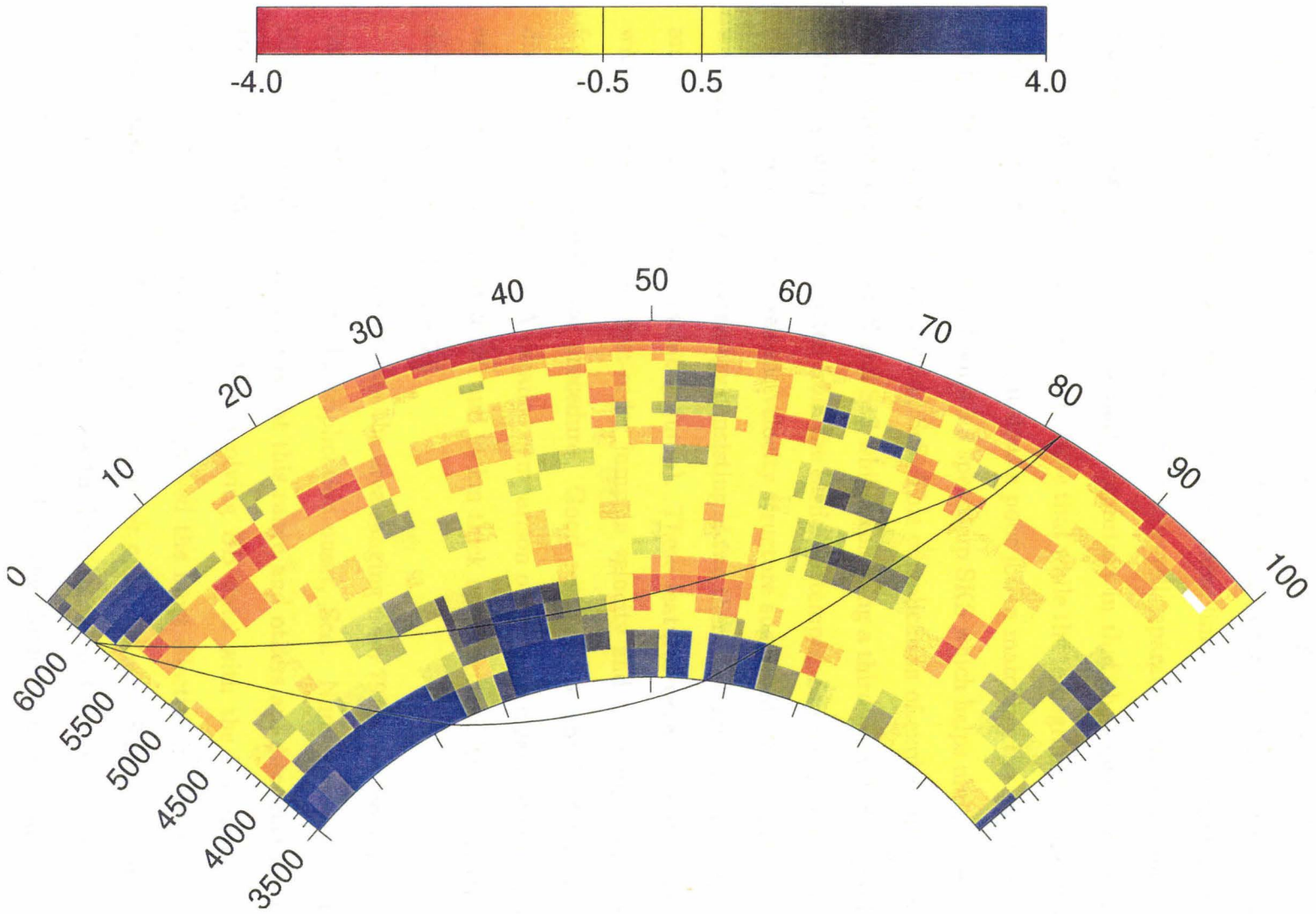

Figure 3.3: The cross section of tomographic model by *Grand* [1994] along the great circle defined by a deep south American event (5/10/94) and TERRAscope stations. The color scale varies with depth (4% at the top to 1% at the bottom). Raypaths of S and SKS at the cross-over distance are also displayed.

except for the slow receiver segment. This feature maps into a delayed S-arrival as displayed in Figure 3.4.

These synthetics are appropriate for a 1D reference model (PREM) and Grand's 2D model after correcting for 2D effects on the path, Appendix A. These two models show a difference in SKS-S crossover of about .2° which is close to that observed as indicated by the crossing lines in the figure. These lines are easily established by using the complete data set when S and SKS are well separated. However, modeling the ranges in this figure are particularly important in that the separation between ScS and S provides a major constraint. Note that while the tomography model predicts an earlier cross-over than PREM, it does a poor job in matching the waveforms. Essentially, the fast D″ layer in Figure 3.3 speeds up SKS which helps match the cross-over but causes difficulty in matching ScS. This complication of explaining the relatively large separation between S and ScS while explaining a third arrival, Scd, produced by a velocity jump has persisted from the earliest attempts, *Lay and Helmberger* [1983a].

To mimic the radial seismic velocity structure suggested by dynamic predictions, we adopted a modeling strategy consisting of two thermal-boundary layers (gradients) and a phase transition (velocity jump). These features were allowed to vary along with the position of the first-order jump in velocity and the model space explored following a trial-and-error procedure. Good results were obtained for the models displayed in Figure 3.5. A detailed comparison of synthetics generated from the two extreme models, namely a 120 and 60 km thick upper zone, with the SH triplication data is displayed in Figure 3.6.

This seismic section sampling the area ranging from 79° to 83° contains the most definitive observations on the triplication onset, Scd. Numerous presentations of BB data filtered in various ways at this range and others are discussed in *Ding and Helmberger* [1997], but simply convolving BB data with the instrument response discussed in *Zhang and Lay* [1984] proved the most effective in allowing Scd to be separated from the tail of S so that its move out relative to S and ScS can easily be seen. By overlaying these synthetics with the data, we find that the thicker transition zone (120 km) provide a more favorable fit. The thinner zone separates S and ScS

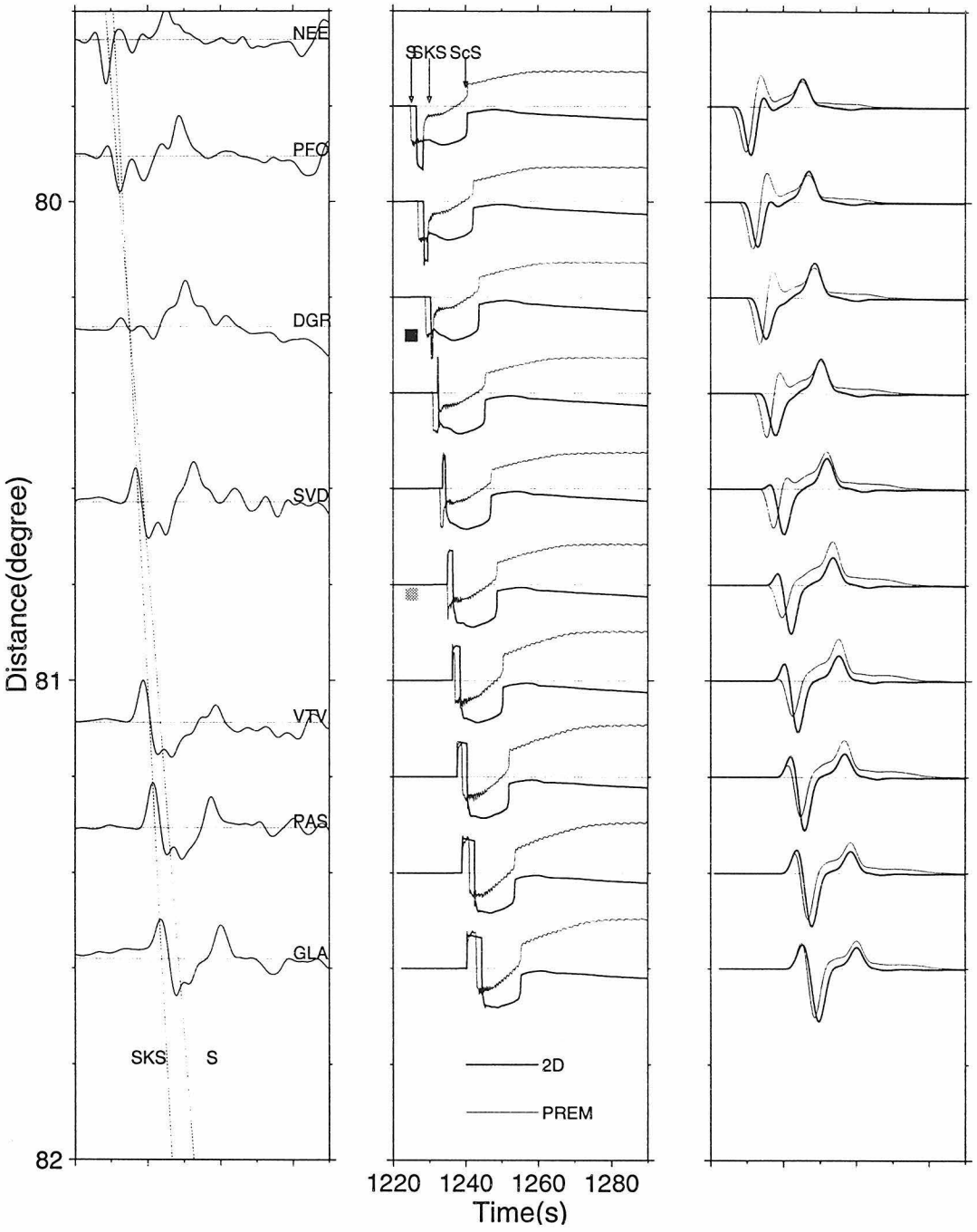

Figure 3.4: Comparison of the data and synthetics at the distance range of SKS-S cross-over. Left panel displays data from the 5/10/94 south American event. The middle panel displays the step responses for PREM (light line) and for the 2D model displayed in Figure 3.3 (heavy lines). The solid and gray squares mark the cross-over distance from these two models. The right panel displays the synthetics generated from the step responses in the middle panel by convolving with the source function appropriate for (5/10/94) event.

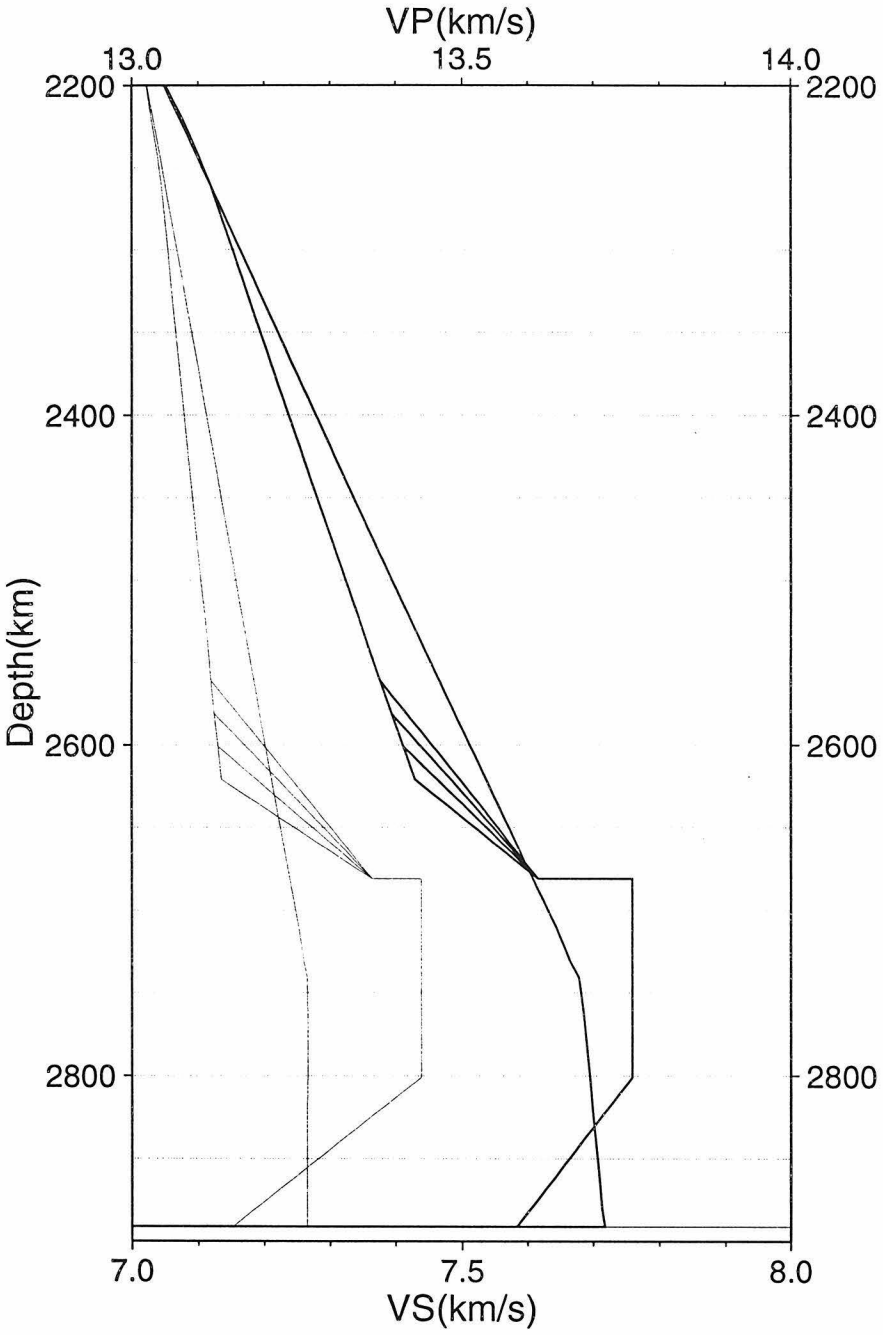

Figure 3.5: Possible CMB models relative to PREM with heavy lines for P and light lines for S. The models include a velocity jump of 1% for S and 1% for P at the depth of 2680 km, a transition zone above the jump with varying thicknesses of 60 km, 80 km, 100 km, and 120 km (3% S velocity increase and 1% for P) and a negative gradient zone at the bottom with thickness of 90 km (4% drop in S velocity and 1.3% for P velocity).

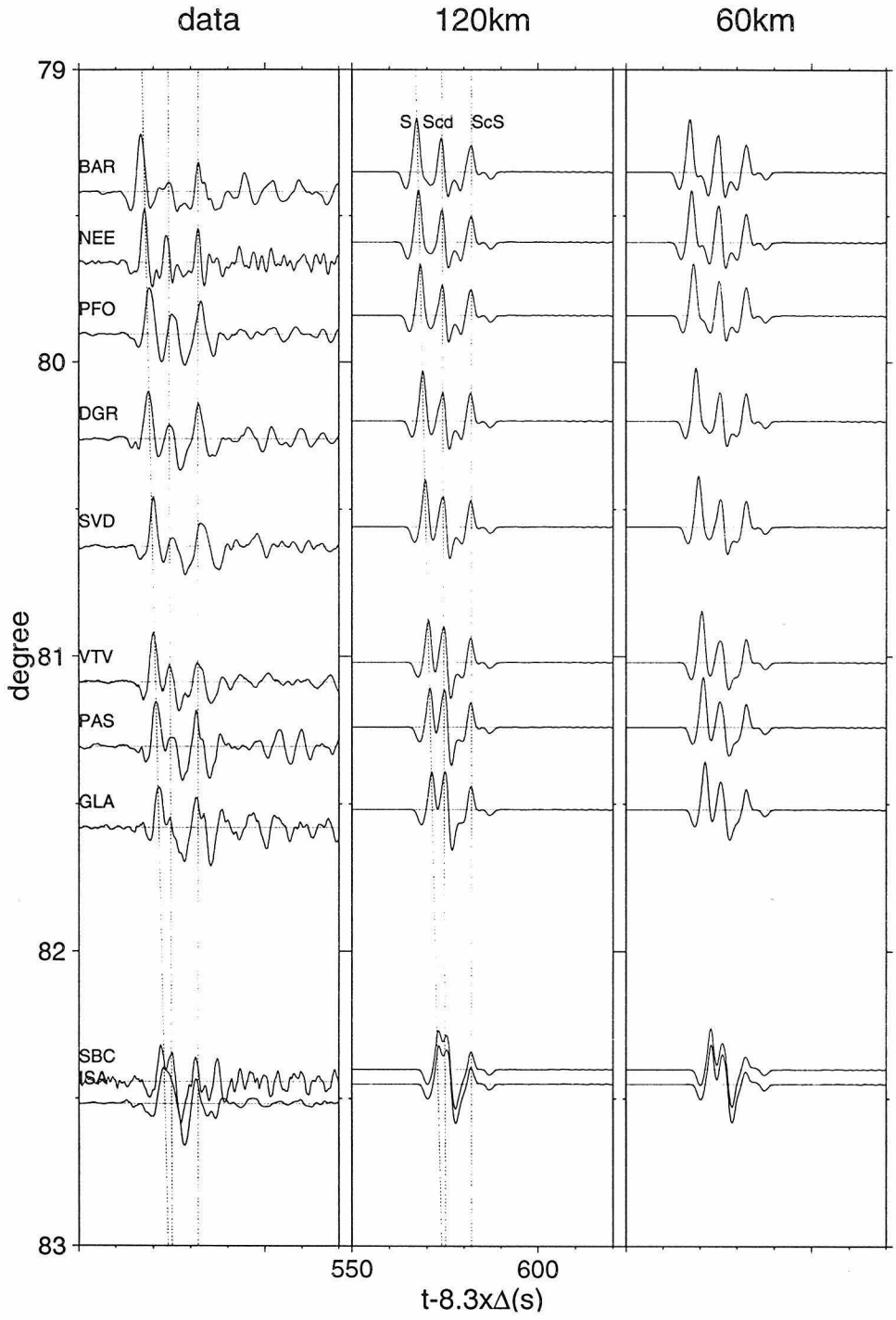

Figure 3.6: Left panel displays the TERRAscope observations from the 5/10/94 event after convolving with the broadband instrument used in *Zhang and Lay* [1984]. Middle panel displays a synthetic generated for model with the upper transition zone of thickness 120 km and the right panel for 60 km. Both models produce Scd phases. The middle panel fits the data better in S-ScS and S-Scd differential time. Dashed lines are the travel times for the model with a 120 km thick transition zone.

slightly too much.

The P-wave velocities are only estimates since we have no identified Pcd or PcP arrivals. We simply assumed the P-wave gradients in our model would be about half the S-wave strength [*Anderson and Masuda*, 1994]. The comparison of TERRAscope data, filtered by a short-period instrument as discussed in *Ding and Helmberger* [1997], against synthetics is displayed in Figure 3.7. It becomes difficult to identify such small secondary arrivals without extensive processing. *Mori and Helmberger* [1995] attempted this using the SCSN array but were not able to identify even the PcP. Comparing the synthetics from these models with observations at other ranges produces satisfactory fits, at least as good as models with sharp velocity jumps. However, at larger ranges, $\Delta > 90°$, the waveforms become more unstable apparently caused by lateral variation which easily distorts horizontally traveling rays [*Helmberger et al.*, 1997]. The tomographic results displayed in Figure 3.3 suggest this is the case.

3.4 Discussion

The seismic models proposed here contain more parameters than previous typical "Lay type" structure. Note that the earliest models explained the Scd phase with only two parameters, a velocity jump and thickness and they proved very effective for this same particular path, *Zhang and Lay* [1984]. Thus, our models are not unique but simply explains the existence of a strong Scd with a much subdued Pcd by adding an extra set of parameters. Moreover, the sharp jumps in the models displayed in Figure 3.5 are also not necessary but only indicative of a more rapid increase in velocity at that depth. With so many parameters available, it becomes relatively easy to explain the data.

Thus, we were successful in finding seismic models in accordance with subducted slabs with an overall thickness of about 300 km. If these are, indeed, slabs spreading horizontally over the CMB, we would expect to see substantial lateral variation in these structures depending on the rate of production and age. A systematic study of where Scd and Pcd are observed in conjunction with detailed tomography needs

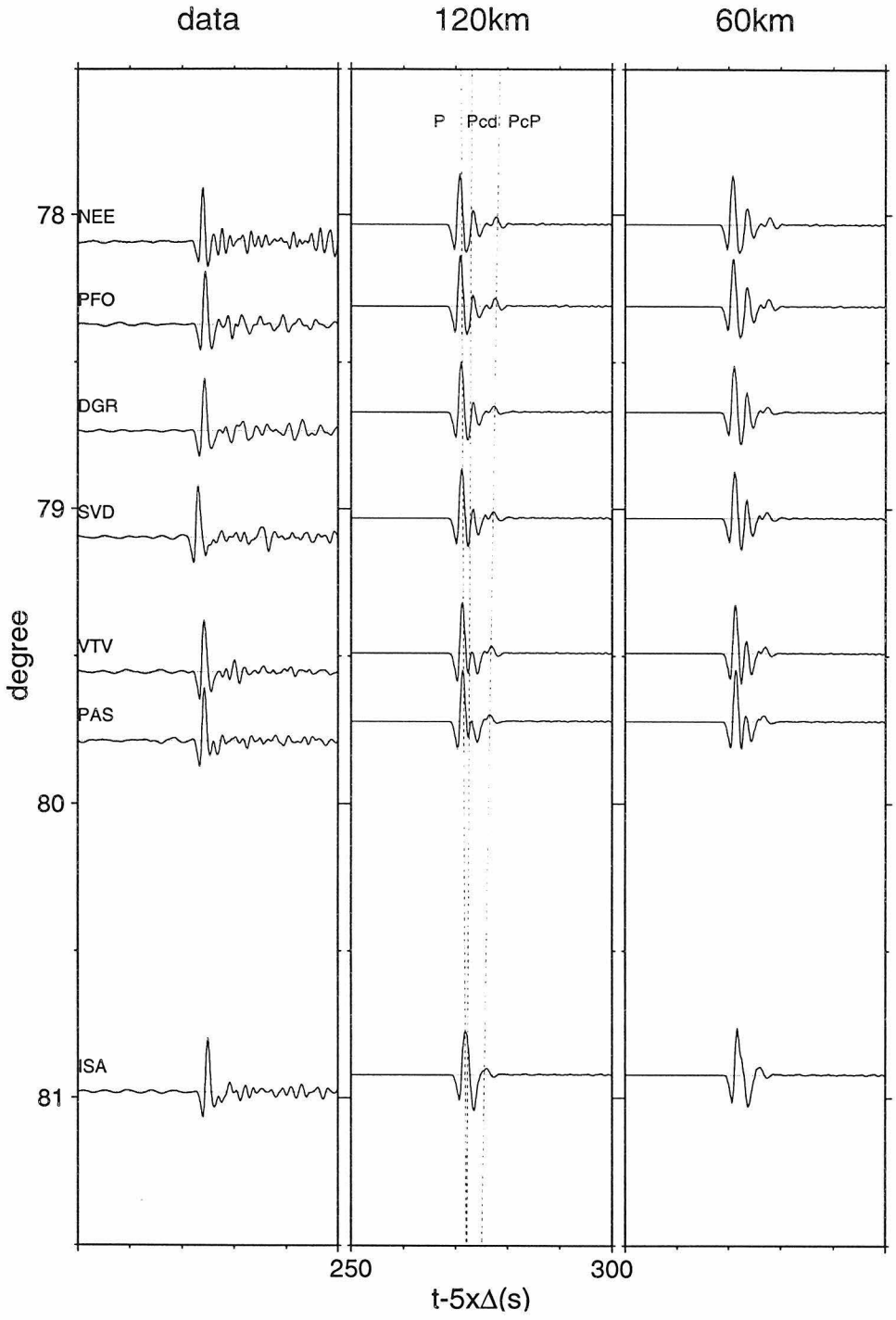

Figure 3.7: Comparison of P data (WWSSN short-period response) on the left and synthetics for the model with upper transition zone thickness 120 km (middle) and 60 km on the right transition zone. The middle panel has small Pcd and PcP arrivals at the noise level in the data, while the right panel has stronger Pcd and PcP phase.

to be addressed. Secondly, inversion studies involving dynamic modeling with realistic material properties and seismological data together appears fruitful and will be attempted in future studies.

A traditional interpretation of the "Lay-type" discontinuity atop D″ is that it represents a jump in major element chemistry and density [*Davies and Gurnis*, 1986; *Christensen*, 1996]. This model has been preferred over a thermal origin because of the expectation that the top of a cold thermal boundary layer would be diffusive and incapable of causing a triplication in SH. However, there is a major dilemma posed by this hypothesis: if D″ was made up of a chemically dense layer, then this layer would be pushed away from convective down-wellings [*Gurnis*, 1986; *Christensen*, 1996] – unfortunately, the triplication is best displayed beneath Circum-Pacific subduction zones [*Lay*, 1995]. With the recognition of penetration of slabs completely through the lower mantle [*Grand et al.*, 1997; *van der Hilst et al.*, 1997], the chemical origin of the Lay discontinuity becomes problematical. We show here that it is possible for old, cold subducted slabs laying flat atop the CMB, as strongly indicated by seismic tomography, to give rise to strong triplications in SH. This is demonstrated by our simple models of D″ with a 120 km thick diffuse top boundary, very similar to the results of our convection models. The lateral variation in the topmost boundary of D″ may well map out the geographical distribution of ancient subducted slabs introduced into the mantle over the last few hundred million years.

Chapter 4 Core-mantle Boundary Structure Beneath Africa and Europe

4.1 Introduction

The core-mantle boundary and adjacent transition zones play a critical role in Earth dynamics. Thus, lateral variation in this structure provides some fundamental information about how the mantle convects. Many papers have been published on the seismic resolution of this structure at various wavelengths(see review by *Loper and Lay* [1995]). The 3D model by *Grand* [1994] appears to have the highest resolution in terms of S-velocity, a few hundred km. Figure 4.1 displays his tomography map of the D″ structure beneath a large portion of the Earth. This model was constructed by picking the travel times of multiple S phases (SS, SSS,....) along with core phases, ScS, SKS, etc., as recorded on analog records. These data are unique and not used by any other modeling group. In contrast, most global models have been constructed by inverting long-period waveforms as recorded on the Global Digital Seismic Networks(GDSN) and thus share the same data. While these methods vary somewhat, they produce similar models near the surface but disagree significantly at depths displayed in this figure. Thus, some independent checks of Grand's model (Figure 4.1a) would help establish its validity. The structure above a depth of 2500 km agrees remarkably well with P-velocity tomography [*van der Hilst et al.*, 1997; *Grand et al.*, 1997]. The agreement is not good below this level. This may be caused by the lack of PKP data which would be included in future efforts. To check these models, one can examine some key profiles of data to see how well synthetics constructed from these models predict the observations. Figure 4.1a includes event locations (South America) and WWSSN seismic stations along with the surface projection of travel paths. Figure 4.1b displays the paths taken by the most important phases discussed

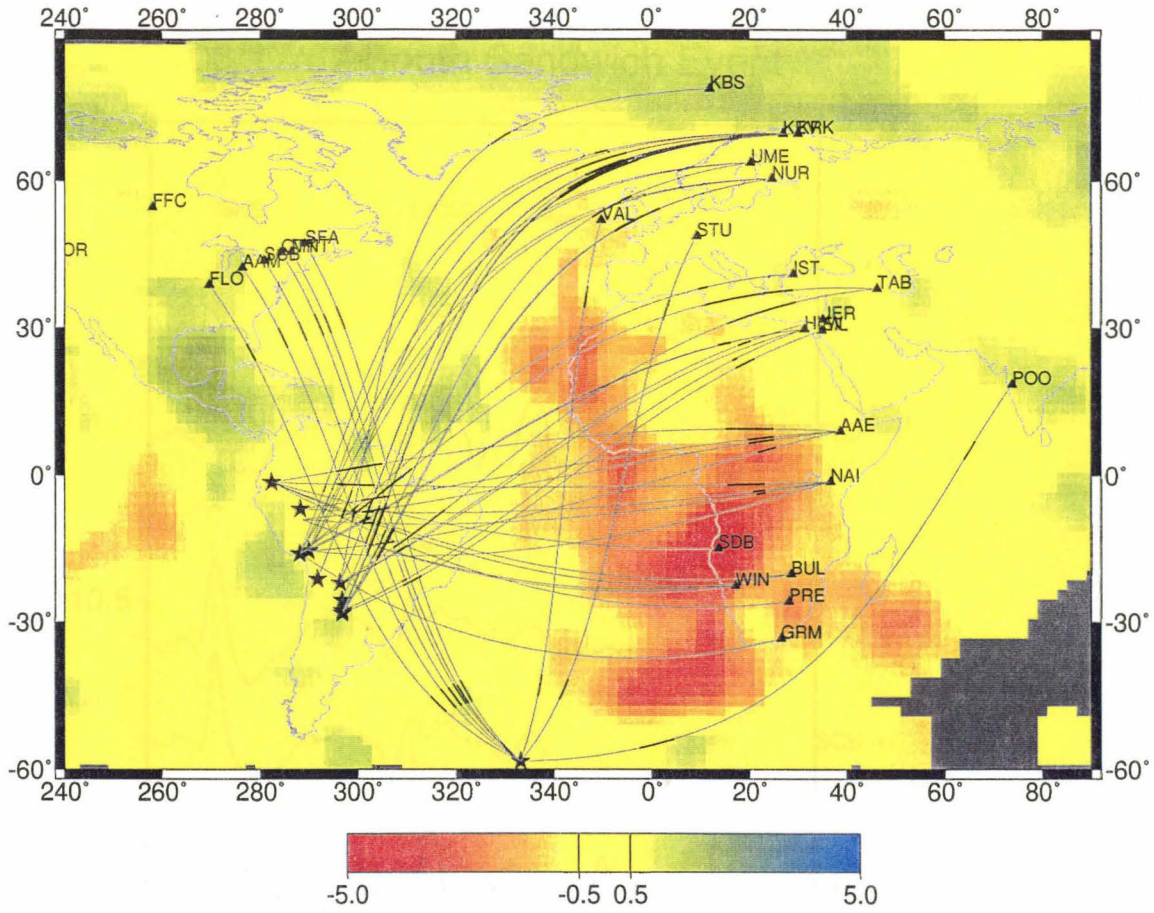

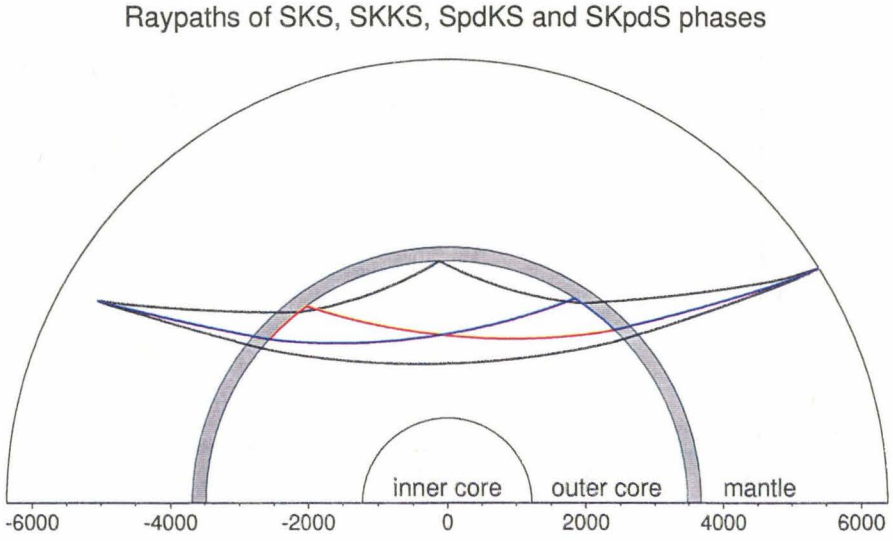

Figure 4.1: a) Distribution of the events (stars) and stations (triangles). The background is the CMB structure from the tomographic model by *Grand* [1994]. The heavy lines display where the $SK_{P_{diff}}S$ and $S_{P_{diff}}KS$ diffract along the CMB. b) The raypaths of SKS, $SK_{P_{diff}}S$ and $S_{P_{diff}}KS$ computed for PREM at 118°.

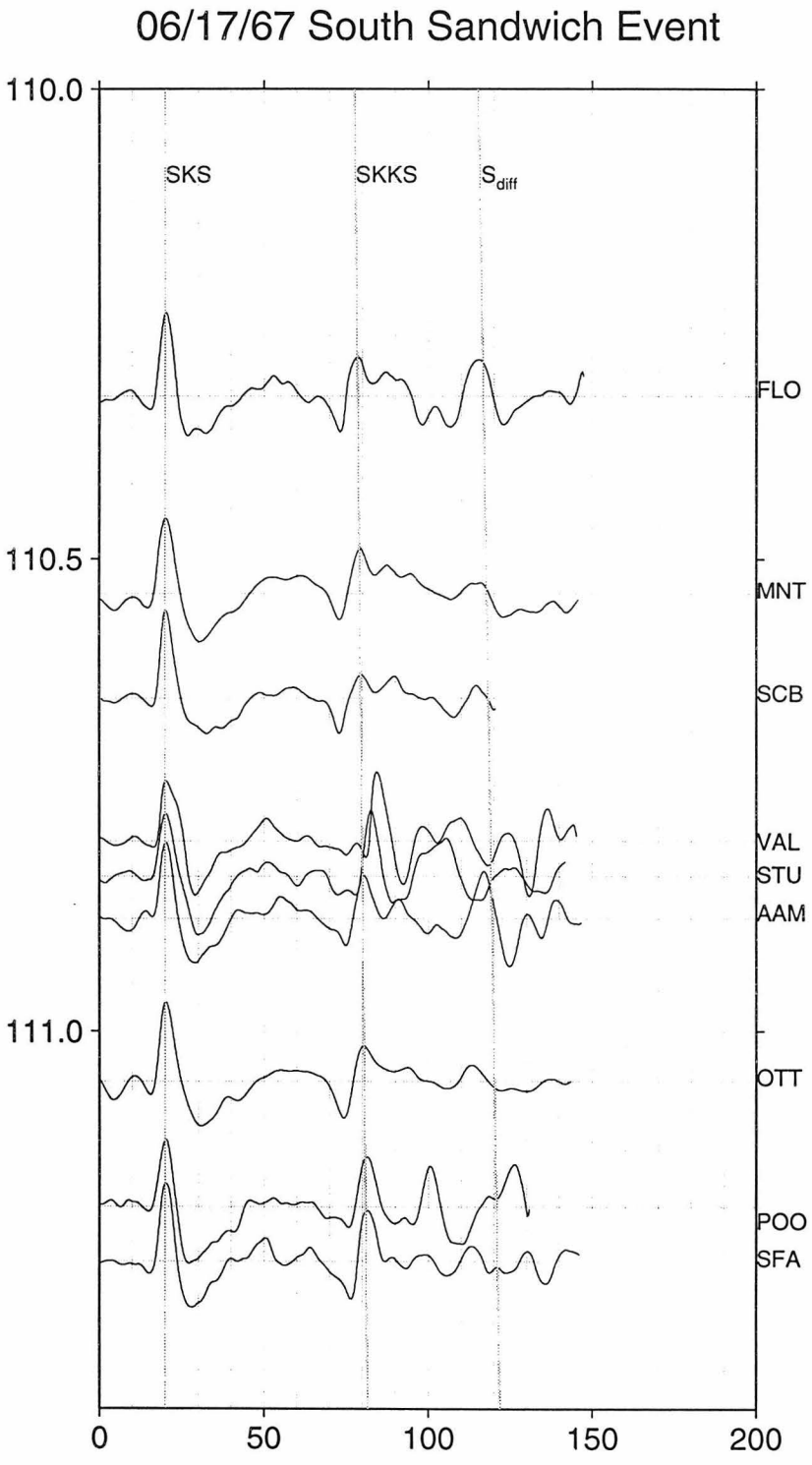

Figure 4.2: A record section from a South Sandwich event recorded on North America and European stations as an example of regions without ULVZ.

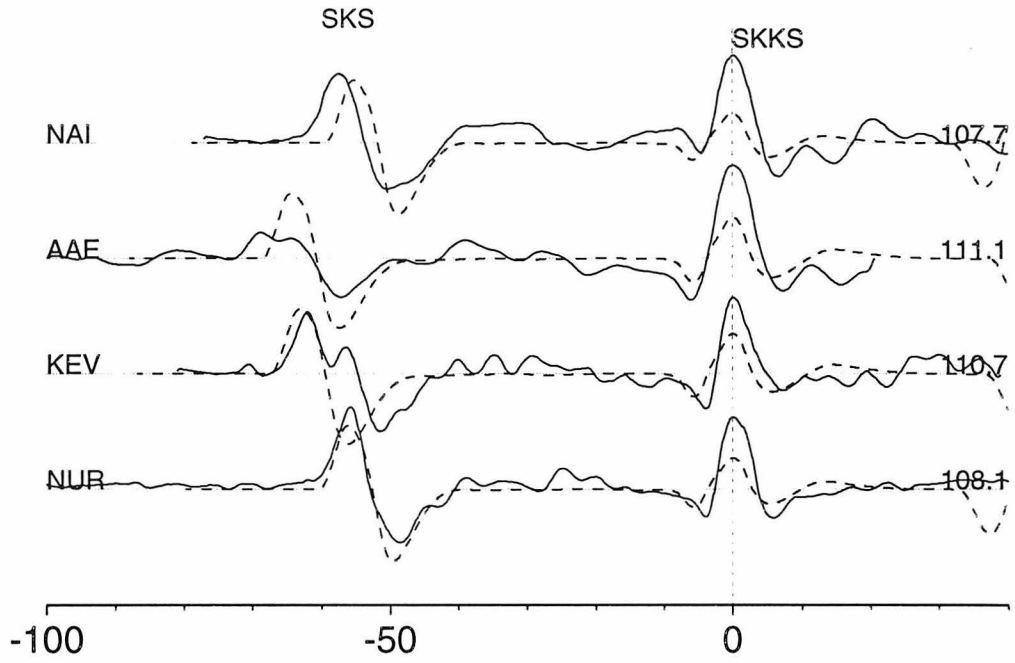

Figure 4.3: Four seismic records show different behavior in waveforms and travel times at about 110°. The dashed lines are synthetics for PREM. NAI shows only differential travel time anomaly, KEV shows only the waveform distortion in the first arrival, AAE shows both while NUR is fit well by PREM.

in this paper, namely, SKS, $SK_{P_{diff}}S$, and $S_{P_{diff}}KS$. Note that these rays share similar paths in the upper mantle and therefore differential times provide highly useful measurements of lateral variation near the CMB. Although these phases provide quality information, they require relatively deep sources to separate surface reflections from SKKS. For example, a micro-section produced from a South Sandwich event is presented in Figure 4.2. Note that considerable complexity occurs in the tail of SKKS which is probably caused by surface reflections. Thus, the source region available to study these phases is restricted mostly to the subduction zone beneath South America as indicated in Figure 4.1a.

Many of the records displayed in Figure 4.2 were also included in a paper discussing the ultra low velocity zone (ULVZ) beneath the mid-Pacific, *Garnero and*

Helmberger [1996]. The paths to the United States generally yield observations consistent with PREM-like synthetics. They are consistent with the timing separation between SKKS-SKS and in waveforms of the phases $S_{P_{diff}}KS$ and $SK_{P_{diff}}S$. These phases are rather sensitive to the velocity structure at the CMB and can be quite prominent in regions containing a ULVZ with P velocities 10% or more lower than PREM at the CMB, *Helmberger et al.* [1996]. The KEV record in Figure 4.3 displays a good example of this phase. In fact it is the record that sparked a global search for more examples, *Garnero and Helmberger* [1995]. Generally, there is a good correlation between anomalies in SKKS-SKS differential travel time residuals and the prominence of the $S_{P_{diff}}KS$ and/or $SK_{P_{diff}}S$ phase. Thus, one can simply examine records at these distances and determine if the CMB region is anomalous or not. For example, if we examine the trace at VAL in Figure 4.2, we see that SKS is broader, indicative of the prominence of $S_{P_{diff}}KS$, and SKKS is late or the SKS phase is early. However, there is an ambiguity here in that the anomaly could be at either end, $S_{P_{diff}}KS$ or $SK_{P_{diff}}S$, or both. We have relied mostly on tomographic studies to interpret which end the anomaly lies, although no significant ULVZ's in the blue ring has been found around the Pacific as reported by *Garnero and Helmberger* [1995]. We digitized and compared all the observations obtained from the south Sandwich event (Figure 4.1) and compared them with PREM synthetic. Only VAL and STU to a lesser degree show anomalous fits. These general features look quite compatible with the tomographic results presented in Figure 4.1a. Thus, we will suppose that the anomalous structures beneath Africa are responsible for the distortions at AAE and NAI (that is $SK_{P_{diff}}S$) and beneath Iceland to explain KEV. Note that these two regions are distinctly different in their S-wave velocities as indicated in these SKKS-SKS comparisons and in their tomographic footprints displayed in Figure 4.1a. This implies a very localized ULVZ beneath Iceland and a more massive structure beneath Africa. We will address the modeling of waveform data from these two regions in the remainder of this chapter.

Table 4.1: South American events list

No.	origin	lat(°)	lon(°)	depth(km)
1	650917 11:13:53.5	-1.4	-77.7	161
2	651103 1:39:3.20	-9.04	-71.32	587
3	670117 1:7:54.3	-27.4	-63.3	586
4	670215 16:11:11.5	-9.075	-71.38	595
5	670909 10:6:44.5	-27.62	-63.15	577
6	671227 8:53:51.4	-21.2	-68.3	135
7	680823 22:36:49.8	-22	-63.64	513
8	690725 6:6:42.1	-25.49	-63.21	573
9	700617 4:44:20.9	-16	-71.88	99
10	710221 10:35:19.7	-23.8	-67.19	165.6
11	710508 0:49:45.0	-42.28	-71.78	146.2
12	720112 9:59:10.3	-6.83	-71.77	575
13	731025 14:8:58.5	-21.96	-63.65	517
14	741007 21:53:8.4	-58.08	-27.26	286
15	741205 11:57:31.1	-7.65	-74.45	156
16	770204 7:46:34.1	-24.66	-63.39	555.1
17	790521 22:22:23.0	-15.44	-70.04	209
18	820915 20:22:57.8	-14.53	-70.79	153
19	821118 14:57:51.3	-1.73	-76.72	190
20	831212 12:21:12:0	-28.13	-63.15	602

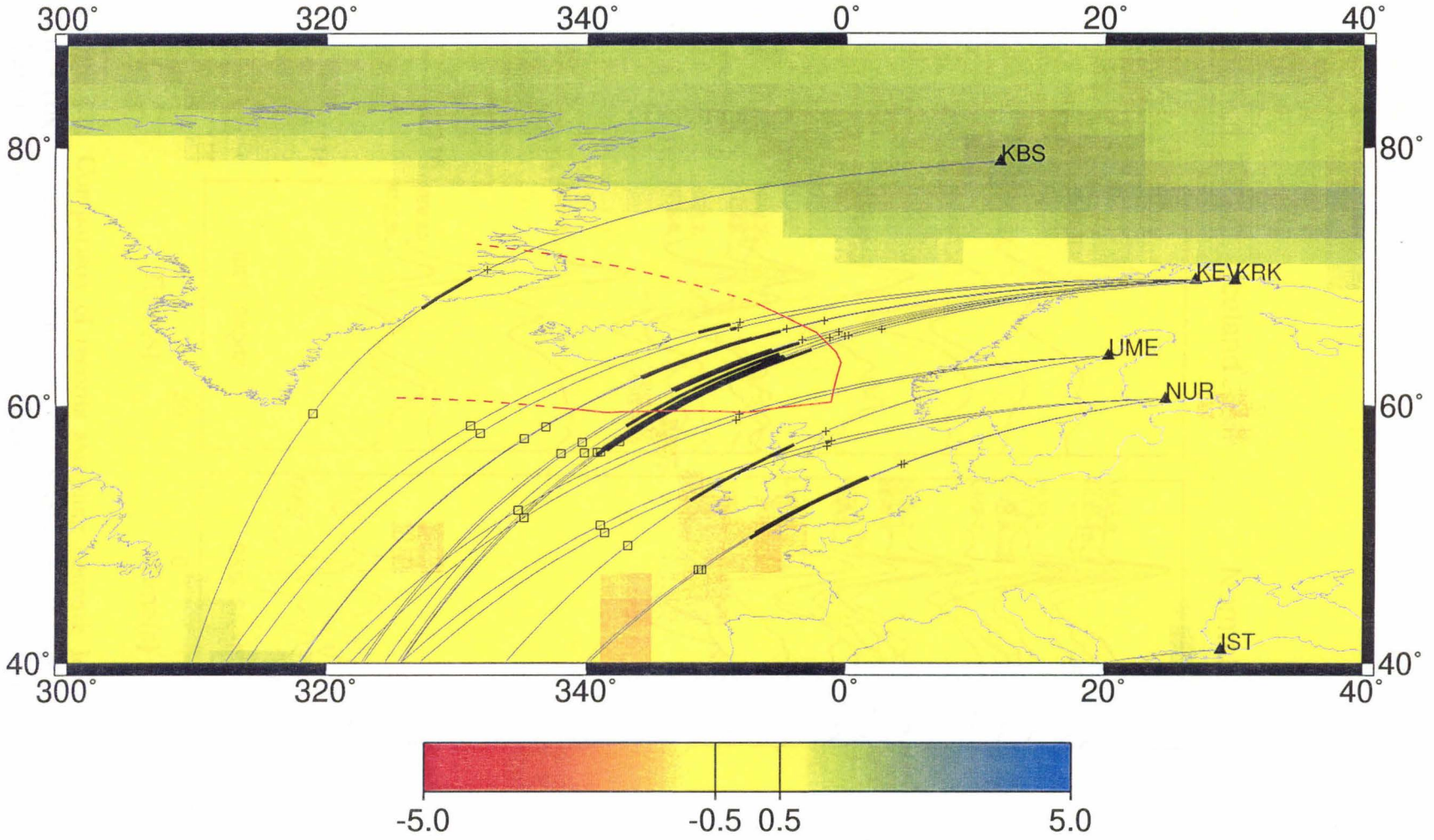

Figure 4.4: Display of where $SK_{P_{diff}}S$ diffract along the CMB(heavy lines) and the exit points of SKS(crosses) and SKKS(squares) from the CMB.

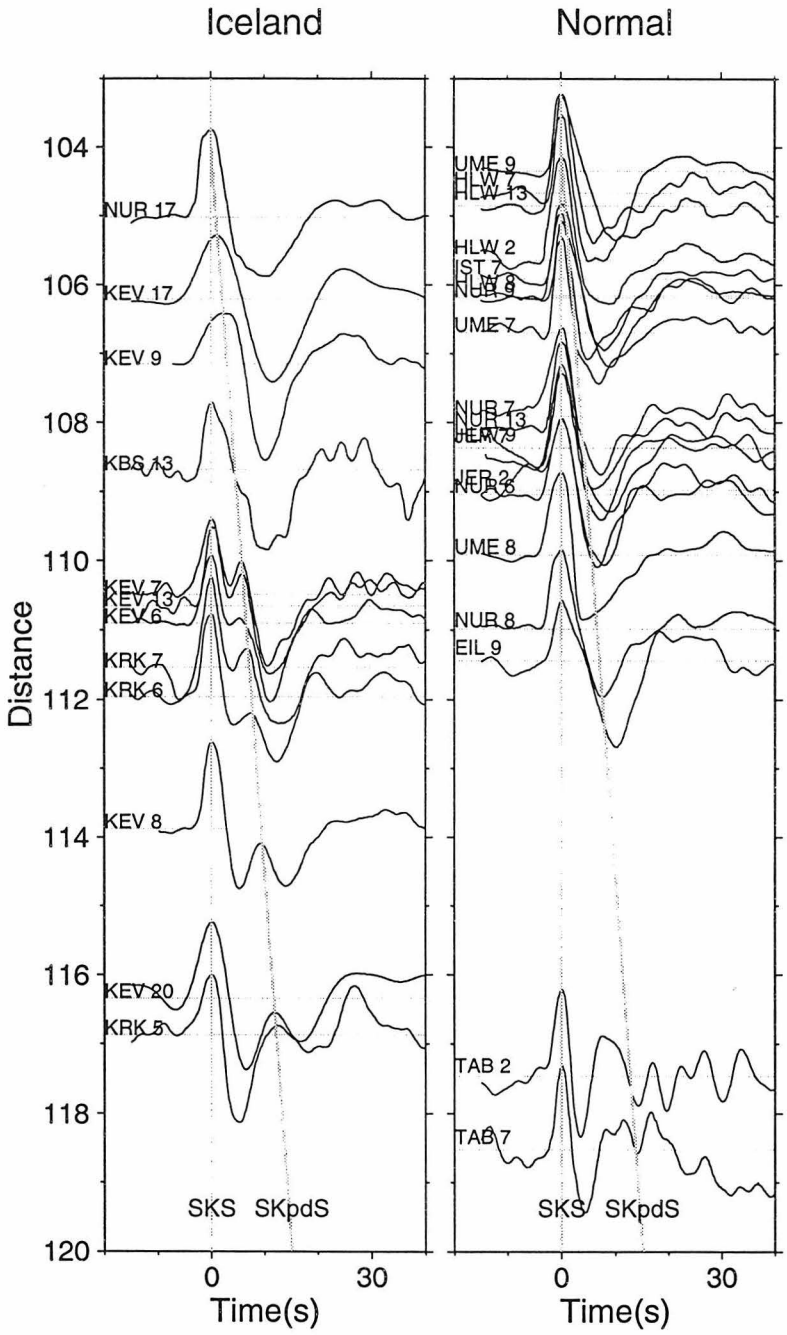

Figure 4.5: Comparison of records sampling beneath Iceland (left) and Northern Africa (right). The gray lines indicate SKS and $SK_{P_{diff}}S$ measured from left panel and are included in right panel for reference. The $SK_{P_{diff}}S$ in right panel behaves like PREM predicted.

4.2 ULVZ beneath Iceland

A detailed comparison of observations sampling the region beneath Europe and northern Africa is displayed in Figure 4.5. The station locations, the projected path segments ($SK_{P_{diff}}S$), and the core exit points of SKS and SKKS are displayed in Figure 4.4. Numbers above the various traces in Figure 4.5 indicate the event as indexed in Table 4.1. Only paths to KEV, KRK and KBS appear anomalous and these observations have been plotted on the left. Many of these events were deep enough to show clear SKKS arrivals but no significant anomalies were identified and therefore SKKS phases have been omitted in the plot. The observations on the right show some variation which is mostly caused by variations in source time histories. In general, they can be compared with those in Figure 4.2 which have been modeled by PREM structures. The record at EIL for event 9 shows a slight complication which is expected at this region. However, the observations on the left indicate a very strong $SK_{P_{diff}}S$ which appears to start developing near 106°.

What is particularly unique about this dataset is that CMB samples by observations at UME and NUR are so close to those sampled by KEV (Figure 4.4). The path going to UME is only 300 km south of the KEV path at the CMB. This suggests a localized structure situated just to the east of the KEV exit point for SKKS. Since KBS shows a strong anomaly, it must also be sampling the anomalous structure. Unfortunately, data from KBS are quite limited.

Modeling the waveforms on the left panel of Figure 4.5 proved quite difficult using classical layered structure. *Garnero et al.* [1993], using a 1D structure, showed that such features can be explained by dropping the P-velocity near the CMB. However, in our case only the path $SK_{P_{diff}}S$ is anomalous because the segments $S_{P_{diff}}KS$ to UME and KEV are nearly identical. Models with different structures at the entry and exit points are discussed in *Helmberger et al.* [1996]. Synthetics from such models were used by *Garnero and Helmberger* [1996] in explaining the anomalies beneath the mid-Pacific. A schematic plot of the significant ray paths following this approach is displayed in the upper panel of Figure 4.6. The source segment produces essentially

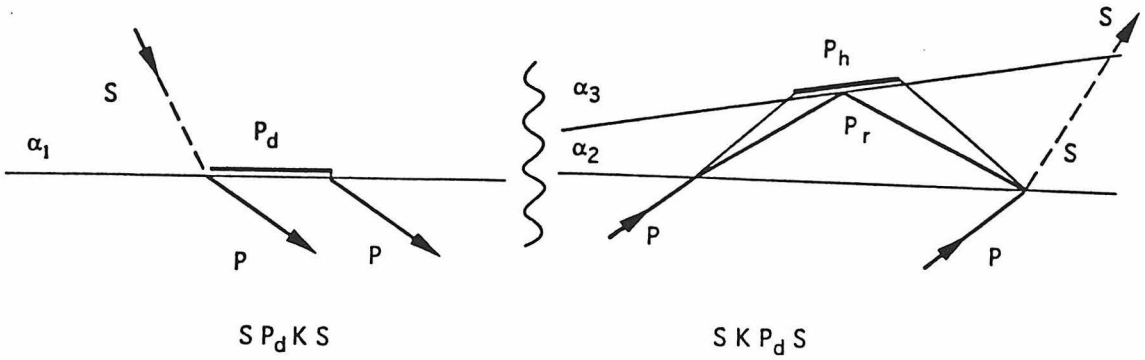

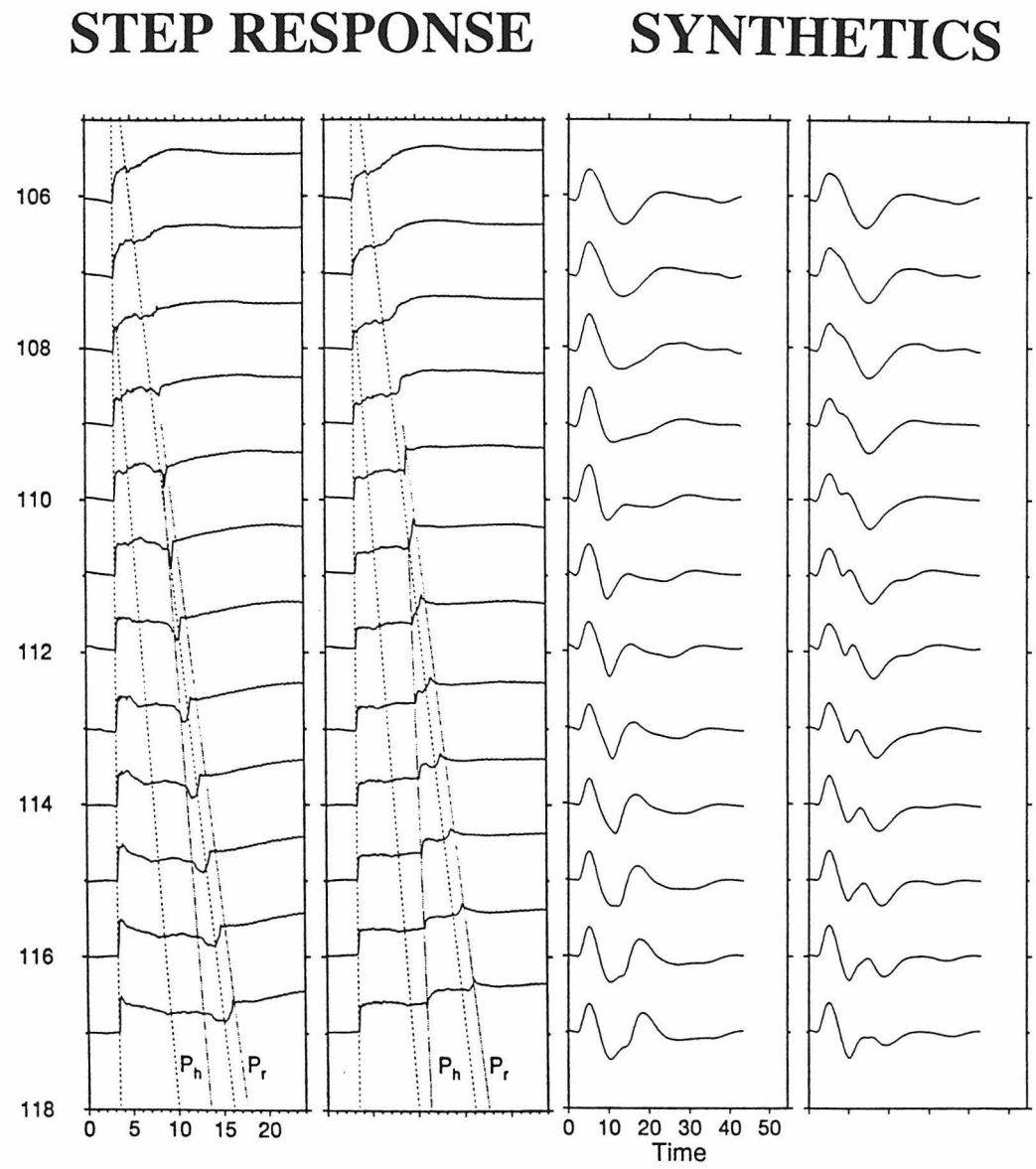

Figure 4.6: Top: Schematic plot of the structure where $S_{P_{diff}}KS$ and $SK_{P_{diff}}S$ samples. Bottom: Step responses and synthetics from two structures with PREM for $S_{P_{diff}}KS$ and 70 km of flat ULVZ and 80 km with 15° dipping base layer.

two arrivals, the SKS part and the $S_{P_{diff}}KS$ arrival (Pd) which has an apparent velocity of α_1 (the P-velocity of PREM at the CMB). At the receiver end, three arrivals become prominent, the normal SKS part, the arrival Pr (a ray reflected back down by the top boundary) which travels with the velocity α_2 since the layer thickness is very thin compared to the horizontal distance and Ph (head-wave traveling along the top) with velocity α_3. These arrivals are illustrated in theoretical responses (step response) but generally show complex interference in long period synthetics as plotted in Figure 4.6.

Column 1 contains a PREM structure on the left ($S_{P_{diff}}KS$) and a 70 km thick layer on the right ($SK_{P_{diff}}S$) where $\alpha_2 = .9\alpha_1$, $\beta_2 = .9\alpha_1$, and the density is from PREM. Column 3 contains the synthetics appropriate for this step response. The dotted lines indicate the various arrivals; the first (SKS), second (Pd), and the third a reference line. The solid line Ph is parallel to Pd, essentially $\alpha_3 = \alpha_1$ and the arrival is offset due to the layer thickness. Critical angle occurs near 110° producing a second arrival which is easily seen for high frequency source histories that are common for Fiji events. The synthetics in this figure contain a (2, 2, 2) trapezoidal source which is appropriate for South American events [*Lay and Helmberger*, 1983a]. Column 2 contains a hybrid model which approximates a locally dipping structure by changing α_3 [*Helmberger et al.*, 1996]. A dipping structure of 15°maps into an increase in $\alpha_3 = 1.25\alpha_1$ and $\beta_3 = 1.25\beta_1$. This greatly increases the reflection coefficient and enhances $SK_{P_{diff}}S$ significantly. Note the high apparent velocity of Ph which allows more of the core to contribute to the family of rays feeding $SK_{P_{diff}}S$. Note that columns 2 and 4 are not record sections of dipping structure but a flat model with inflated α_3 and β_3.

Comparisons of such hybrid models with the observations are given in Figures 4.7 and 4.8 where the main features fit quite well. In Figure 4.8, we have added the 40 km flat-layered synthetics used previously in *Helmberger et al.* [1996]. These synthetics are well documented. While the hybrid synthetics or simulations suggest a dome-like structure, they need to be verified by more rigorous techniques as in *Wen and Helmberger* [1997]. Column denoted dome is from their study assuming a 2D dome 80 km high, 200 km wide with a 10% drop in both P and S velocity. The 2D dome is

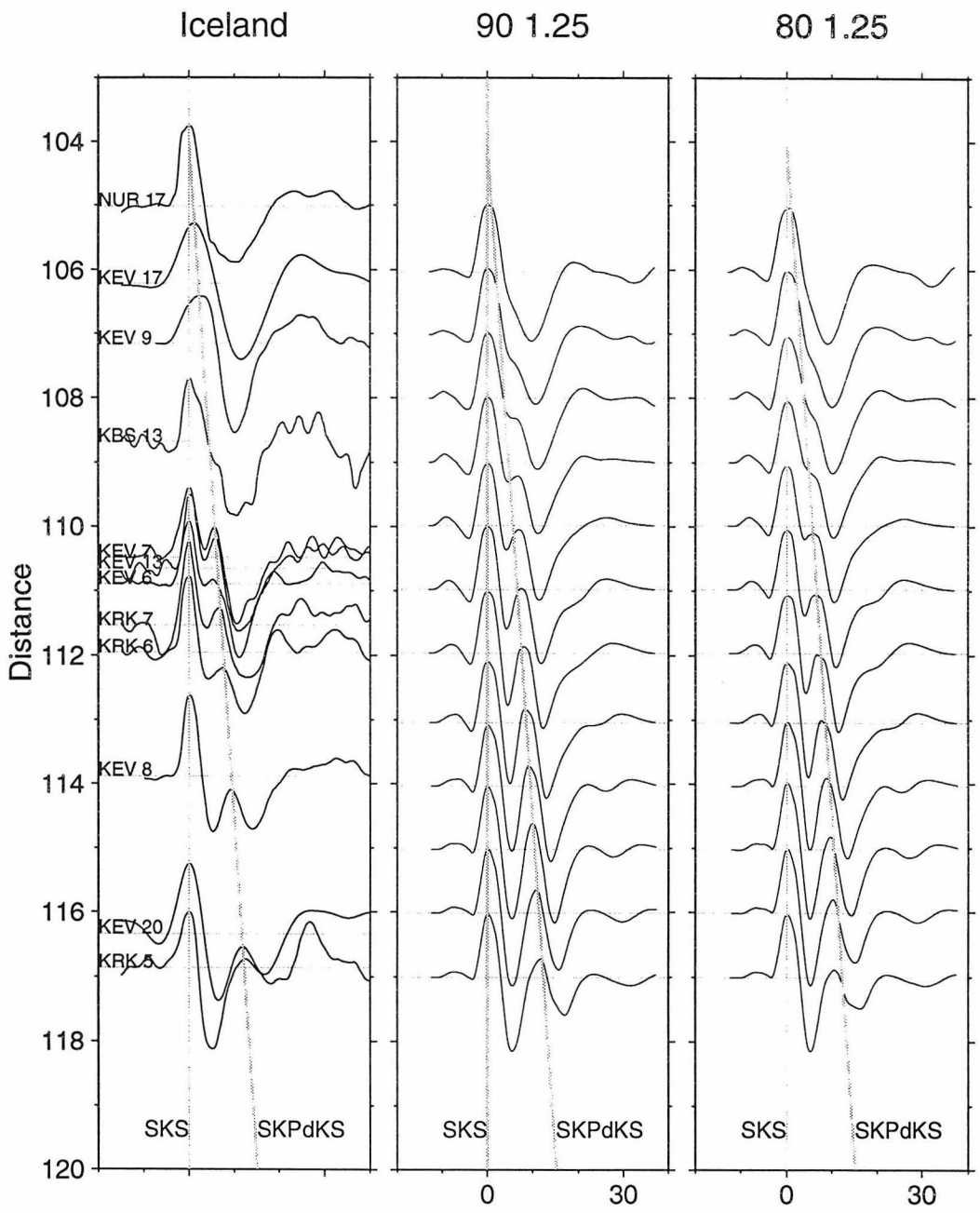

Figure 4.7: Comparison of data (left panel) with synthetics of the model with ULVZ of -10% P velocity drop, 15° dipping structure and thickness of 90km (middle panel) and 80km (right panel) of the mantle. The middle panel shows the arrival time fit the data but the amplitude is too big while the right panel shows the amplitude is about right but time does not fit.

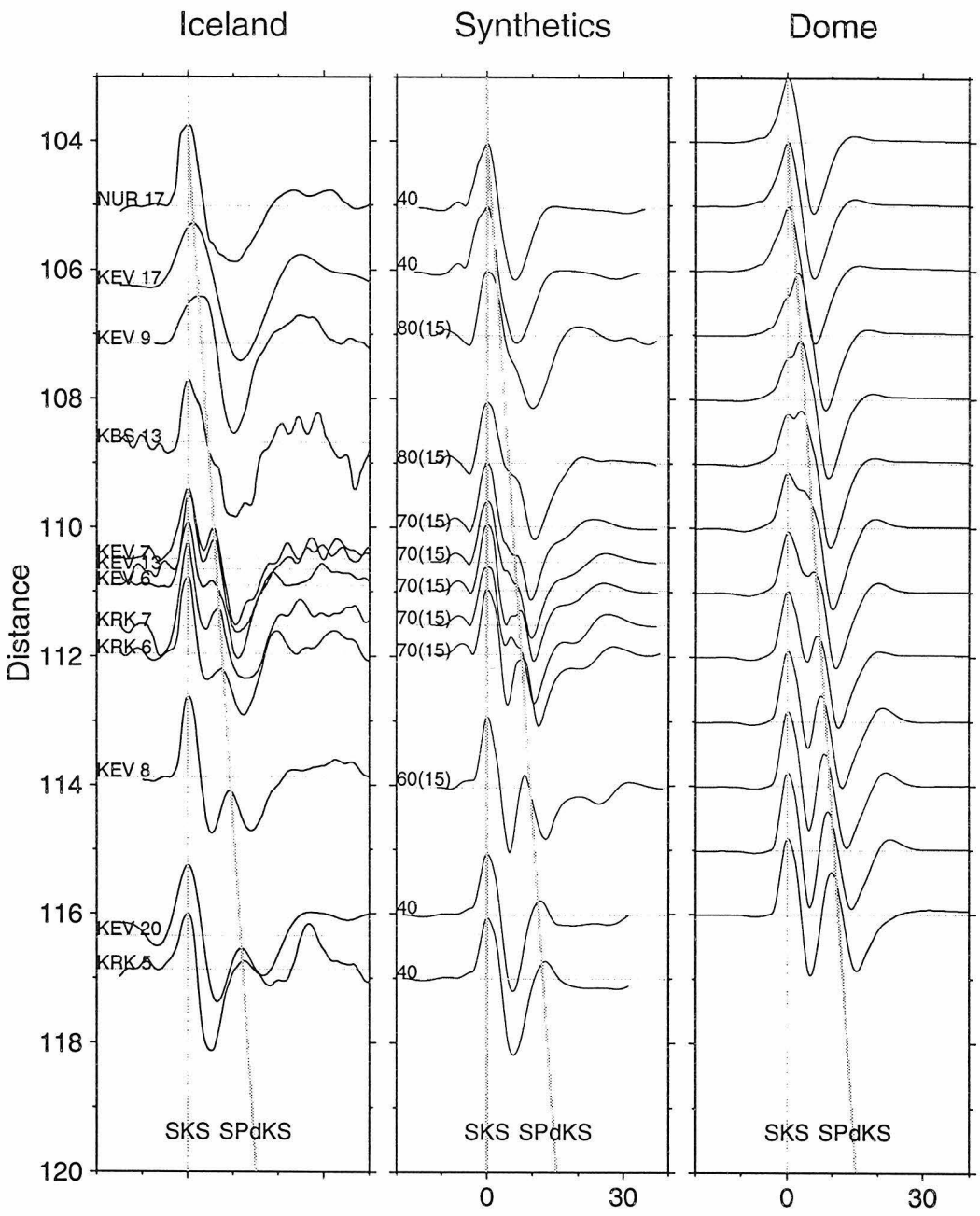

Figure 4.8: Comparison of data (left panel) with synthetics of the 2D simulation (middle) as described in text and synthetics of the 1D hybrid method [*Wen and Helmberger*, 1997]. The numbers in the middle panel are thickness in km and the dipping angles in degrees.

situated between the squares and crosses in Figure 4.4. While this model explains the waveform data quite well, it is somewhat ambitious in that a similar structure less high but with a lower shear velocity can also fit the data as discussed by *Wen and Helmberger* [1997]. Nevertheless, either interpretation suggests a prominent ultra low velocity region below a well-known hotspot (Iceland), which could well indicate some degree of melting [*Williams and Garnero*, 1996].

4.3 LVZ beneath Africa

Unfortunately, there are not very many seismic stations in Africa which makes studying the $S_{P_{diff}}KS$ and $SK_{P_{diff}}S$ phase particularly difficult because of the restricted ranges of observations, 108° to 114°. The only useful samples obtained are from AAE as shown in Figure 4.9. The paths $SK_{P_{diff}}S$ should be sampling the edge of the slow velocities beneath Africa as displayed earlier in Figure 4.1a. Not all of these events are deep as indicated in Table 4.1. Therefore we expect considerable variation in source functions. However, some of these observations are quite anomalous, e.g., events 2 and 4 at ranges near 111°, AAE records from them have shapes similar to KEV waveforms from events 6 and 13, as displayed in Figure 4.9. We conclude that there is probably a ULVZ present, but its lateral extent is difficult to resolve with this limited dataset.

One of the strongest constraints on the LVZ is provided by the behavior of S and SKS as a function of distance. A record section of long-period waveforms displaying the cross-over ranges, 74° to 85°, is given in Figure 4.10. Lines indicating the approximate cross-over distance are included along with a 1D profile of synthetics for PREM. Obviously, the cross-over for the synthetics occurs much earlier than in the observations.

Identifying phases when strong lateral variations are present can be quite difficult. Many times the short-period observations can be useful for this purpose as displayed in Figure 4.11. In the right panel, we can identify the ScS phase since it appears to be in-phase with SH (LPT) and out-of-phase with SV (LPR). The identification of

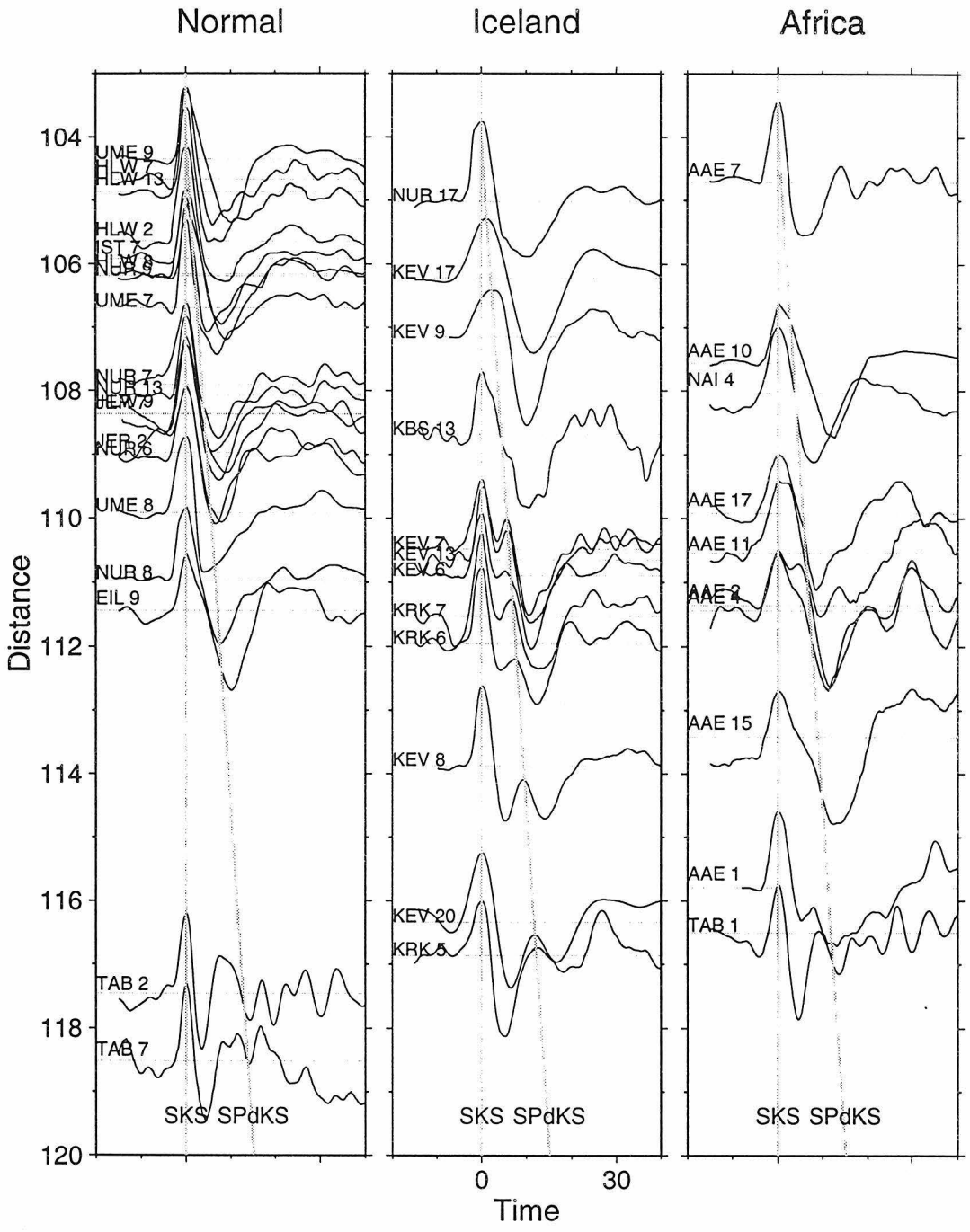

Figure 4.9: Left panel show the seimograms compatible with PREM, middle panel is data sampling beneath Iceland and right panel is data for AAE station.

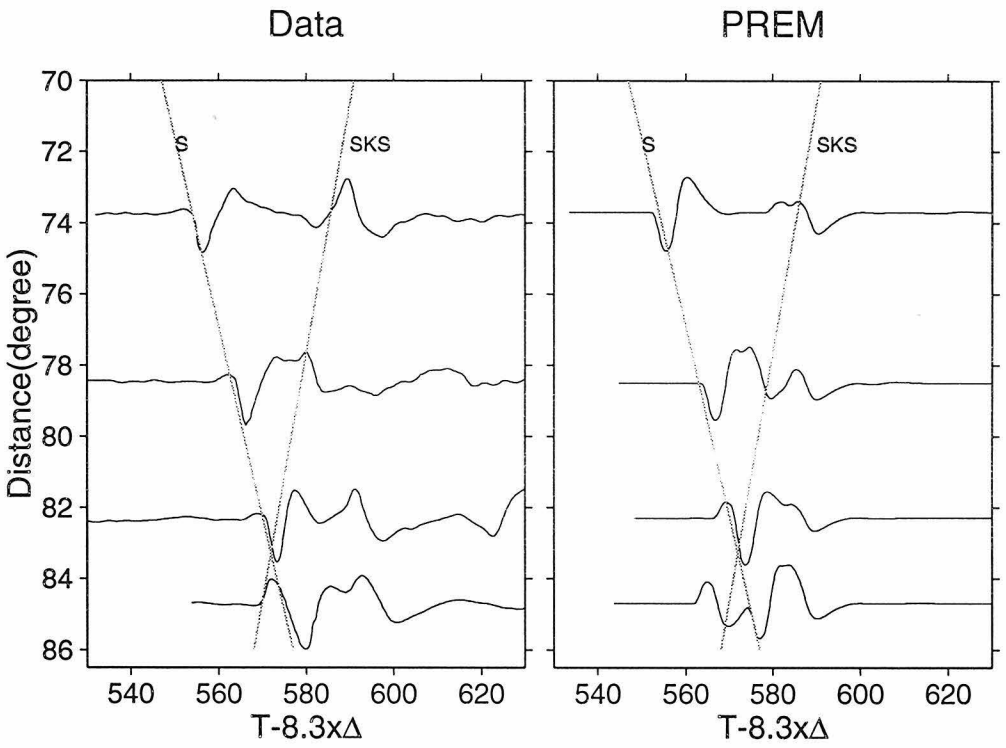

Figure 4.10: Comparion of records from 70° to 86°. Note the difference in the last trace. The cross-over in PREM occurs too early.

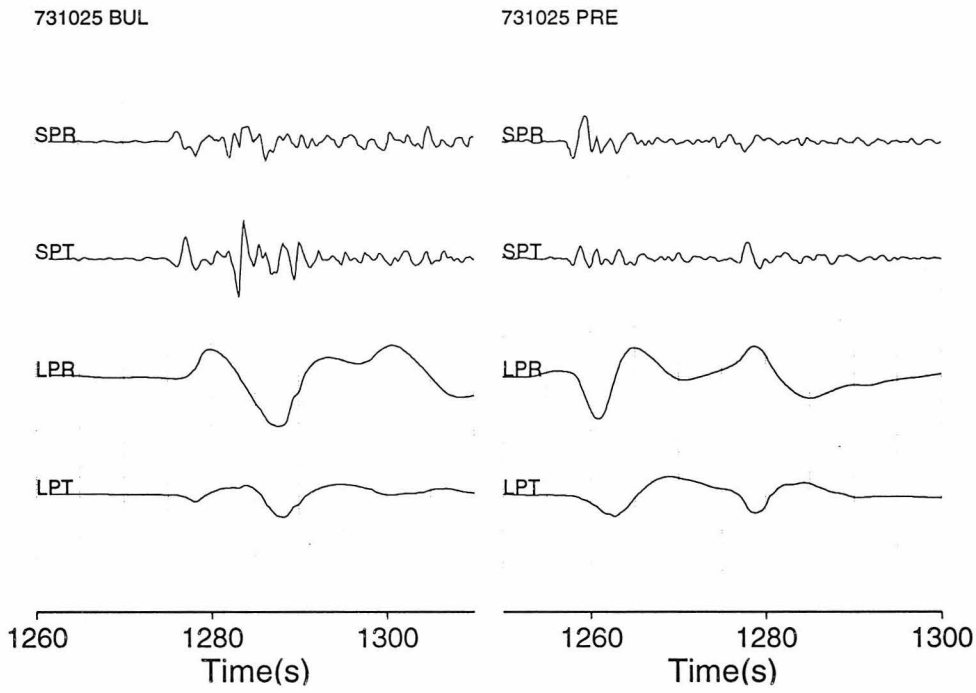

Figure 4.11: The long period and short period seismogram recorded on BUL from event 10.

SKS is more subtle but since the SPR and SPT start together, we can assume the first arrival is S. Since SKS occurs slightly later, it should make the long-period SV signal shorter-looking than the SH waveform which appears to be the situation. The separation between the first arrival with ScS as measured on SPT agrees well with the long-period estimate. Unfortunately, short-period ScS cannot be identified in the left panel as is usually the case for South African observations. However, the separation between SKS and S in the left panel is quite obvious except that SKS should not be so strong on the SPT components.

4.3.1 Travel-time analysis

Recordings at the five stations in Southern Africa and two in Central America (Figure 4.1a) from relatively deep events were analyzed in detail. The locations and index of events are given in Table 4.1. The travel-time picks were made from a combination of long-period and short-period records following the procedure discussed with respect to Figure 4.11. The raw data plotted as a PREM-residual is given in the upper panel of Figure 4.12. The open symbols are from the central African stations, AAE and NAI, and are late relative to South Africa stations as predicted by station statics [*Dziewonski and Anderson*, 1983]. South Africa stations, BUL, PRE, and SLR are slightly negative, while GRM, WIN, and SDB are slightly positive in terms of P-wave residuals. The stations AAE and NAI have large positive P residuals of 2.1 and 2.5 seconds respectively, which we have mapped into S-wave residuals by multiplying by 1.8. This brings down the rather large bias at distances greater than 100° which is dominated by these two stations. The data has also been corrected for event shifts by normalizing to common stations, i.e., base line shifted. The results are presented in the lower panel of Figure 4.13. Note that after these corrections, the solid and open symbols appear to form one population although with a large scatter. This scatter is probably caused by the strong lateral variation suggested in Figure 4.1a. Unfortunately, we do not have sufficient waveform data to warrant a 3D model so that we will simply attempt to explain the data with a 2D profile crossing this structure. A

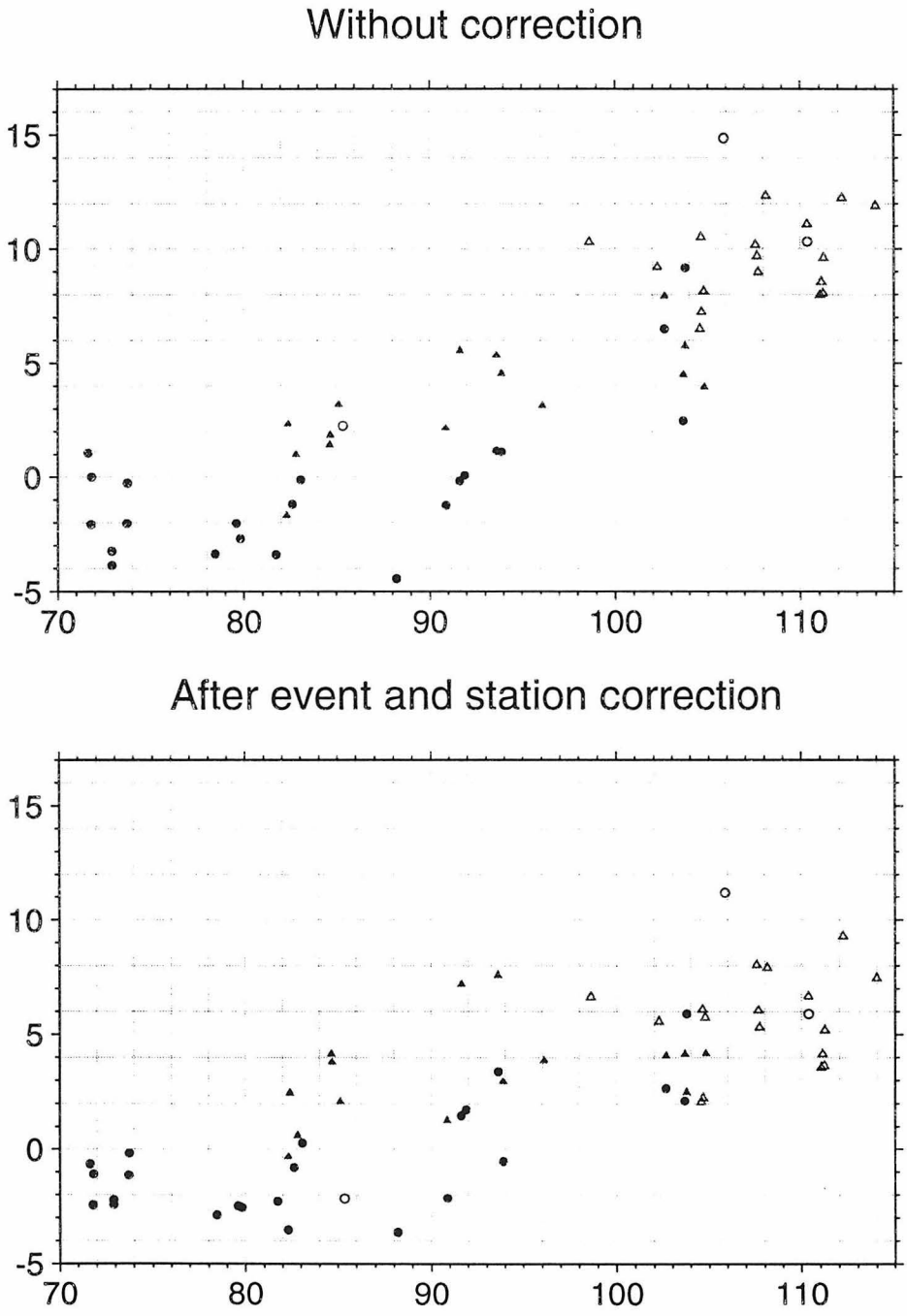

Figure 4.12: a) SKS(triangles) and S(dots) travel time residuals relative to PREM. Open symbols are for station NAI and AAE. b. Time residuals after event and station correction.

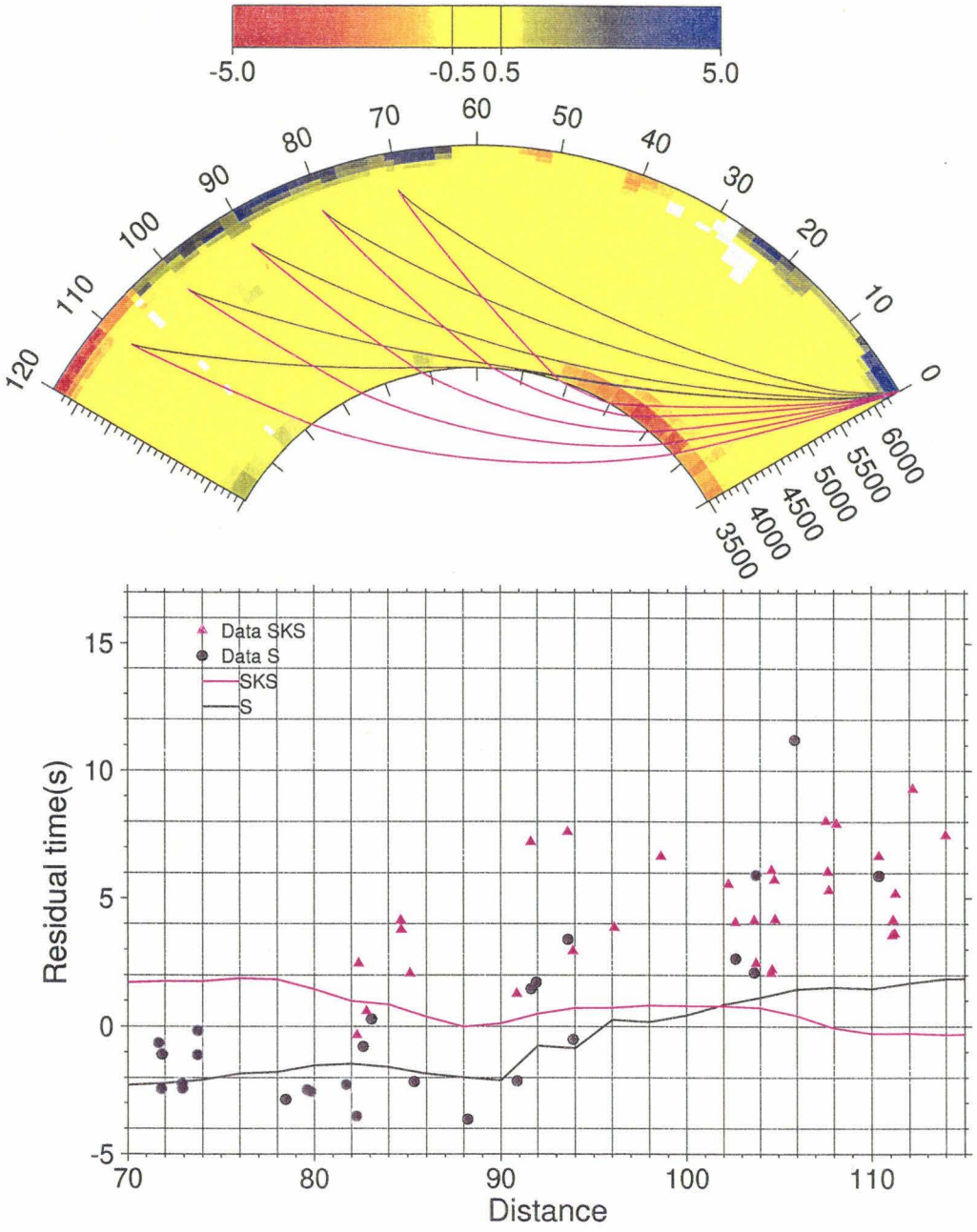

Figure 4.13: top: Profile from *Grand* [1994] through great circle (20°S,30°E) to (2°S,77°W) starting from (20°S, 30°E). Raypaths of S and SKS with the source depth 550km are also included. bottom: The SKS and S residuals from the model are displayed with the corrected data.

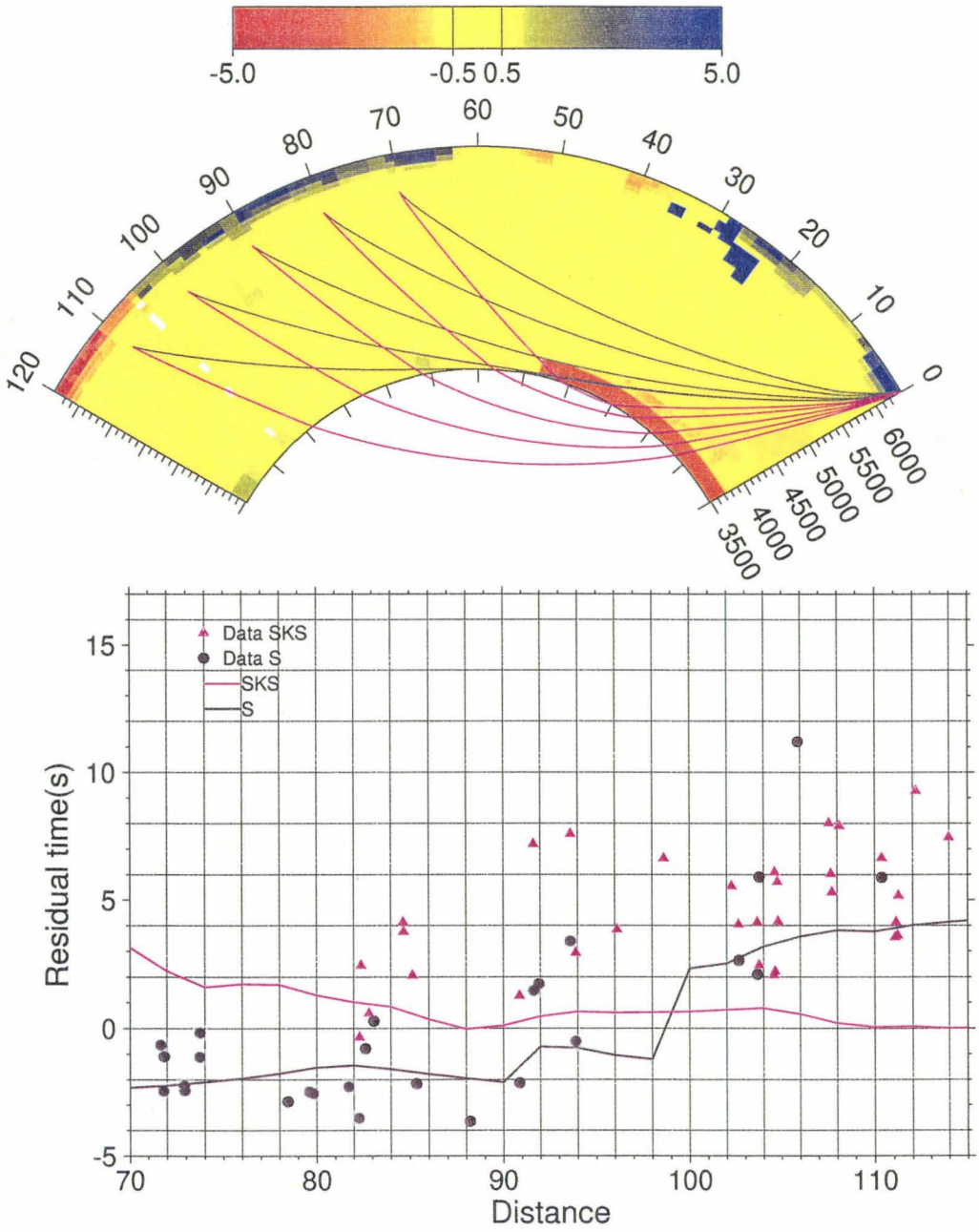

Figure 4.14: top: Profile from *Grand* [1994] with enhanced base layer through great circle (20°S,30°E) to (2°S,77°W) starting from (20°S, 30°E). Raypaths of S and SKS with the source depth 550km are also included. bottom: The SKS and S residuals from the model are displayed with the corrected data.

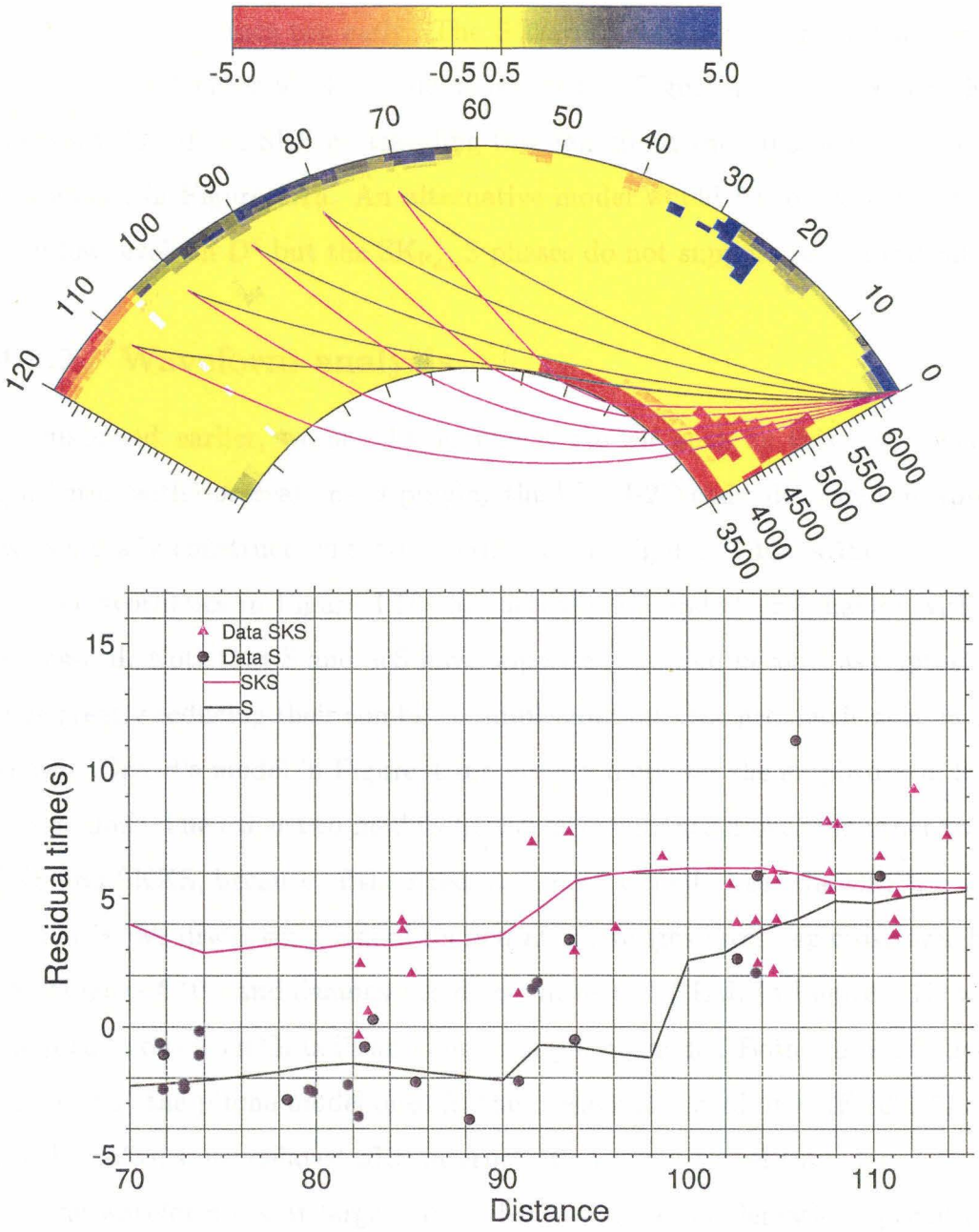

Figure 4.15: top: Profile from *Grand* [1994] with enhanced base layer and plume structure through great circle (20°S,30°E) to (2°S,77°W) starting from (20°S, 30°E). Raypaths of S and SKS with the source depth 550km are also included. bottom: The SKS and S residuals from the model are displayed with the corrected data.

comparison of travel-time predictions from Grand's model is presented in Figure 4.13 assuming essentially a 2D profile through station PRE. The agreement for S is quite good over the range 70° to 90° but underestimated at larger distance suggesting a lower velocity in D″ (see raypaths in the upper cross-section). The predictions for SKS are about 6 secs too early. The S travel-times can be easily fixed by decreasing the D″ velocities to -4% as demonstrated in Figure 4.14. To fix the SKS times, we must slow down SKS by traveling through about the same length of red zone as introduced in Figure 4.15. An alternative model would be to drop the velocities to very low levels in D″ but the $SK_{P_{diff}}S$ phases do not support such a radical solution.

4.3.2 Waveform analysis

As discussed earlier, we should document models such as this one by comparing synthetics with observations. Applying the WKM-2D code, discussed in Appendix A, we can easily construct synthetic sections as in Figures. 4.16a–4.16d.

The synthetics in Figure 4.16a are actually 1D and their behavior with distance is classical. Note that S and ScS have opposite signs and become asymptotic in time, thus greatly reducing their combined amplitudes into the geometric shadow as is well known. Grand's model in Figure 4.16b greatly increases the amplitude of S well into the shallow. The other two models particularly enhance S over the other two phases, SKS and SKKS, because of their reduced shear velocity near the CMB.

Earlier we discussed a record section at the ranges involving cross-over from S to SKS(Figure 4.10), and demonstrated the misfit to PREM. In Figure 4.17, we display the predictions from Grand's and our favor plume model. Both models fit better than PREM but the plume model does fit the cross-over record at PRE (82.3°) quite well which confirms our delayed SKS interpretation of the travel-time data.

The waveform fits at larger ranges become more problematic, especially with respect to the S-wave which is into the shadow. As in recent CMB studies [e.g., *Garnero and Lay*, 1997], considerable shifts in diffracted SH vs. SV are observed and interpreted as anisotropy. Figure 4.18 presents some of our data where we have included

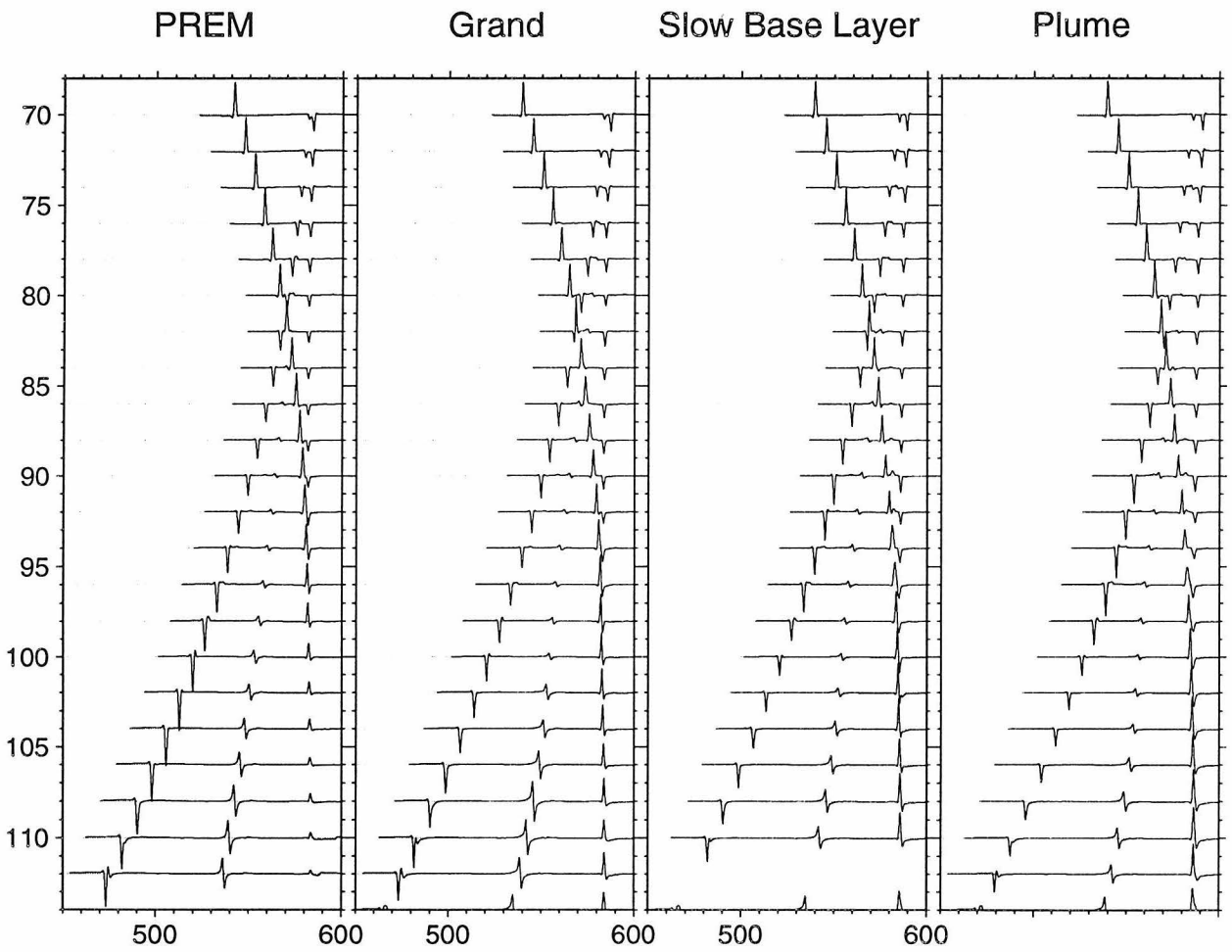

Figure 4.16: Synthetics for PREM[*Dziewonski and Anderson*, 1981] and models displayed in Figure 4.13, 4.14, 4.15.

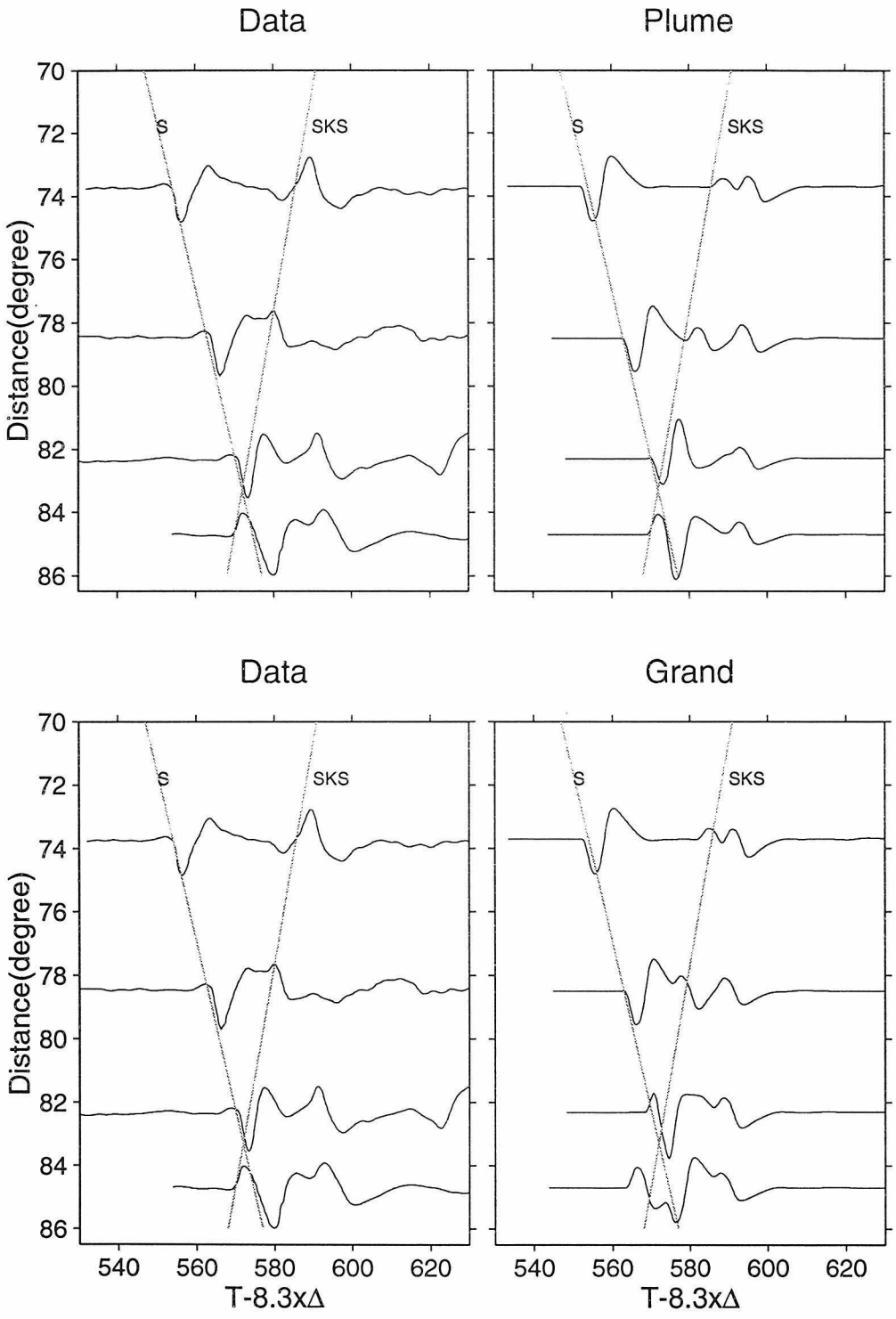

Figure 4.17: Comparion of records from 70° to 86° with *Grand* [1994] and plume model.

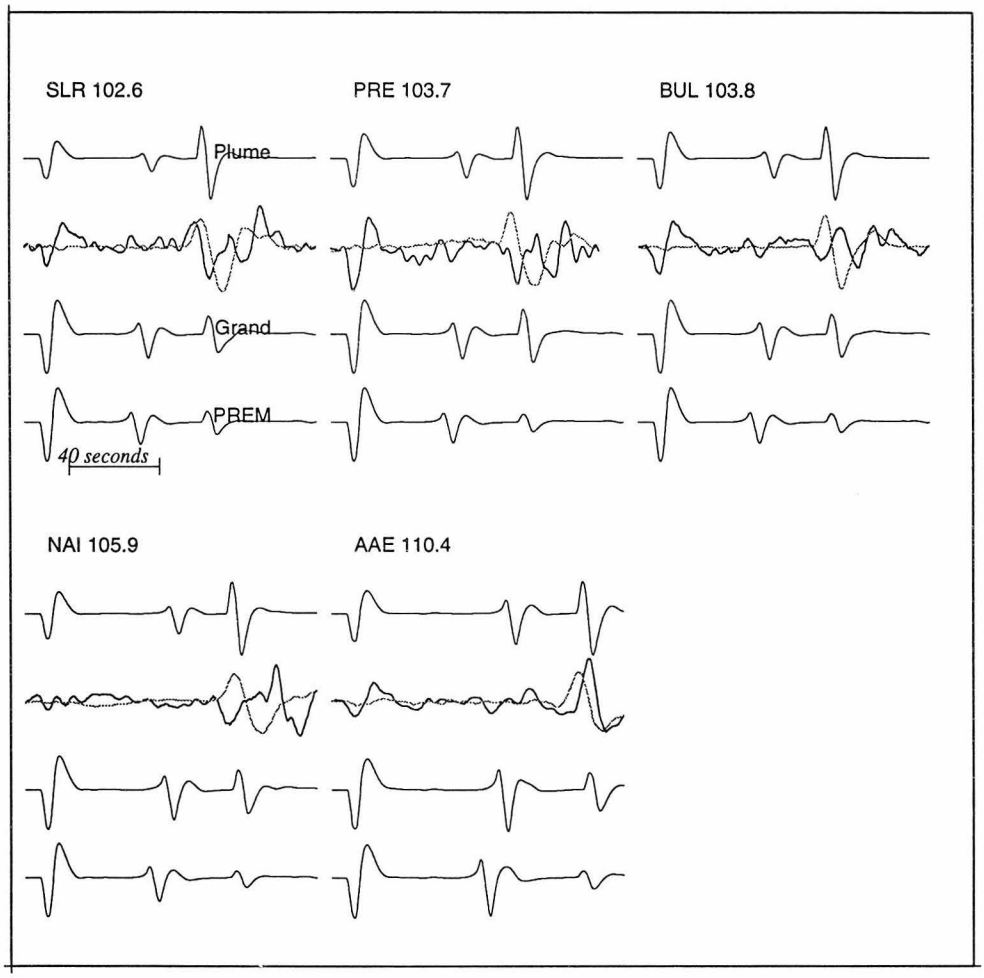

Figure 4.18: Synthetics for different models compared with data beyond 100°.

the tangential component (SH) as dotted traces. Sometimes SV is early (SLR,102.6°) and sometimes SH is early, (AAE, 110.4°). This may be caused by anisotropy or 3D scattering. However, the main point is that Sdiff is relatively strong and both SKS and Sdiff are late.

4.4 Discussion

In this chapter we investigated two structures at the base of the mantle with contrasting scale lengths. The African anomaly has associated with a large scale feature ($\sim$ 3000 km) [e.g. *Su et al.*, 1994], and is sometimes referred to as super-plume. The long wavelength lower mantle structure is revealed both in slow direct S-waves[*Masters et al.*, 1996] and in differential times [*Masters and Shearer*, 1992]. This structure is similar to the central Pacific anomaly with a 2 to 4% drop in shear velocity in the bottom most layer of the mantle according to these studies. These models do not use the SKS-S data studied here and do not predict their behavior well. Grand's model does better but since tomographic models tend to smooth anomalies we need to sharpen it (personal communication)fro. The basic model presented by *Grand* [1994] which has been recently updated appears to be correct with a plume looking structure upwelling beneath eastern Africa. The primary evidence for this structure is about 5 seconds delay in SKS raypaths sampling this zone and the delayed cross-over of S to SKS. Synthetics generated from Grand's model with enhanced velocity anomalies fit record sections quite well confirming the travel-time interpretation of the data. The dimensions of the plume-like structure has not been resolved in this study although it extends upward about 1500 km in the present model. For example, a decrease the velocity drop from -4% to -8% would reduce the vertical extent by a factor of 2. The width is also not determined except that it must be at least 500 km across at the base of the mantle. The structure modeled here is essentially 2D extending NS. However, the study by *Tanaka and Hamaguchi* [1992] involving NS sampling of S and ScS finds that the anomaly ends about the equator or beneath NAI, see Figure 4.1a. They suggest a horizontal length of about 500 km (NS) based

on ScS-S differential times of 4 to 8 residuals which maps into a D″ with reduced velocities of -2.5% to -5%. They also suggest that Q is low in this zone which may explain why the phase ScS is not apparent in many of the records used in this study. While the African anomaly is large in dimension influencing nearly all phases and prominent even in long period tomographic studies the LVZ structure beneath Iceland is very small. There are no anomalies in differential travel times of S, SKS, or SKKS. It is not apparent in Grand's present model although he has recently found an event located in Hindu-Kush as recorded in North America that reveals its presence.

The only feature that is common to these two structures is that two of the latest arrivals in the ISC catalog are KEV (Iceland) and NAI (Africa). This may be fortuitous but future studies may reveal the connection.

Chapter 5 Possible Upper and Lower Inner Core Structure

5.1 Abstract

Recent papers have introduced an asymmetry in the anisotropic structure of the Inner Core, *Su and Dziewonski* [1995], and hemispheric variations, *Tanaka and Hamaguchi* [1997], *McSweeney et al.* [1997], with large scatter in individual picks. We propose an interpretation of this data in terms of a transitional structure mostly isotropic (upper) surrounding the anisotropic (lower) inner core with possible variable thickness. We suppose that the interface between these structures is complex and scatters short-period signals similar to Upper-Mantle structure and is most easily studied at longer periods. In this paper, we model broadband PKP triplication data at ranges 146° to 154° from South Sandwich Island to northwestern North America and show that these waveforms are consistent with an isotropic layer above 300 km thick overlaying in anisotropic (5%) lower inner core.

5.2 Introduction

The seismic velocity structure of the inner core has taken a quantum jump in importance with the discovery that it depends on time, *Song and Richards* [1996] and *Su et al.* [1996]. *Su and Dziewonski* [1995] suggest that the pole of anisotropic symmetry is roughly 10° away from the spin-axis and if the mantle is spinning at a rate different from the core, one should see a change in absolute times of the DF branch of the PKP phase along nearly NS paths, see Figure 5.1. Since the predicted variation in time is only a few tenths of a second, this measurement is very difficult without a controlled source geometry. Variation in differential times (BC-DF) is easier to determine since

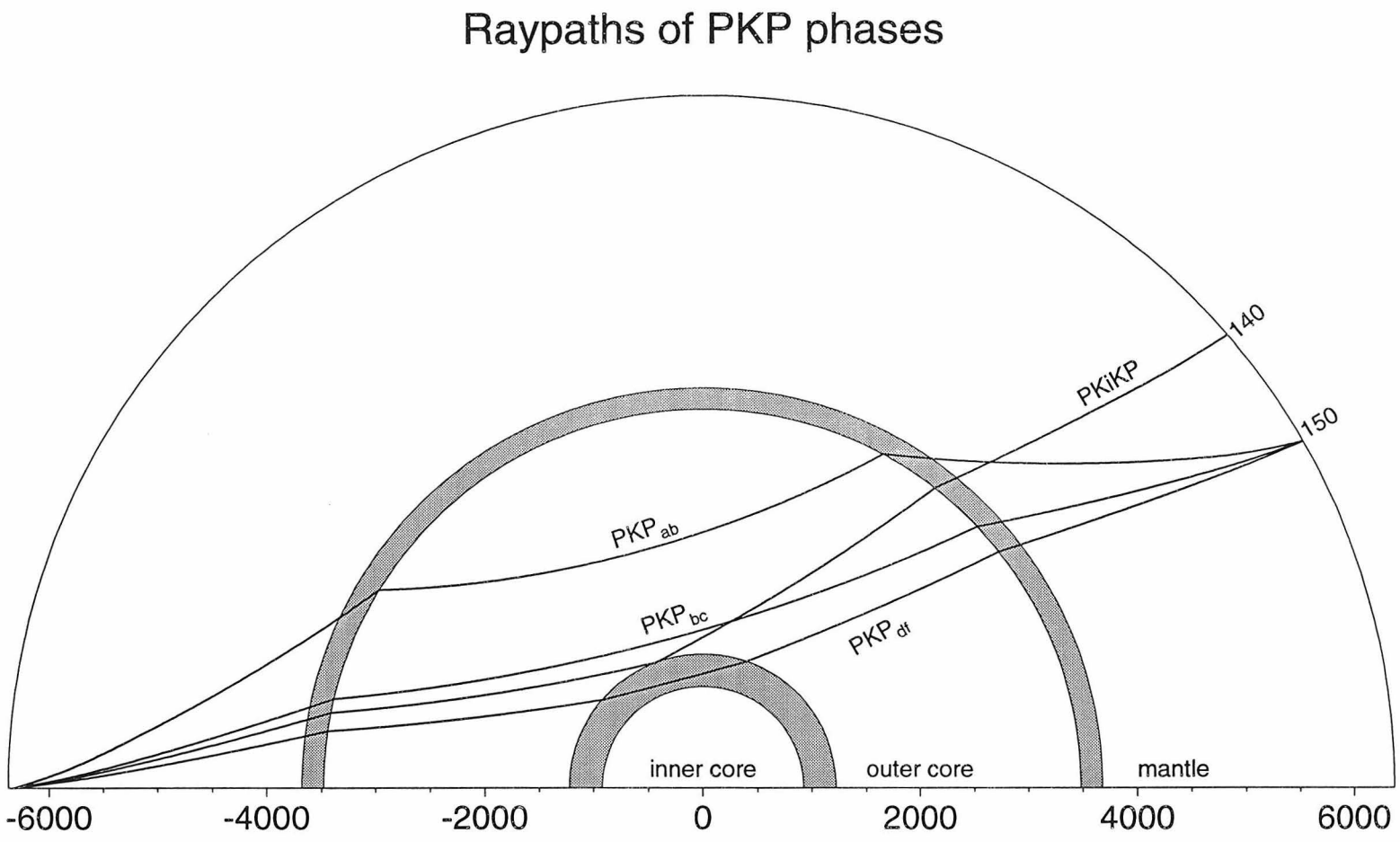

Figure 5.1: Ray paths associated with the PKP family.

the problems of exact location, origin time and 3D path correction in the upper mantle can be avoided, *Song and Richards* [1996]. However, mapping changes of this differential time into differential spin rates requires detailed knowledge of the Inner core anisotropic structure. In short, to understand how it varies in time is obviously coupled to what the structure is with time-fixed. It would appear that the inner core must be anisotropic as recent papers confirm, see recent review by *Song* [1997], and on average, it must be between 3 and 5% faster along NS paths as compared to EW paths. However, seismograms produced by paths along the spin-axis show considerable variation in the characteristics of the DF branch both in timing and waveform. For example, paths from Sandwich Island to College, Alaska are consistently faster than paths from Macquarie Islands to northwest Europe, *Shearer* [1994] and others. The most recent reports on the analysis of short-period travel peaks comes from *Tanaka and Hamaguchi* [1997], and *Creager* [1996] who both report on strong hemispherical variations, up to 2 secs shifts averaged over large areas. However, the data show very large scatter even in differential PKP (BC-DF) times. Large scatter in PKP (AB-DF) is expected based on the large variation in D" structure, see *Song and Helmberger* [1997], *Garnero and Helmberger* [1997], and many others. Even long-period waveform modeling shows that variation of up to 2 sec are common, *Song and Helmberger* [1995b]. Scatter in PKP (BC-DF) is more difficult to explain without variation in the inner core, since the two ray paths are near each other when crossing the CMB, as displayed in Figure 5.1.

Not only is there considerable scatter in differential times between (BC-DF) for paths along the spin-axis, there is also considerable complexity of the DF waveforms as displayed in Figure 5.2. The observations are aligned on BC. The reference lines for PREM2, *Song and Helmberger* [1995b] is labeled (DF) and the (Da, Fa) indicates the earlier arriving anisotropic predictions for possible models presented in Figure 5.3. Generally, the DFa branch is weak and complex as recognized by many researchers,*Masters* [1993]. One possibility is that this feature is produced by a triplication similar to the short-period complexity found in upper-mantle phases. Moreover, if this transition is irregular as is the case for upper-mantle phases, we

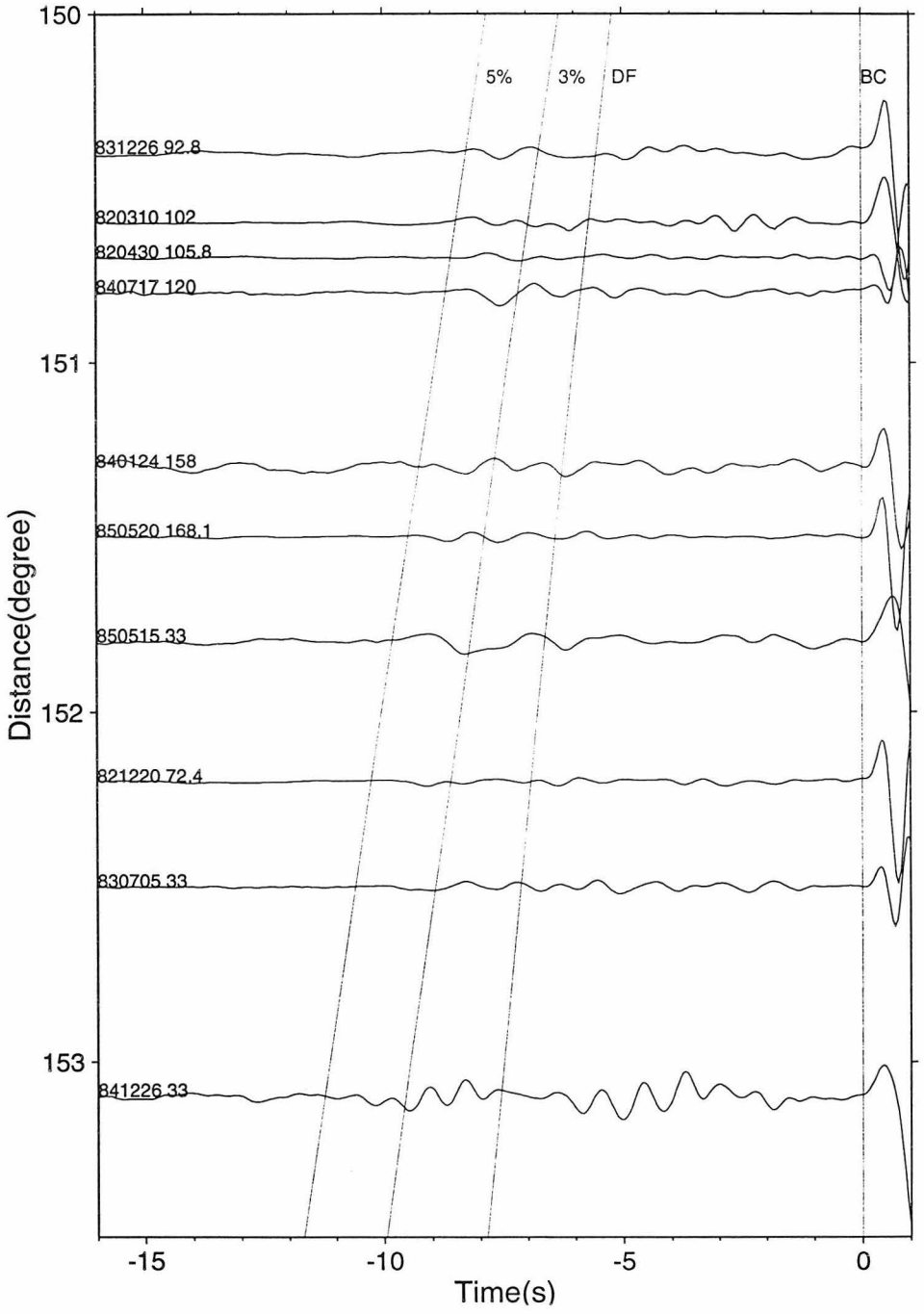

Figure 5.2: Short-period set of (College, Alaska) records displaying the onset of the PKP(DF) branch relative to BC. The traces are aligned with the BC arrival. The lines indicate the predicted arrivals from PREM2 (normal) and models containing triplications, see Figure 5.3.

would expect to see considerable variations in differential times (BC-DFa).

The evidence for a transition zone, outer inner core (OIC), of isotropic material surrounding an anisotropic inner-inner core (IIC) has been suggested by *Song and Helmberger* [1995a]. They proposed the model displayed in Figure 5.3, PREM2-NS, to reconcile the lack of any measurable differential anomalies in NS (PKiKP - PKIKP) values at ranges 130 to 146°. However, their model does not fit the long-period waveforms at COL very well as displayed in Figure 5.4. While PREM2 predicts long-period (EW) waveshapes very well, it does poorly on NS paths as displayed in the top trace. The model PREM2-NS predicts a better fit but a thicker layer (300 km) with a 5% jump fits better with a broadened first arrival (DF). The main objective of this paper is to establish this structure along this particular path, sample beneath the Caribbean as displayed in Figure 5.5.

5.3 Long-period modeling of the OIC structure

Modeling long-period P-waves from shallow earthquakes has become a mature science, but requires studying individual earthquakes in detail. Deep events are much earlier to study since the triplication distortions can be separated from surface reflections. Figure 5.6 displays a simple set of PKP synthetics for this case assuming the models given in Figure 5.3 shows the broadband response for comparison with modern IRIS instruments along with analog Worldwide Seismic Net responses on the bottom. The major branches, DF, BC, and AB are easily identified at these ranges. However, the DF waveform shows considerable broadening at ranges 147 to 153° moving left to right. This feature is quite clear in observed record sections as displayed in Figure 5.6 and 5.7. Constructing this section was difficult because of the lack of strong deep events. Thus, we have a collection of deep events and a few shallow events that appear to be dominated by PKP with a weak pPKP phase (see Table 5.1). When we compare our synthetics with these shallow events, for example, event 7, we are only concerned with the beginning motions (10 sec). Most of the deep events show good fits over the complete PKP waveform assuming the 5% jump.

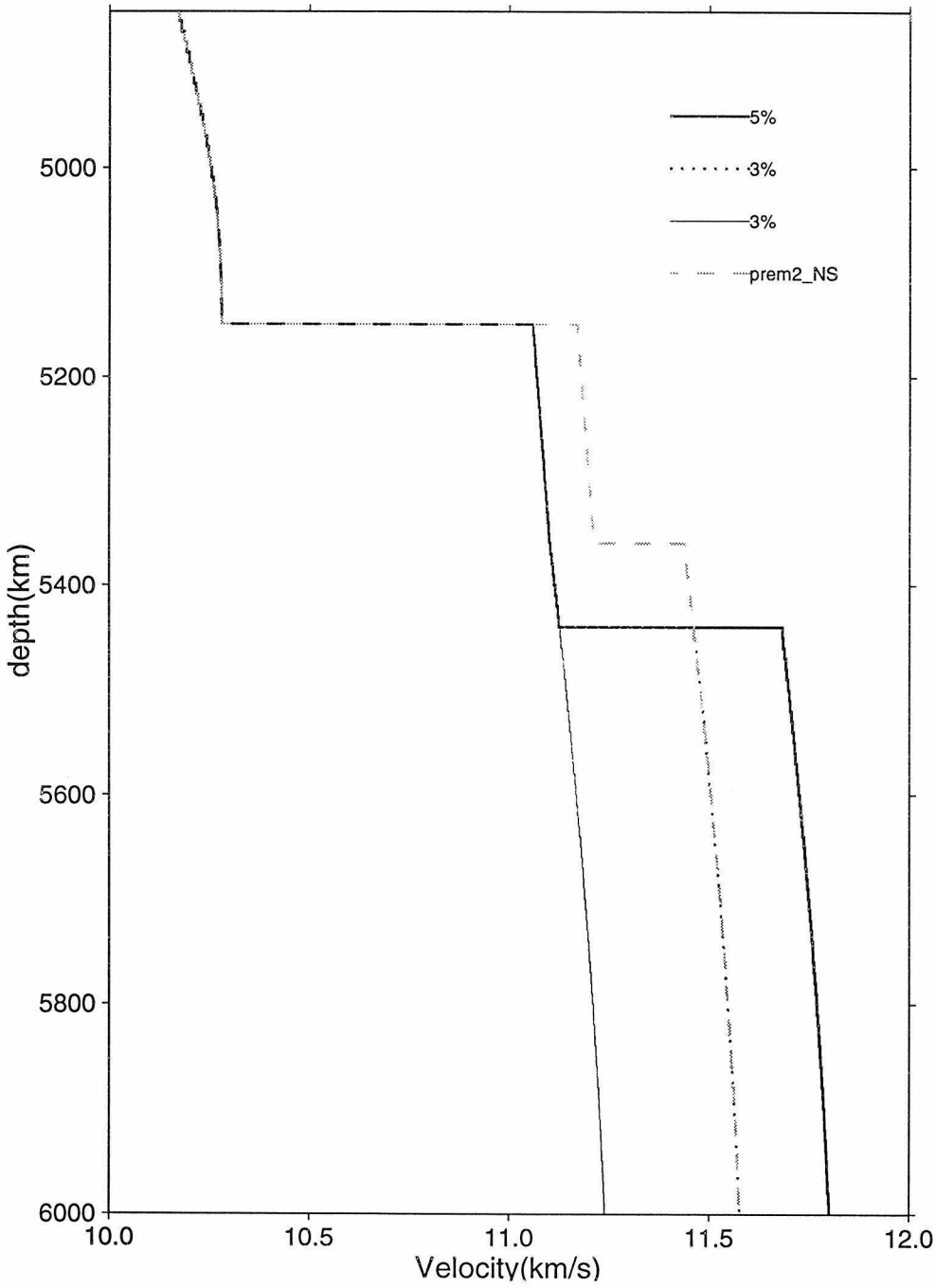

Figure 5.3: Possible models of inner core anisotropy appropriate for NS path.

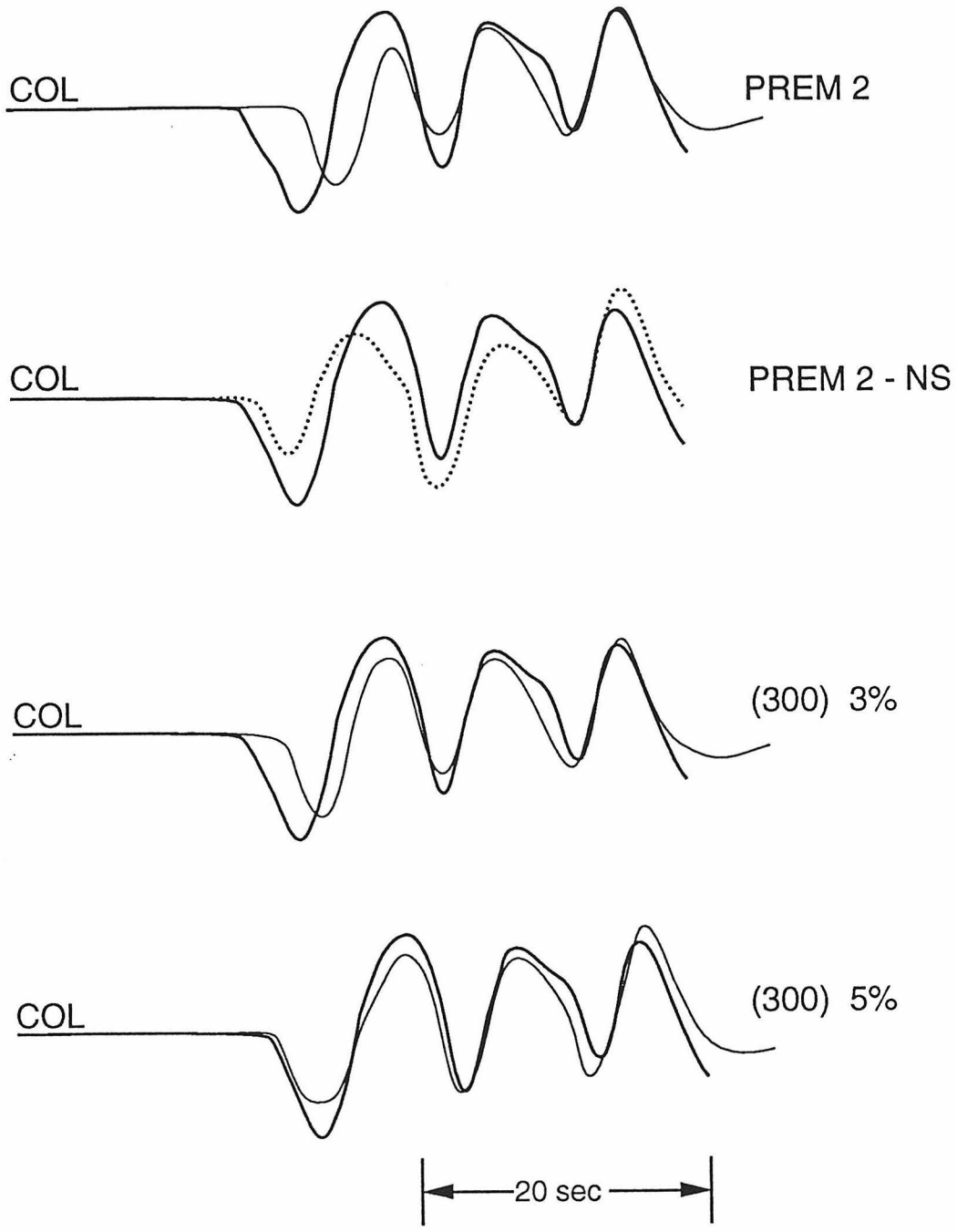

Figure 5.4: Comparison of a long-period observation at College, Alaska with four possible models.

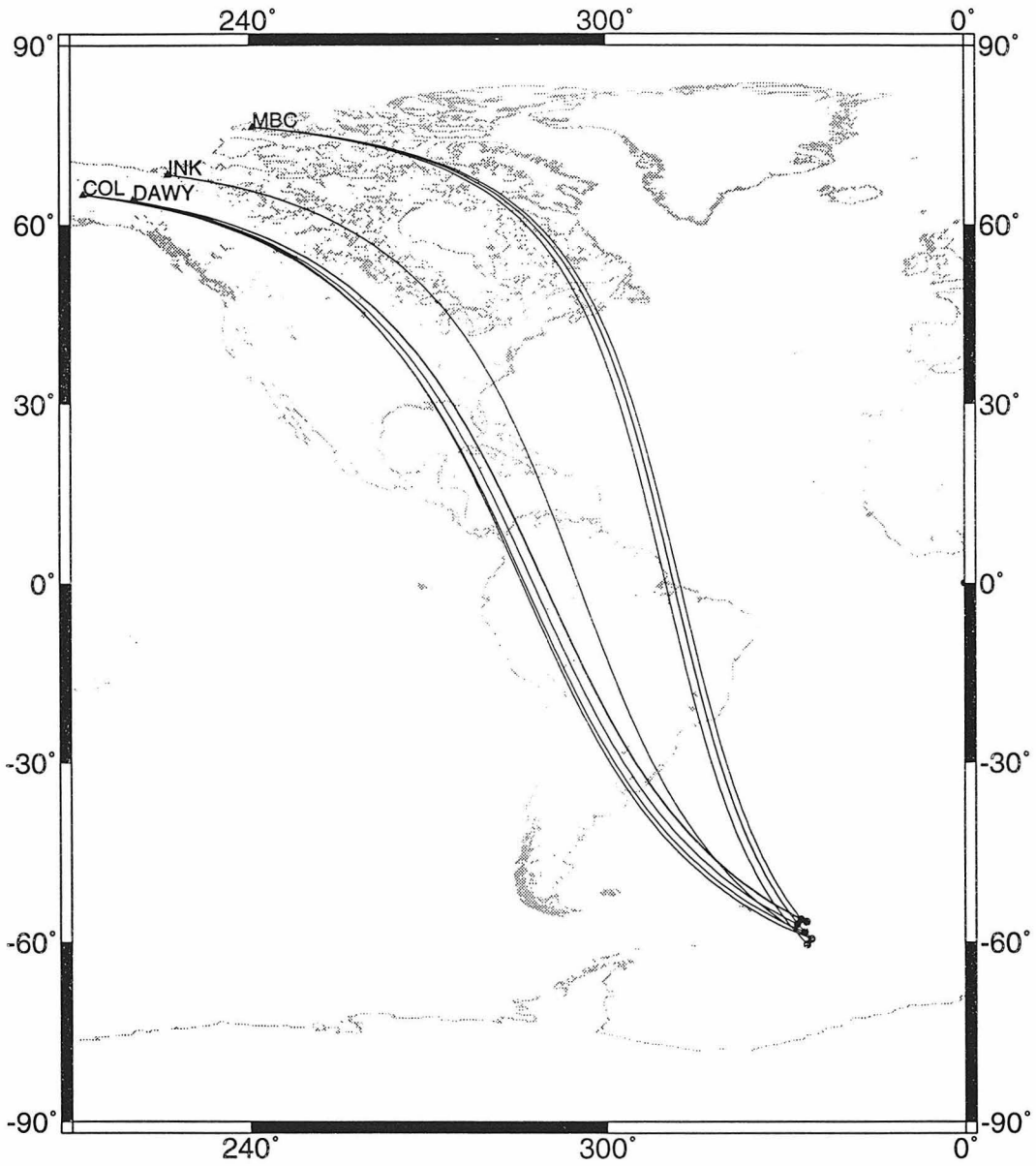

Figure 5.5: Polar ray paths from South Sandwich Island to northwestern North America.

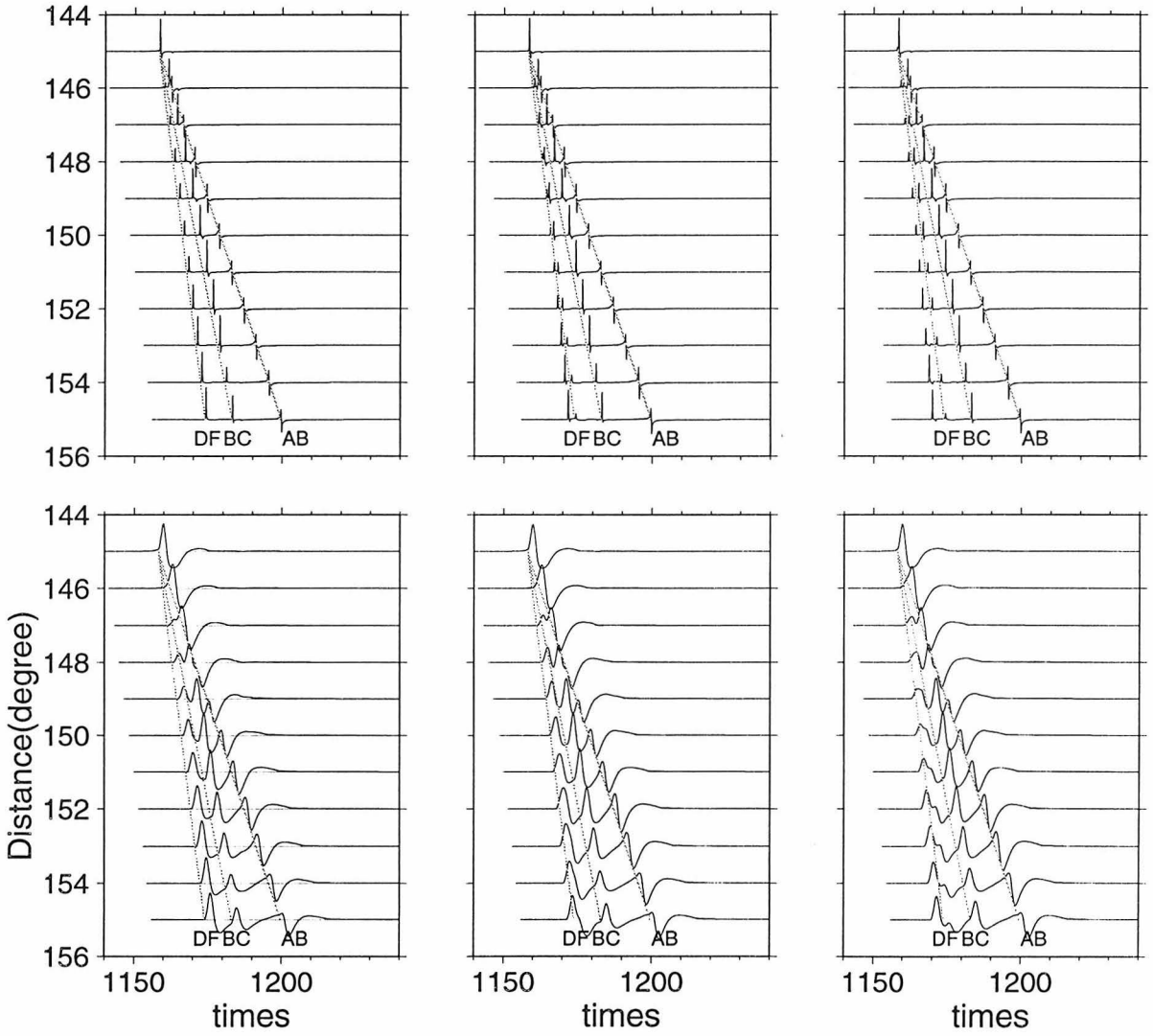

Figure 5.6: Upper panel contains synthetics for three models: PREM2, and the 3% and 5% cases. Lower panel contains corresponding long-period synthetics.

Table 5.1: List of South Sandwich events

No.	origin	latitude(°)	longitude(°)	depth(km)
1	661011	-60.4	-26.4	36
2	670523	-56.23	-27.47	122
3	670617	-58.36	-26.83	136.0
4	690118	-57.	-28.1	120
5	920824	-56.60	-26.56	109.0
6	921121	-56.66	-26.55	33.0
7	930309	-59.51	-25.71	33.0

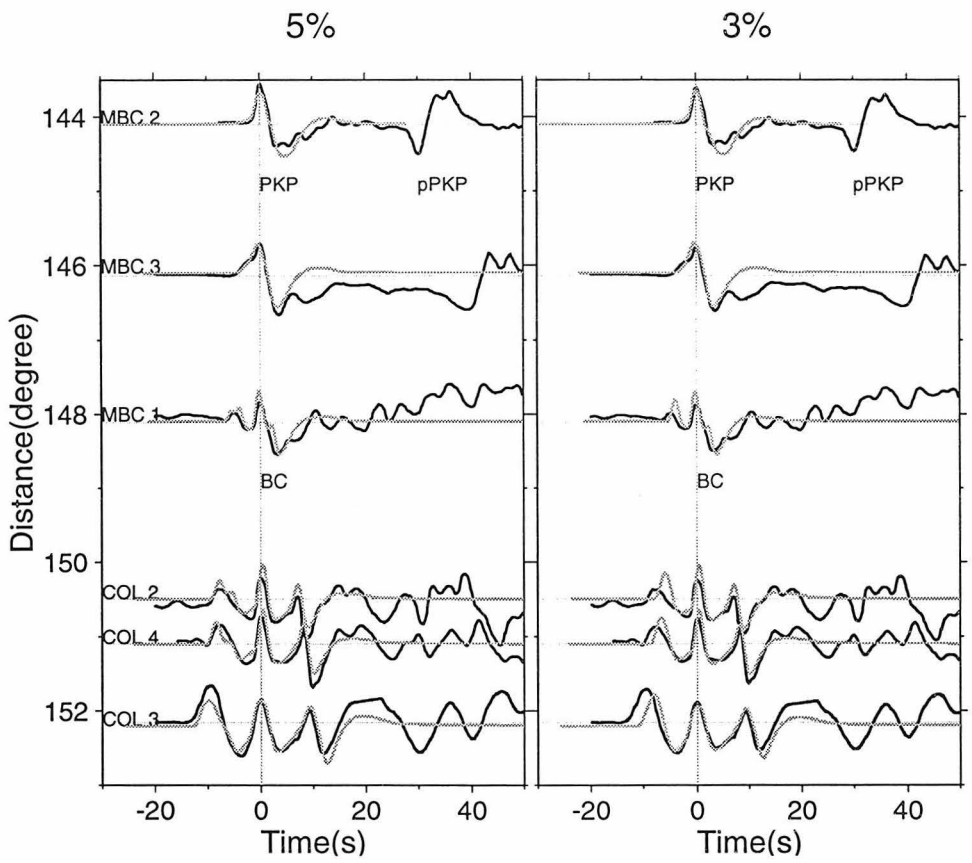

Figure 5.7: Record sections of long-period observations (heavy) compared with synthetics (light). Waveforms are aligned with BC.

5.4 Discussion

Song and Helmberger [1995a] presented strong evidence that the uppermost 150km of the inner core must be nearly isotropic. Both short-period and long-period waveform modeling of NS record sections at ranges 135° to 146° favor the isotropic PREM2 model over models with increased inner core velocities. This has been confirmed to some extent by *Creager* [1996] and is compatible with ISC data, *Shearer* [1994]. A smooth increasing model below that depth will not fit travel times without some type of jump as proposed by *Song and Helmberger* [1995a]. Synthetics for models with a jump as proposed here produce a broad first arrival (DF) at long-periods and a triplication at short-periods. The strong short-period branch is associated with the sharpness of this boundary and will have a travel time nearly the same as DFi over the ranges 148 to 154°. The bottom trace of the observed short-period record section of Figure 5.2 supports this feature. However, it is less clear on other traces where the behavior looks more scattered. Generally, DF is quite clear and strong at these ranges for EW paths, see *Song and Helmberger* [1995b].

The broadband data in Figure 5.8 probably presents the strongest case for the difference in waveshape between DF and BC, especially for events 5 and 6. Note that BC and DF would be expected to have the same shape if no triplication (structure) was present. This is the usual assumption used in data processing, see *Creager* [1992] and others. Part of the broadening of DF has been modeled by introducing attenuation in the inner core, *Doornbos* [1974]. Subsequent authors have typically applied a small t*-operator to correct for this effort, see *Cormier* [1981], and others. Perhaps this apparent attenuation has a path dependence as suggested by *Souriau and Romanowicz* [1996]. No differential attenuation has been applied to these synthetics although some would make the fit better.

In conclusion, we suggest a new picture of the inner core with an isotropic upper structure and an anisotropic lower structure. We suspect that the boundary zone has considerable lateral variation based on the large scatter in reported short-period travel times but this needs further study with long-period and broadband modeling.

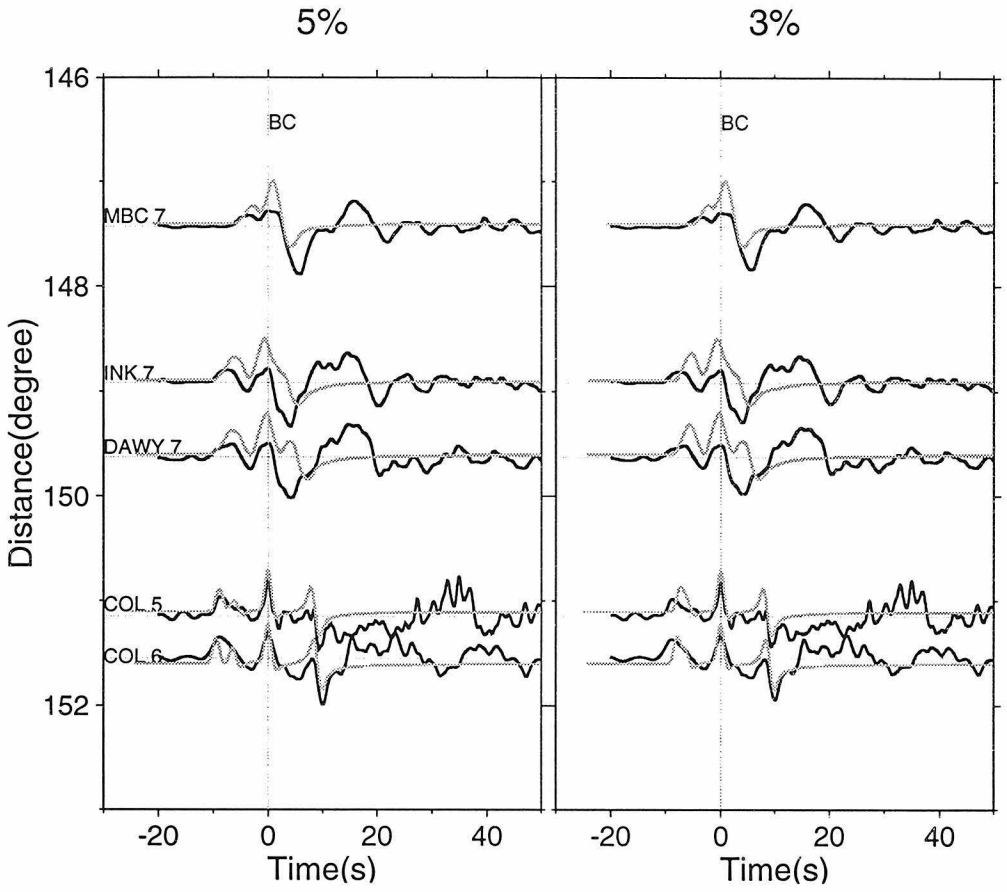

Figure 5.8: Comparison of broadband observations against synthetics where the waveforms are aligned with BC.

Bibliography

Anderson, D. L., Superplumes or supercontinents?, *Geology*, *22*, 39–42, 1994.

Anderson, O. L., and K. Masuda, A thermodynamic method for computing thermal expansivity, α, versus T along isobars for silicate perovskite, *Phys. Earth Planet. Inter.*, pp. 227–236, 1994.

Baumgardt, D. R., Evidence for a P-wave velocity anomaly in D″, *Geophys. Res. Lett.*, *16*, 657–660, 1989.

Bokelmann, G. H. R., and P. G. Silver, The Caribbean anomaly: short-wavelength lateral heterogeneity in the lower mantle, *Geophys. Res. Lett.*, *20*, 1131–1134, 1993.

Bullen, K. E., Compressibility-pressure hypothesis and the Earth's interior, *Mon. Not. R. Astron. Soc.*, *5*, 355–368, 1949.

Chapman, C. H., Exact and approximate generalized ray theory in vertically inhomogeneous media, *Geophys. J. R. astr. Soc.*, *46*, 201–233, 1976.

Chapman, C. H., and J. A. Orcutt, The computation of body wave synthetic seismograms in laterally homogeneous media, *Rev. Geophys.*, *23*, 105–163, 1985.

Chopelas, A., and R. Boehler, Thermal expansivity in the lower mantle, *Geophys. Res. Lett.*, *19*(19), 1983–1986, 1992.

Christensen, U., The influence of trench migration on slab penetration into the lower mantle, *Earth and planetary science letters*, *140*(1-4), 27–39, 1996.

Cormier, V. F., Short-period PKP phases and the anelastic mechanism of the inner core, *Phys. Earth Planet. Inter.*, *24*, 291–301, 1981.

Creager, K. C., Anisotropy of the inner core from differential travel-times of the phases PKP and PKiKP, *Nature*, *356*(6367), 309–314, 1992.

Creager, K. C., Inner-core rotation from differential PKP travel times at COL and the Alaska Seismic Network, *EOS trans. AGU*, *77*, 1996.

Davies, G., and M. Gurnis, Interaction of mantle dregs with convection - lateral heterogeneity at the core mantle boundary, *Geophys. Res. Lett.*, *13*(13), 1517–1520, 1986.

Davis, J. P., and M. Weber, Lower mantle velocity inhomogeneity observed at GRF array, *Geophys. Res. Lett.*, *17*, 187–190, 1990.

Ding, X., and D. V. Helmberger, Modeling D″ structure beneath Central America with broadband seismic data, *Phys. Earth Planet. Inter.*, *in press*, 1997.

Doornbos, D. J., The anelasticity of the inner core, *Geophys. J. R. astr. Soc.*, *38*, 397–415, 1974.

Doornbos, D. J., S. Spiliopoulos, and F. D. Stacy, Seismological properties of D″ and the structure of the thermal boundary layer, *Phys. Earth Planet. Inter.*, *41*, 225–239, 1986.

Dziewonski, A. M., and D. L. Anderson, Preliminary reference Earth model, *Phys. Earth Planet. Inter.*, *25*, 297–356, 1981.

Dziewonski, A. M., and D. L. Anderson, Travel times and station corrections for P waves at teleseismic distances, *J. Geophys. Res.*, *88*, 3295–3314, 1983.

Engebretson, D. C., K. P. Kelley, H. J. Cashman, and M. A. Richards, 180 million years of subduction, *GSA Today*, *2*, 93–100, 1992.

Gaherty, J. B., and T. Lay, Investigation of laterally heterogeneous shear velocity structure in D″ beneath Eurasia, *J. Geophys. Res.*, *97*(B1), 417–435, 1992.

Garnero, E., and T. Lay, Lateral variations in lowermost mantle shear-wave anisotropy beneath the north Pacific and Alaska, *J. Geophys. Res.*, *102*(B4), 8121–8135, 1997.

Garnero, E. J., and D. V. Helmberger, A very slow basal layer underlying the large-scale low-velocity anomalies in the lower mantle beneath the Pacific: Evidence from core phases, *Phys. Earth Planet. Inter.*, *88*, 117–130, 1995.

Garnero, E. J., and D. V. Helmberger, Seismic detection of a thin laterally varying boundary-layer at the base of the mantle beneath the Central-Pacific, *Geophys. Res. Lett.*, *23*, 977–980, 1996.

Garnero, E. J., and D. V. Helmberger, Further structural constraints and uncertainties of a thin laterally varying ultra-low velocity layer at the base of the mantle, *J. Geophys. Res.*, *submitted*, 1997.

Garnero, E. J., D. V. Helmberger, and S. P. Grand, Preliminary evidence for a lower mantle shear wave velocity discontinuity beneath the central Pacific, *Phys. Earth Planet. Inter.*, *79*, 335–347, 1993.

Grand, S. P., Mantle shear structure beneath the Americas and surrounding oceans, *J. Geophys. Res.*, *99*, 11591–11622, 1994.

Grand, S. P., and D. V. Helmberger, Upper mantle shear structure of North America, *Geophys. J. R. astr. Soc.*, *76*, 399–438, 1984.

Grand, S. P., R. D. van der Hilst, and S. Widiyantoro, Global seismic tomography: A snapshot of convection in the Earth, *GSA today*, *7*(4), 1–7, 1997.

Gurnis, M., The effects of chemical density differences on convective mixing in the Earth's mantle, *J. Geophys. Res.*, *91*(B11), 1407–1419, 1986.

Helmberger, D. V., Theory and application of synthetic seismograms, in *Earthquake: Observation, Theory and Interpretation*, edited by H. Kanamori and E. Boschi, Proc. Int. Sch. Phys. Enrico Fermi, 1983.

Helmberger, D. V., and R. A. Wiggins, Upper mantle structure of mid-western United States, *J. Geophys. Res.*, *76*, 3229–3245, 1971.

Helmberger, D. V., E. J. Garnero, and X. Ding, Modeling two-dimensional structure at the core-mantle boundary, *J. Geophys. Res.*, *101*(B6), 13963–13972, 1996.

Helmberger, D. V., L.-S. Zhao, and E. J. Garnero, Construction of synthetics for 2D structures; Core phases, in *Seismic modeling of the Earth Structure*, edited by E. Boschi, G. Ekstrom, and A. Morelli, pp. 183–222, North-Holland, New York, 1997.

Houard, S., and H. C. Nataf, Further evidence for the "Lay discontinuity" beneath Northern Siberia and the Northern Atlantic from short-period P-waves recorded in France, *Phys. Earth Planet. Inter.*, *72*, 264–275, 1992.

Houard, S., and H. C. Nataf, Laterally varying reflector at the top of D″ beneath northern Siberia, *Geophys. J. Int.*, *115*, 168–182, 1993.

Isaak, D. G., O. L. Anderson, and T. Goto, Measured elastic-moduli of single-crystal MgO up to 1800K, *Phys. Chem. Minerals*, *16*(7), 704–713, 1989.

Jordan, T. H., and W. S. Lynn, A velocity anomaly in the lower mantle, *J. Geophys. Res.*, *79*, 2679–2685, 1974.

Kanamori, H., E. Hauksson, and T. Heaton, TERRAscope and CUBE project at Caltech, *EOS trans. AGU*, *72*, 564, 1991.

Kendall, J.-M., and C. Nangini, Lateral variations in D″ below the Caribbean, *Geophys. Res. Lett.*, *19*, 399–402, 1996.

Kendall, J.-M., and P. M. Shearer, Lateral variation in D″ thickness from long-period shear-wave data, *J. Geophys. Res.*, *99*, 11575–11590, 1994.

Kennett, B. L. N., and E. R. Engdahl, Travel-times for global earthquake location and phase identification, *Geophys. J. Int.*, *105*, 429–465, 1991.

Langston, C. A., The SSPmP phase in regional wave-propagation, *Bull. Seism. Soc. Am.*, *86*, 133–143, 1996.

Lay, T., Localized velocity anomalies in the lower mantle, *Geophys. J. R. astr. Soc.*, *72*(2), 483–516, 1983.

Lay, T., Seismology of the lower mantle and core-mantle boundary, *Rev. Geophys.*, *33*, 325–328, 1995.

Lay, T., and D. V. Helmberger, Body wave amplitude patterns and upper mantle attenuation variations across North America, *Geophys. J. R. astr. Soc.*, *66*, 691–726, 1981.

Lay, T., and D. V. Helmberger, A lower mantle S-wave triplication and the shear velocity structure of D″, *Geophys. J. R. astr. Soc.*, *75*(3), 799–837, 1983a.

Lay, T., and D. V. Helmberger, The shear-wave velocity-gradient at the base of the mantle, *J. Geophys. Res.*, *88*(B10), 8160–8170, 1983b.

Lehman, I., P′, *Publ. Bur. cent. Seism. Int. Ser. A*, *14*, 3, 1936.

Li, X. D., and B. Romanowicz, Global mantle shear velocity model developed using nonlinear asymptotic coupling theory, *J. Geophys. Res.*, *101*, 22245–22272, 1996.

Liu, H., P. M. Davis, and S. Gao, SKS splitting beneath Southern California, *Geophys. Res. Lett.*, *22*, 767–770, 1995.

Loper, D. E., and T. Lay, The core-mantle boundary region, *J. Geophys. Res.*, *100*(B4), 6397–6420, 1995.

Masters, G., Core models ring true, *Nature*, *366*, 629–630, 1993.

Masters, G., S. Johnson, G. Laske, and H. Bolton, A shear-velocity model of the mantle, *Roy. Soc. of London Philosophical Trans.*, *354*(1711), 1385–1410, 1996.

Masters, T. G., and P. M. Shearer, Large-scale 3-dimensional structure of the mantle(abstract), *EOS trans. AGU*, *73*, 201, 1992.

McSweeney, T. J., K. C. Creager, and R. T. Merrill, Depth extent of Inner-core seismic anisotropy and omplications for geomagnetism, *Phys. Earth Planet. Inter., in press*, 1997.

Mitchell, B. J., and D. V. Helmberger, Shear velocities at the base of the mantle from observations of S and ScS, *J. Geophys. Res.*, *78*, 6009–6020, 1973.

Mori, J., and D. V. Helmberger, Localized boundary layer below the Mid-Pacific velocity anomaly identified from a PcP precursor, *J. Geophys. Res.*, *100*, 20359–20365, 1995.

Nataf, H.-C., and S. Houard, Seismic discontinuity at the top of the D″: a world-wide feature?, *Geophys. Res. Lett.*, *20*, 2371–2374, 1993.

Richards, M. A., and D. C. Engebretson, Large-scale mantle convection and the history of subduction, *Nature*, *355*, 437–440, 1992.

Shearer, P. M., Constraints on Inner-core anisotropy from PKP(DF) travel-times, *J. Geophys. Res.*, *99*(B10), 19647–19659, 1994.

Silver, P. G., and W. W. Chan, Shear wave splitting and sub-continental mantle deformation, *J. Geophys. Res.*, *96*, 16429–16454, 1991.

Song, X. D., Anisotropy of the Earth's inner core, *Rev. Geophys., in press*, 1997.

Song, X. D., and D. V. Helmberger, A P-wave velocity model of Earth's core, *J. Geophys. Res.*, *100*(B6), 9817–9830, 1995a.

Song, X. D., and D. V. Helmberger, Depth dependence of anisotropy of Earth's Inner-core, *J. Geophys. Res.*, *100*(B6), 9805–9816, 1995b.

Song, X. D., and D. V. Helmberger, PKP differential travel times: Implications for three-dimensional lower mantle structure, *Geophys. Res. Lett., Submitted*, 1997.

Song, X. D., and P. G. Richards, Seismological evidence for differential rotation of the earths inner-core, *Nature*, *382*(6588), 221–224, 1996.

Souriau, A., and B. Romanowicz, Anisotropy in Inner-core attenuation - a new-type of data to constrain the nature of the solid core, *Geophys. Res. Lett.*, *23*(1), 1–4, 1996.

Su, W. J., and A. M. Dziewonski, Inner-core anisotropy in 3 dimensions, *J. Geophys. Res.*, *100*(B6), 9831–9852, 1995.

Su, W. J., R. L. Woodward, and A. M. Dziewonski, Degree-12 model of shear velocity heterogeneity in the mantle, *J. Geophys. Res.*, *99*(B4), 6945–6980, 1994.

Su, W. J., A. M. Dziewonski, and R. Jeanloz, Planet within a planet - rotation of the Inner-core of Earth, *Science*, *274*(5294), 1883–1887, 1996.

Tanaka, S., and H. Hamaguchi, Heterogeneity in the lower mantle beneath Africa, as revealed from S and ScS phases, *Tectonophysics*, *209*(1-4), 213–222, 1992.

Tanaka, S., and H. Hamaguchi, Degree one heterogeneity and hemispherical variation of anisotropy in the Inner-core from PKP(BC)-PKP(DF) times, *J. Geophys. Res.*, *102*(B2), 2925–2938, 1997.

van der Hilst, R. D., S. Widiyantoro, and E. R. Engdahl, Evidence for deep mantle circulation from global tomography, *Nature*, *386*, 578–584, 1997.

Vidale, J. E., and H. M. Benz, Seismological mapping of fine structure near the base of the Earth's mantle, *Nature*, *361*, 529–532, 1993.

Vidale, J. E., and D. Garcia-Gonzalez, Seismic observation of a high-velocity slab 1200–1600 km in depth, *Geophys. Res. Lett.*, *15*, 369–372, 1988.

Vinnik, L. V., G. L. Kosarev, and L. I. Makeyeva, Anisotropy of the lithosphere from observations of SKS and SKKS, *Proc. (Doklady) of the Academy of Sciences of the USSR*, *278*, 1335–1339, 1984.

Weber, M., P- and S-wave reflections from anomalies in the lowermost mantle, *Geophys. J. Int.*, *115*, 183–210, 1993.

Weber, M., Lamellae in D″— an alternative model for lower mantle anomalies, *Geophys. Res. Lett.*, *21*, 2532–2534, 1994.

Wen, L., and D. L. Anderson, The fate of slabs inferred from seismic tomography and 130 million years of subduction, *Earth Planet. Sci. Lett.*, *133*, 185–198, 1995.

Wen, L., and D. V. Helmberger, A 2D hybrid method and applications to core phases, *J. Geophys. Res.*, *in preparation*, 1997.

Williams, Q., and E. Garnero, Seismic evidence for partial melt at the base of earths mantle, *Science*, *273*(5281), 1528–1530, 1996.

Wright, C., K. J. Muirhead, and A. E. Dixon, The P wave velocity structure near the base of the mantle, *J. Geophys. Res.*, *90*, 623–634, 1985.

Wysession, M. E., E. A. Okal, and C. R. Bina, The structure of the core-mantle boundary from diffracted waves, *J. Geophys. Res.*, *97*, 8749–9764, 1992.

Young, C. J., and T. Lay, Evidence for a shear velocity discontinuity in the lower mantle beneath India and the Indian Ocean, *Phys. Earth Planet. Inter.*, *49*, 37–53, 1987.

Young, C. J., and T. Lay, The core shadow zone boundary and lateral variations of the P velocity structure of the lowermost mantle, *Phys. Earth Planet. Inter.*, *54*(1-2), 64–81, 1989.

Young, C. J., and T. Lay, Multiple phase-analysis of the shear velocity structure in the D″ region beneath Alaska, *J. Geophys. Res.*, *95*(B11), 17385–17402, 1990.

Zhang, J. J., and T. Lay, Investigation of a lower mantle shear-wave triplication using a broad-band array, *Geophys. Res. Lett.*, *11*(6), 620–623, 1984.

Zhao, Y. S., and D. L. Anderson, Mineral physics constraints on the chemical-composition of the Earth's lower mantle, *Phys. Earth Planet. Inter.*, *85*(3-4), 273–292, 1994.

Zhong, S., and M. Gurnis, Dynamic interaction between tectonic plates, subducting slabs, and the mantle, *Earth Interactions*, 1997.

Appendix A Construction of Synthetics from 3D Tomographic Model

A.1 Introduction

Tomographic model gets more and more higher resolution because computing power allow seismologist to put more data into inversion. Two independent researches in P (*van der Hilst et al.* [1997]) and S(*Grand* [1994]) tomographic studies involves different data set and different inversion techniques produce remarkable similarities between them for regions where the data coverage is good. On the other hand, the D″ studies show that the lateral heterogeneity in this region may be in even smaller scale than the current tomographic model can resolve. And the small scale structures may show great impact on the convection pattern. The high resolution studies with dense seismic arrays, therefore, as a complementary tool is necessary. We develop some techniques based on 1D WKM and generalized ray theory(GRT) by considering the lateral structures in the current tomographic models. Our method will retrieve a 2D cross-section for a given source-receiver geometry from the 3D tomographic model and account for the affect of the lateral variation in the cross-section.

A.2 Review of WKM and Cagniard-de Hoop method

The ray theory has some advantages over the numerical method e.g., finite element and finite difference: 1. Less computing power is required; 2. It is easy to understand where the contributions are from for the phase, therefore help to identify the phases and the sampling depth of the phase. It's especially useful in studying the triplications caused by the discontinuities in the interior of the Earth. 3. Numerical method is prohibitly expensive for teleseismic modeling. WKM is a variant from the commonly

used WKBJ synthetics [*Chapman*, 1976; *Chapman and Orcutt*, 1985]. Usual WKBJ method constructs synthetics using rays under-shoot and over-shoot the receiver, while WKM uses rays arrival at the receiver. The former method may easily violate casualty. It is reported that WKM is able to produce more reliable arrivals in the shadow zone where WKBJ method will produce truncation phase, *Helmberger et al.* [1997]. WKM method parameterize the velocity model in the same way as GRT, i.e., layered model. The rays reflecting from top of each layer will form a p-t curve, where p is ray parameter and t is the travel time associated with that ray. From the p-t curve, the synthetics is constructed with:

$$\Phi(x,t) = \sqrt{\frac{2}{x}}\frac{1}{\pi}\frac{\Delta}{\sin(\Delta)} Im\left[\frac{1}{\sqrt{t}} * \sum_t \frac{\sqrt{p}C(p)}{\eta_1}\left|\frac{dp}{dt}\right|\right] \tag{A.1}$$

where $C(p)$ is transmission and reflection coefficients for the ray, and dp/dt can be obtained from the p-t curve. Each turning point in the p-t curve will produce an arrival on the final synthetics.

Generalized ray synthetic is another commonly technique to generate body wave synthetics. Starting from *Helmberger* [1983], the potential is expressed as:

$$\Phi(x,t) = \sqrt{\frac{2}{x}}\frac{1}{\pi}\frac{\Delta}{\sin(\Delta)}\left[\frac{1}{\sqrt{t}} * \sum \Psi_j(p)\right] \tag{A.2}$$

where j is the index for rays, and

$$\Psi_j(p) = Im\left(\frac{\sqrt{p}}{\eta_1}\prod(p)\frac{dp}{dt}\right) \tag{A.3}$$

The function dp/dt is derived from:

$$t = px + \sum_{j=1}^{j=n} \eta_j T h_j \tag{A.4}$$

It has been shown that when only the first motion is considered, WKM and GRT are equivalent.

A.3 2D synthetics

A tomographic model is a mild perturbation to a reference 1D model. We compute the raypaths using the reference model and map them into tomographic 2D cross section, and then compute the travel time residual with respect to the 1D reference model due to the lateral variations. The residual time may be used in GRT to shift the responses in equation A.3 for each ray and the final response is the first-order approximation of the response for the lateral structure. Or the residual time may be applied to the p-t curve in WKM method to produce 2D synthetics. These adjustments are similar to the conventional tomographic method, i.e., only perturbing the travel time along the fixed ray path, we call it time-correction method. For better approximation, we compute the velocities for each ray segment based on the 2D cross section, and use those velocities to find the ray that satisfies the Snell's law, and thus construct a p-t curve to produce synthetics. We call the above process path correction. The transmission and reflection coefficients associated with the core-mantle boundary are also re-computed according to the velocity from 2D model. WKM cannot treat the reflection phases, e.g., ScS_H, effectively. Because the p-t curve stops right at the core-mantle boundary, and only a cut-off phase at the arrival time of ScS will be produced, but with a wrong amplitude, we use GRT to compute the ScS phase with time correction only, and sum up with the responses WKM can deal with fine.

The importance of the path correction is shown by synthesizing for a simplified cross-section model with a D″ layer of 200 km thick and a S velocity jump of 4% at source side and disappears at the receiver side as displayed in Figure A.1. Figure A.2 displays the raypaths computed for reference model and the raypaths corrected with 2D variations. Note that the raypaths in 1D model are symmetric, but they are distorted when encountering the fast anomaly marked with gray shade in right panel. The asymmetry in the raypaths for the 2D case is due to that the velocity structures for both legs are different, namely, the velocity in the left side is 4% faster than that in the right side which is the same as the reference model. We do not account for the vertical boundary because most of the rays across this boundary at a large incident

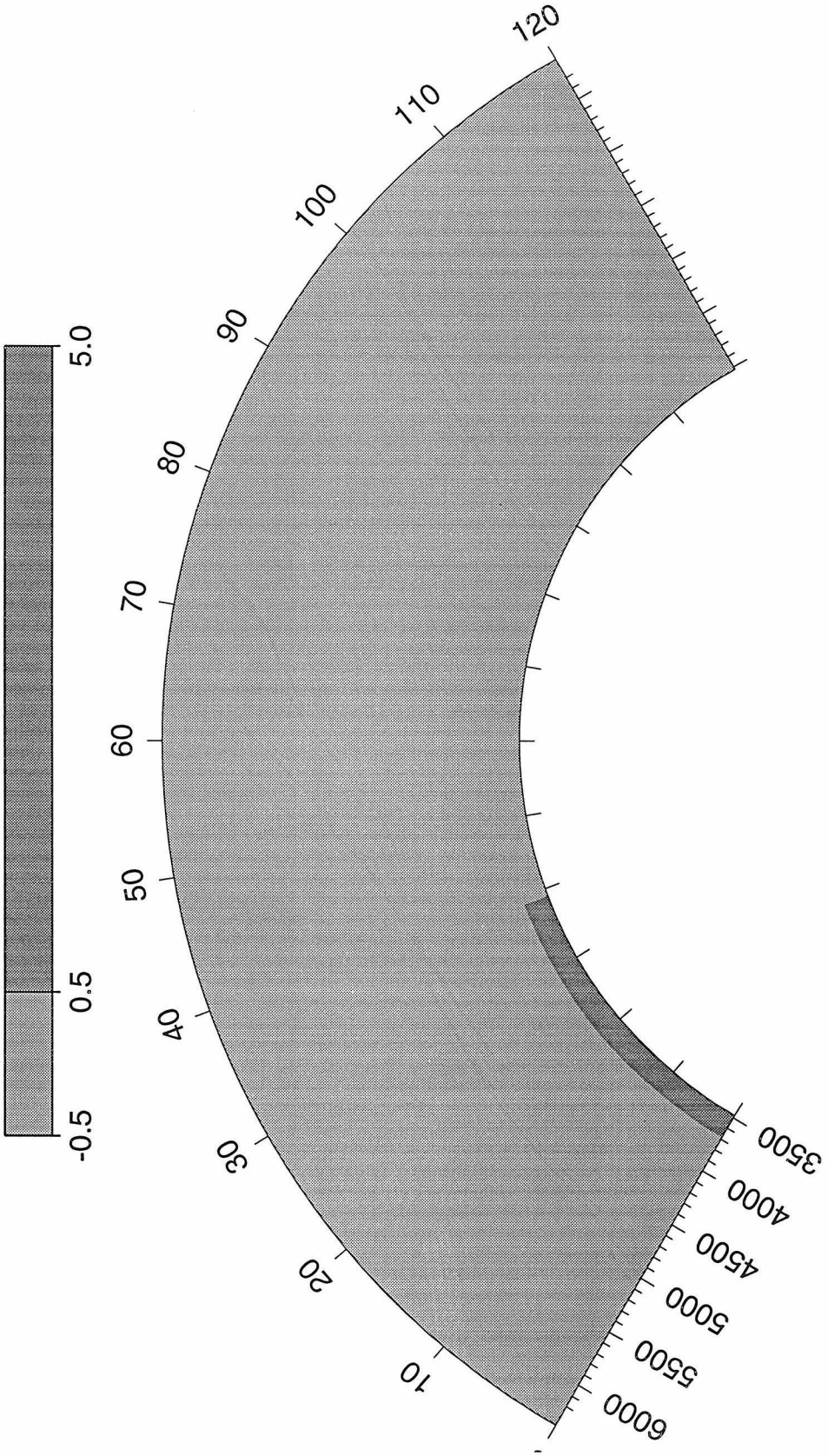

Figure A.1: A simplified 2D model with a 4% S velocity jump in the shaded area. The source is at the start point.

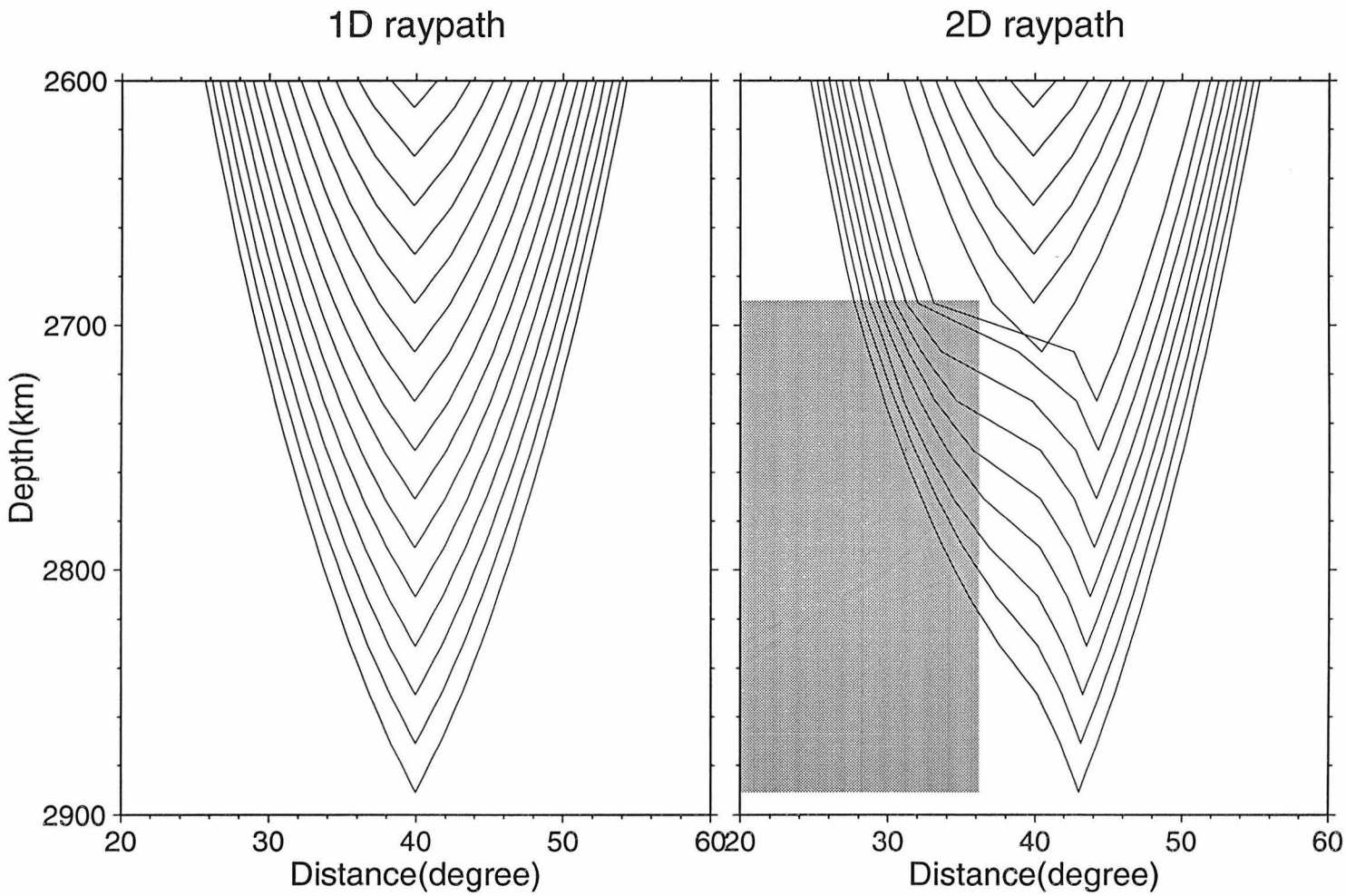

Figure A.2: Raypaths for 1D (left panel) and 2D model (right panel). The gray shaded area in right panel is the area where S velocity is 4% faster. Note above the shades area, the raypaths are the same in both panels.

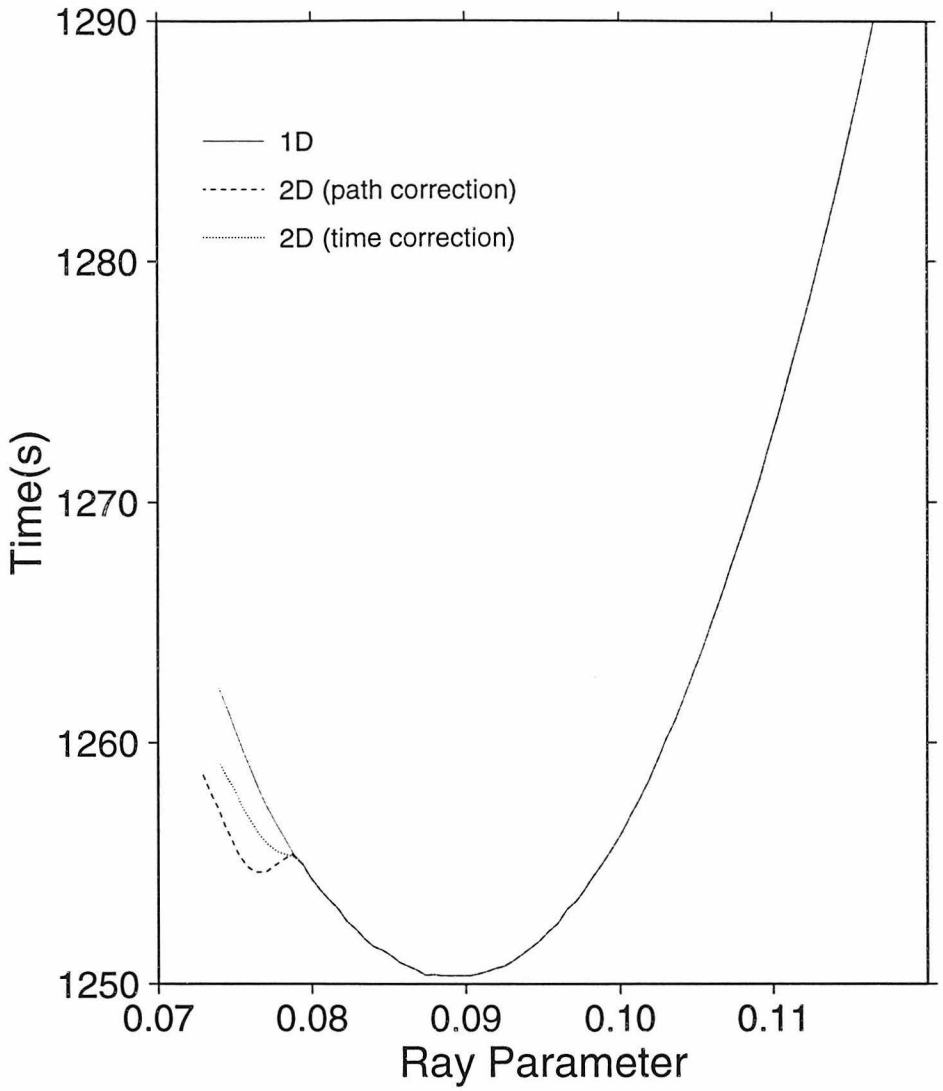

Figure A.3: P-t curves for 1D model (Solid line), 2D model with only the time corrections (dotted line) and 2D model with the path corrections (dashes lines). They are all the same when $p < 0.08$, where the ray go above the D″ layer.

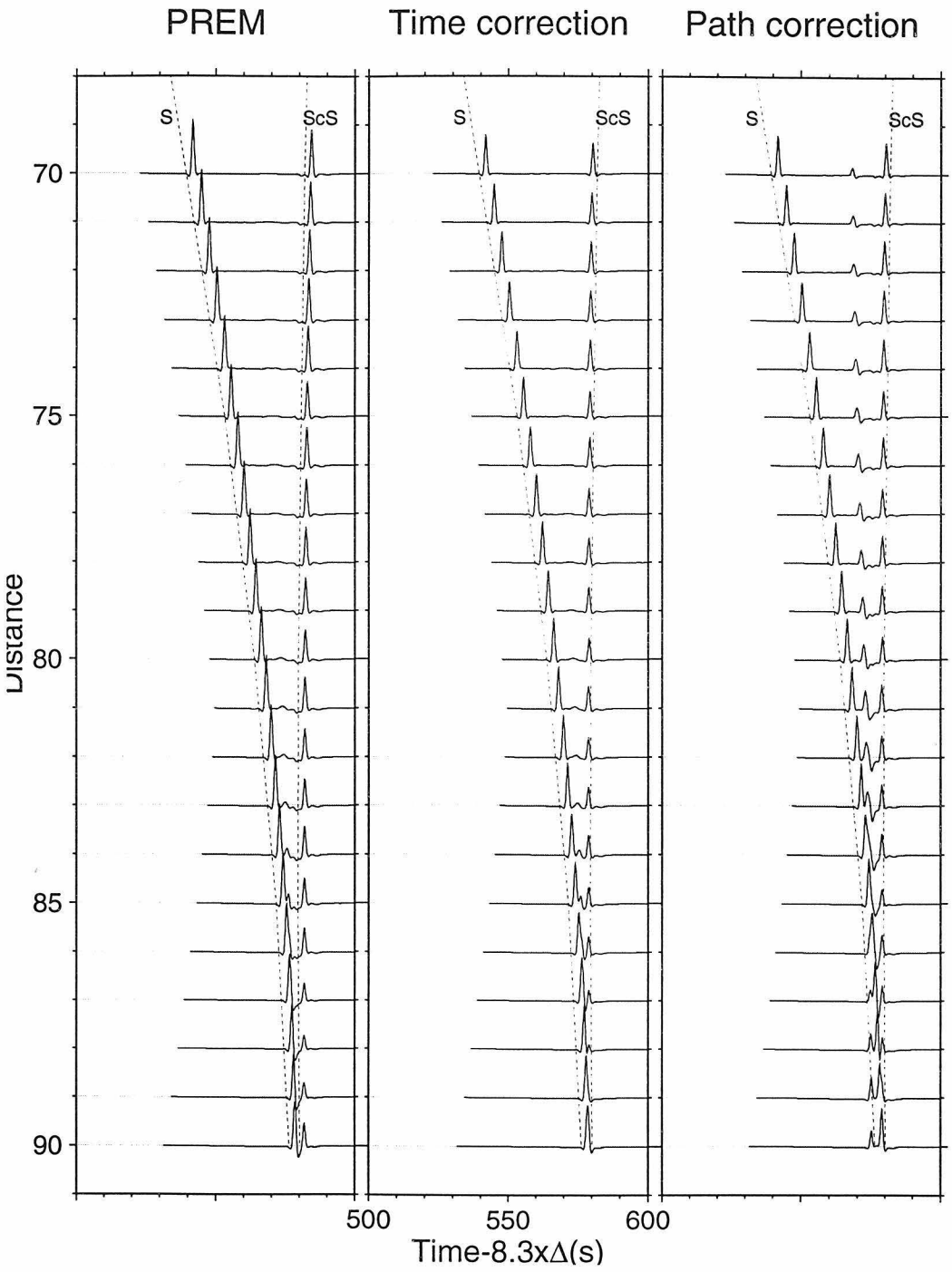

Figure A.4: Synthetics generated for 1D reference model, the 2D model with only the time corrections and thd 2D model with the path coorections. The dashed lines stand for the S and ScS travel times predicted by PREM.

angle for our S synthetics. Figure A.3 displays three different p-t curves at distance of 82° for a 1D model, a 2D model with the path corrections and a 2D model with time corrections only respectively. The only difference between these curves is at the left-lower corner, where the p-t curve for 2D model with path correction shows an additional wiggle which will produce an additional arrival in the synthetics. While the fast structure doesn't affect the p-t curve with only 2D time corrections as much, therefore the arrival of Scd phase should be much smaller as will be displayed in Figure A.4. Figure A.4 displays the Green's functions for the reference model, for 2D model with only time corrections and with path corrections. The included lines are the S and ScS times predicted by PREM. ScS is faster than PREM in the right two panels because it propagates through part of the fast D″ layer. The Scd phase in the middle of S and Scd is produced in the right panel, while in the middle panel, Scd phase is not seen until beyond 83°. This suggests that the path correction is a better approximation than time correction when dealing with a laterally varying structure.